technische universität
dortmund

DISSERTATION ZUR ERLANGUNG DES AKADEMISCHEN GRADES
DR. RER. NAT.

ON THE OPTICAL DETECTION OF THE PHYSICAL STATE OF EXCITABLE MEMBRANES

Sara Carina Fedosejevs

Medizinische und Biologische Physik
Fakultät Physik
Technische Universität Dortmund
August 2022

Erstgutachter: Prof. Dr. Matthias Schneider
Zweitgutachter: Dr. Matan Mussel

Datum der Disputation: 11.November 2022

Ein eigentümlicher Zauber umgibt das Erkennen von Maß und Harmonie.

- Carl Friedrich Gauß

SUMMARY

Phase transitions, phenomena deeply rooted in thermodynamics, are subject to discussion in biological systems. They are the source of nonlinearities and have been suggested to be responsible for cellular functions including nerve pulse propagation. In pure lipid interfaces characteristic properties as excitability or permeability are introduced during a transition. These relations would have a tremendous effect on the lipid-based cellular membranes. However, evidence for these transitions in cellular membranes of excitable cells - participating in nerve pulse conduction - has so far not been provided. In this thesis, the existence of phase transitions in cellular membranes is explored on single neuronal cells. Based on the findings it is elaborated on to what extent the transitions in cells could be relevant for (membrane) functionality.

To approach this question different optical methods/tools are established and applied to characterize thermodynamical phase states of lipid-based membranes. The combination of a confocal microscope with sensitive fluorescence detection offers manifold possibilities to use fluorescent dyes embedded into biological membranes as local state reporters. The optical as well as temporal resolution is strongly enhanced compared to conventional microscopy and allows observations up to a molecular level.

In the first part, the focus lies on the characterization of artificial lipid systems and the evaluation of different optical (state) parameters. For one, an optical state parameter, the ratio parameter, is introduced. This parameter reflects the position of the fluorescence emission spectrum which is subject to phase state changes for the used dye *Atto488 DPPE*. A transition between phase states is reflected by a nonlinear shift in that parameter. By that, optical state diagrams of pure lipid interfaces (vesicle suspensions, monolayers..) are recorded for different phospholipid types under temperature variation and pH modulation. Further, examples are provided that the intensity-independent fluorescence lifetime of the dye is a potential state parameter as well.

Measurements on lipid monolayers provide evidence for the direct coupling of the emission fluorescence of the dye to the thermodynamics of its surrounding regime. Optical parameters, such as ratio parameter and lifetime, are directly correlated to the mechanical state parameter (area per molecule). Additionally, localized emission intensity fluctuations can be traced back to a thermodynamical origin as they are strongly coupled to the phase state and feature the phenomenology predicted for thermodynamic fluctuations: A maximum in the amplitude and timescale aligned with the susceptibilities during the phase transition.

On the other hand, lipid systems are approached by fluorescence correlation spectroscopy. Upon autocorrelation of intensity traces characteristic timescales are extracted from the optical response of single, fluorescent molecules. This technique is utilized to measure diffusion coefficients state-dependently and protonation rates at lipid interfaces. A state-dependent diffusion behavior - mirrored in the diffusion coefficient of the embedded dye - is detected in giant unilamellar vesicles with a shift over orders of magnitude as well as in lipid monolayers. Upon these measurements the groundwork is layed to use this setting for a holistic thermodynamical characterization of various systems.

In the second part this methodology is subsequently applied to living cells. At first, ratiometric measurements are conducted: A local spot in the cellular membrane ($\sim 1\ \mu\text{m}^2$) of a single, neuronal cell is monitored during temperature variation and a nonlinearity in the ratio parameter detected. It features similar characteristics as the optical response of *Atto488 DPPE* recorded during a phase transition in pure lipid systems and is identified as the latter. The transition is localized directly in the membrane of the single cell which is verified by the inclusion of additional characterizing parameters such as fluorescent lifetime and diffusion times. The detected transitions are extraordinary sharp (~ 1 °C) and are located at ~ 18.5 °C. This sharpness represents a nonlinearity within the membrane such that preconditions for nonlinear excitability and associated threshold behavior are created, similar to attributes describing the phenomenology of action potentials.

The nonlinearities in the optical response - identified as transitions - are strongly sensitive to pH variations. The melting temperature is increased upon acidification of the extracellular buffer solution (pH 5.5) to $\overline{\text{T}}_m = 29.9$ °C. This underlines the significance of these findings for physiological processes as a shift of pH - which is easily induced within cells during biochemical reactions is - is potent enough to modulate the membranes' state drastically. Further, it is indicated that the physical state of the membrane is subject to adaption within networks of cells. For adjacent cells and also within a connected layer of cells the transition points are significantly closer to each other than what would be expected from the overall distribution of individual transition points taken from single, not connected cells. This assimilation of physical state and hence material properties between adjacent cells will have significant impact on properties of the cellular network. It would, for instance, enhance the effective conduction of signals between them.

In conclusion, in this thesis important groundwork is layed to detect physical states within lipid-based membranes by a collection of optical tools. It yields strong support that the used fluorescent dye undergoes a thermodynamical coupling with the interface and gets part of its thermodynamic entity. The identification of a phase transition within the cellular membrane of a single neuronal cell strengthens the hypothesis that cellular functionality is coupled to nonlinear material behavior introduced by phase transitions.

CONTENTS

1. INTRODUCTION

Erwin Schrödinger's question *What is life?* which he formulated and pursued in the 1940s is exemplary for the interest of physicists in biology. Upon approaching cells from a physical point of view he derived the theoretical prediction of an *aperiodic crystal* containing the genetic information [1], inspiring the discovery of the double helix structure of the DNA molecule by Crick and Watson in the 1950s [2]. This is a prominent example in which biology has benefited from the involvement of physicists.

Historically, *physics* and *biology* are rather separated fields. The term *physics* as the *science of nature* was coined by Aristoteles around 350 B.C. and originates in Greek culture. Initially, it evolved as a field of philosophy. Observations in nature, such as the appearance of the night sky, weather phenomena, geometry etc. were systematically conducted and it was tried to understand their causes. Later, these observations were put into mathematical equations and physical *laws*, or rather *natural laws* were derived. It became clear that processes were following certain laws and did not happen randomly. For instance, planet movements may appear chaotic at first sight, but they follow indeed natural laws. By applying them it is even possible to predict the movements.

Living systems have not been approached in this spirit for a long time. Observations within these systems were simply not possible as processes happen on a cellular or even molecular level and are not visible by eye. The existence of a *cellular* level was not clear until the 17th century when Robert Hooke discovered the cell as the smallest unit in living systems. A technological progress in optics, the invention of the light microscope in the beginning of the 17th century was crucial for that discovery and even opened up access to the molecular level in the long run. *Biology* emerged as the *science of life* which is rather dedicated to the phenomenology and description of living beings.

Even nowadays where we have the tools to overcome these limitations these two sciences still kind of coexist. Even though attributes can be declared for defining that a system is alive, there is no *theory of life*. However, it is obvious that the complexity of a living organism must somehow follow certain laws in order to function and thus a demarcation between these two sciences is only useful to a limited extent. Natural laws must apply, for instance, to water regardless of where it is located, in an ocean or (rather bound) in a living cell.

This thesis is dedicated to contribute building a bridge between physics and biology, by observing physical phenomena within biological systems and investigating their role.
Classically, the mechanisms of intra- and intercellular communications are approached on a molecular level. Signal transduction pathways are explained by an interplay of receptors, hormones and cascades of protein activation as well as channel proteins to evoke a cellular response.
Nerve pulse conduction, for instance, is described via an action potential propagating along cells to conduct the signal between the location of the stimulus and the receiver (brain). Phenomenologically, an action potential is a nonlinear pulse which is excited when a certain threshold is exceeded. Historically, it is perceived as an electrical phenomenon since a modulation of the membrane potential is present during an action potential. On the molecular level it is interpreted as the opening of voltage-dependent channel proteins located in the membrane [3]. The induction of ion flow through the membrane upon depolarization in turn affects the transmembrane potential.
However, upon signal transduction along membranes a macroscopic output is generated by a *cooperative* interplay on the molecular level and a thermodynamic point of view is useful as it yields a rather macroscopic approach.
The cellular membrane which plays a central role for nerve pulse conduction is a lipid-based bilayer. Interestingly, pure lipid membranes are known to exhibit similar features as those observed during nerve pulse propagation, such as permeability and the excitability of nonlinear pulses [4, 5].

The functionality of these model systems is induced by the existence of physical phase states which are distinguished by their structural order. The lipid interface itself and its hydration shell is a thermodynamic entity and the cooperative transition between these states causes nonlinearities in associated macroscopic material properties.
Concerning the action potential, this idea was put forward within a holistic thermodynamical approach by Kaufmann and Heimburg [6, 7, 8]. It suggests a local propagating phase transition in the membrane as the underlying mechanism of nerve pulse propagation. As such, it is perceived as an adiabatic phenomenon featuring attributes of an acoustic pulse. All parameters are modulated during its propagation and can locally induce functions in the membrane. The threshold is understood as the barrier to induce a phase transition in the layer. In this picture, the excitation strength needed to overcome the threshold and trigger an action potential depends on the phase state of the membrane. Hence, the membrane state is key and controls this function of excitability. Not only within nerve pulse conduction but also in other phenomena the role of the membrane phase state has been postulated to be essential. For instance, it has been associated as a *switch* for certain transport functions in the cell [9, 10].

For this theory to apply, among others, the existence of a phase transition would be a necessary feature of the cellular membrane. For pure lipid membranes it is a given property, but a cellular membrane is a composition of various lipid types, proteins and carbohydrates and the existence of a *cooperative* phase transition in the membrane is controversial. Nevertheless, several studies identify phase transitions in cellular ensembles [11, 12, 13, 14, 15]. The transitions appear rather broad ($\sim 15\,°C$) which has been often used to neglect their biological relevance. In order to be consistent with a threshold-like excitation a much sharper transition is expected. However, excitable neuronal cells have not been reported to be subject to phase state characterizing measurements so far and a proof of phase transitions on a single cellular level is missing even more.

The existence and biological relevance of physical phase states in lipid-based cellular membranes shall be further investigated in this thesis. The missing link between theory and reality - as to what extent the phase state of the membrane plays a role for functionality including nerve pulse propagation - shall be provided.

In order to invest this, an optical approach using confocal microscopy is applied. Fluorescent dyes are embedded into lipid-based membranes and instrumentalized as local state reporters. Many dyes exhibit a sensitivity to their environment as they undergo a thermodynamical coupling which is mirrored in their emission properties. This is utilized to identify phase states of artificial, lipid systems as well as living, neuronal cells, and to record (optical) state diagrams. Additionally, within the setting of a fluorescence correlation spectrometer (FCS) characteristic timescales of membrane associated processes are extracted and state-dependently investigated.

2. THEORETICAL CONSIDERATIONS ON THE ROLE OF THERMODYNAMICS IN BIOLOGY

2.1. INTRODUCTION TO BIOLOGICAL MEMBRANES

Biology - the science of life - revolves around biological and living systems. In the following, a short introduction of what is referred to as a living or biological system is given.
Biological systems are built up from biomolecules which can be classified into lipids, proteins, carbohydrates and nucleic acids. Although there is no commonly accepted definition for *life* itself, there are basic characteristics that are undoubtedly linked to acknowledging a *life form*. Among them are the existence of a metabolism, the ability of reproduction and a life cycle. The capability to respond to external stimuli is yet another feature and requires the conduction of signals within the organism.

A similarity conserved within every living system is their composition of small functioning, self-organized units, commonly known as cells. They were first identified in plants in the 17th century by R. Hooke. In the extreme, organisms comply all characteristics of a *life form* within one cell. Examples for these unicellular organisms are bacteria or paramecia.
Cells, eukaryotic as well as prokaryotic, are enclosed by membranes ensuring the separation from the environment and the formation of a cell unit. Membranes are of particular interest as they are inevitably involved in all of the aforementioned processes featuring living systems. Therefore, they must hold manifold tasks within an organism.

CELLULAR MEMBRANES

Membranes are not only responsible for shielding the cell against its outer milieu and thereby maintain chemical gradients. They additionally ensure a compartmentalization within the cell as organelles are spatially bounded.

Essential elements of cellular membranes are lipids, proteins, carbohydrates, water and ions, where the amounts of lipids and proteins are dominating. These both molecule species each contribute in average $\sim 50\,\%$ to the mass of the cellular membrane [16]. Since lipids have a lower molecular weight than proteins far more lipids account to this mass as proteins. It has been estimated that 50 lipids are present for each protein [17]. Note, these values represent an average as they vary between organelles, cell types and organisms.

Lipids consist of a hydrophilic headgroup and a hydrophobic hydrocarbon tail (refer to **Fig. 2.1**), whereas proteins are folded chains of amino acids.

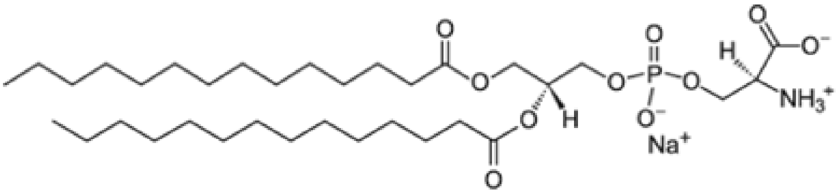

FIG. 2.1.: Exemplary structure of a phospholipid, here: *1,2-ditetradecanoyl-sn-glycero-3-phospho-L-serine* (DMPS) . Two hydrophobic hydrocarbon chains are coupled to a hydrophilic headgroup. DMPS has a chain length of 14 carbon atoms and a negative charge at the headgroup at physiological pH (p$K \sim 5$ of the -COOH group). Figure taken from [18].

Within a cellular membrane a variety of lipid types, mainly phospholipids but also cholesterol or sphingolipids, are present. Phospholipids differ in chain length and in modifications of the phosphate group located at the headgroup. This leads to variations in chemical properties, for instance, in the pK determining whether the headgroup is negatively charged at a given (physiological) pH.

Due to their amphiphilic structure phospholipids self-organize in aqueous regimes and build a bilayer framework in which the proteins are embedded.

Although lipids exhibit a polymorphism and can also aggregate into micelles, cubic ore tubular arrangements, a lamellar structure, the bilayer, is the here preferred structure in which the hydrophobic hydrocarbon chains are shielded. The hydrophilic headgroups are oriented towards the inner cell respectively the outer regime (**Fig. 2.2**) and are surrounded by a hydration shell.

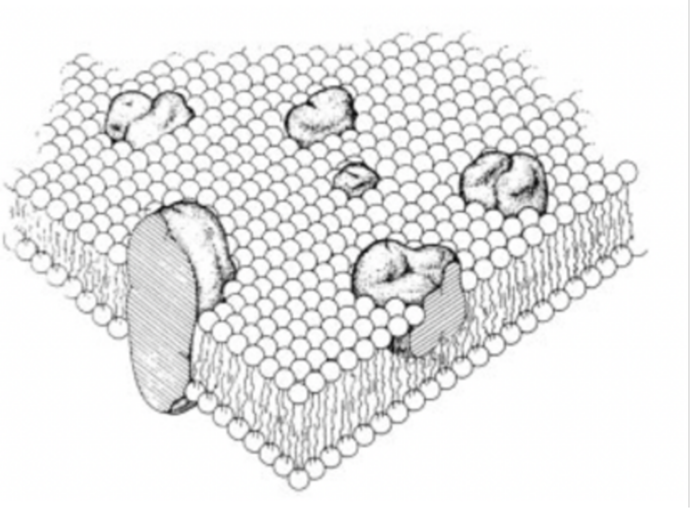

FIG. 2.2.: Scheme of a cellular membrane: A lipid bilayer framework with embedded proteins according to the fluid mosaic model of Singer and Nicolson. Figure taken from [19].

As already mentioned, the composition of lipid types and the share of embedded proteins vary across different cell types and cell organelles. To what extent the molecular composition determines cell functionality is unclear. However, a network of similar cell types can form a unit of specific functionalization as found in organs in more complex organisms. Significant differences between cell types are present, especially regarding the composition of the lipids. A comparison of the contribution of zwitterionic choline phospholipids (PC), negatively charged phosphatidylserine (PS) and cholesterol is presented in table 2.1.

	Mouse	**Human**		
	Neurons[a]	Brain[a]	Erythrocytes[b]	Mitochondria[c]
PC	30 % - 40 %	34 %	17 %	50 %
PS	7 % - 11 %	11 %	6 %	2 %
Cholesterol	25 % - 35 %	-	45 %	< 5 %

[a] Tissue; [b] Plasma membrane; [c] Outer plasma membrane

TAB. 2.1.: Lipid compositions of different cell types divided to the appearance of choline phospholipids (PC), phosphatidylserine (PS) and cholesterol. The percentages refer to the whole lipidome present in the cellular system at hand [20, 21, 16].

Biological membranes have also electrostatical attributes. For example, asymmetric compositions of lipid types in both leaflets of the bilayer induce a transmembrane potential due to asymmetrical surface charges. This has been suggested as a potential mechanism for signal transduction across the membrane in the 1970s by Träuble [22]. Indeed, an asymmetrical distribution of phospholipids, for instance, in both leaflets has been observed in mammalian cells [20]. The physiological environment is also marked by the presence of ions contributing to the transmembrane potential.

Since nerve pulses or external stimuli must be forwarded within an organism to evoke a response, they have to pass the cell membrane during the process. They are necessarily involved in information conduction which requires some sort of excitability of the membrane. Artificial, lipid membranes mimicking cellular membranes are commonly created for studying the latter. They are reduced to pure lipid membranes as the bilayer matrix is the essential macroscopic basis of a cellular membrane.

2.2. PHYSICAL STATES IN BIOLOGY

2.2.1. PHENOMENOLOGY OF PHASE TRANSITIONS

Phases states are displayed by stable states within a thermodynamic system characterized by certain parameters. During a transition between the phase states material properties change drastically and reflect a nonlinear behavior. For example, phase states of water are omnipresent, and the fundamental conformational differences are obvious for ice, fluid water and water vapor. Systematically, these differences can be characterized with an order parameter. For the liquid-gas transition of water the density is an established order parameter as it mirrors the symmetry breaking characteristic of the transition. Monitored upon temperature variation the density would reveal a nonlinear shift during the transition. However, temperature is not the only variable that can induce a phase transition. Also, other parameters such as pressure are thermodynamically relevant. Indeed, all these variables are coupled and the shift in one quantity does not solely define the system state.

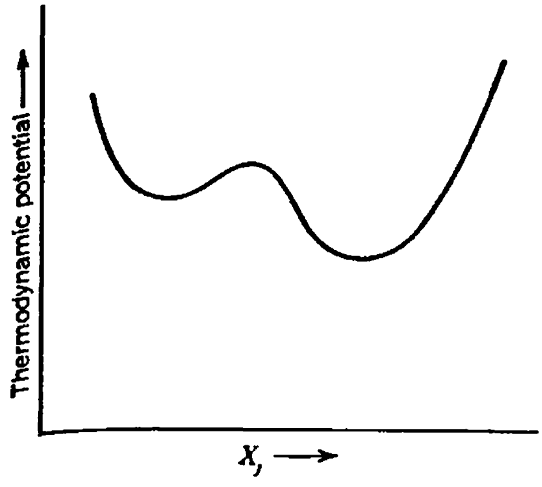

FIG. 2.3.: Exemplary thermodynamic potential with local minima at two states of the according variable X_i. Figure taken from [23].

The Landau theory approaches phase transitions phenomenologically. The free energy G is expanded in a Taylor series as a function of the order parameter in proximity to the transition [23]. This thermodynamic potential yields local minima (similar to **Fig. 2.3**) indicating the positions of stable states. The system will prefer the state at the global minimum and additional energy would be necessary to push the system into another (local) minimum reflecting another phase at otherwise constant conditions.

In a thermodynamic system the combination of several variables (pressure, temperature, volume...) determines its state. Thus, **Fig. 2.3** shows a snapshot rather than a complete state diagram as the potential will vary its shape depending on the setting of the other variables of the system. If the position of the global minimum shifts, another phase state is induced.

In summary, every combination of these parameters yields a new state but not necessarily a new phase state. Transition points are not universal in the sense that the transition temperature T_m is altered when the environmental conditions are changed. It is itself a function of pressure p etc. ($T_m(p, ...)$). For example, the boiling temperature of water is dependent on pressure and is reduced in areas with a lower atmospheric pressure. In particular, on top of the Mount Everest water boils already at 71 °C.
All of the relations between parameters mentioned above are illustrated using phase diagrams.

2.2.2. PHASE TRANSITIONS IN BIOLOGICAL SYSTEMS

Similar to water, lipid molecules, are known to undergo phase transitions and lipid systems can exist in different phase states. They feature structural rearrangements and a distinction is made between ordered and disordered states. The area density of the lipids (area per molecule) and the orientation of the tails are the underlying parameter for classification. Within a lipid bilayer the crystalline phase (L_C) is highly ordered and features an overall tilt angle of 0° for the hydrophobic tails. The gel phase (L'_β) is obtained upon heating and is still shaped by a uniform tilt angle ($\neq 0°$). Further heating crosses the so-called *main transition* and yields the fluid phase (L_α) marked by a disordered distribution of the hydrophobic tails (refer to **Fig. 2.4**).
The transition points of the lipids are defined by parameters as the length of the hydrocarbon chain or the charge of the headgroup. Thus, each lipid type has an associated individual melting temperature.

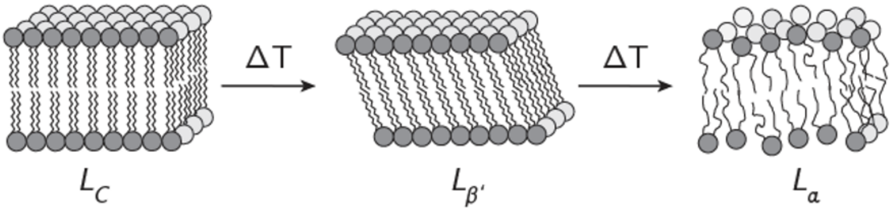

FIG. 2.4.: Phase states of lipid bilayers. From left to right: A lipid bilayer in a highly ordered crystalline phase (L_C) goes through a gel phase (L'_β) upon heating and arrives in the fluid, disordered phase (L_α) after further heating. Figure taken from [24] and adapted by [25].

PHASE TRANSITIONS IN CELLS

Lipids are main constituents of cellular membranes. Considering their presence and role within biological membranes it stands to reason that they are subject to investigations concerning phase transitions in cellular membranes. Indeed, there have been various experiments successfully demonstrating the existence of nonlinear material behavior in cellular ensembles interpreted as phase transitions.

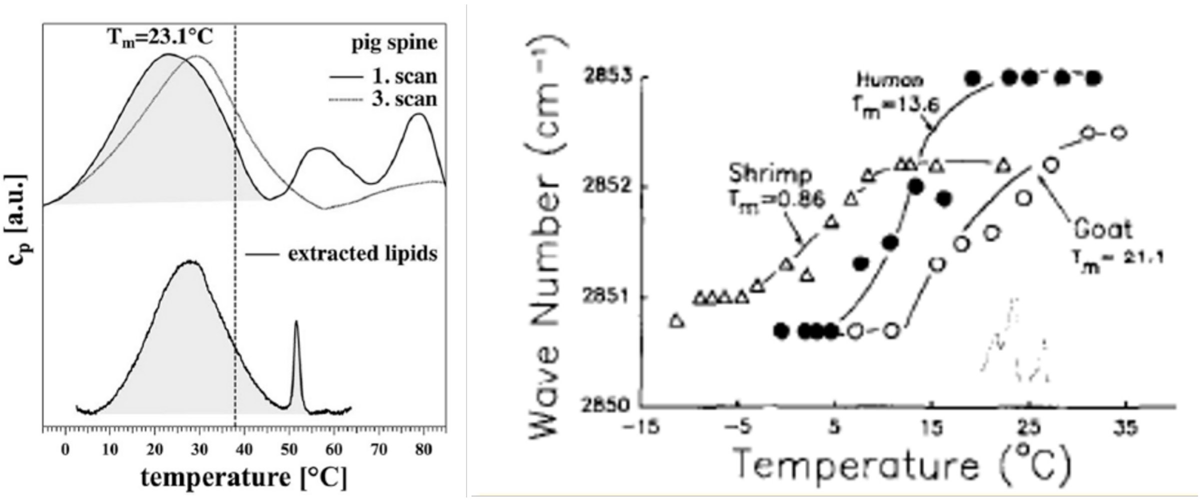

FIG. 2.5.: Left: Calorimetric measurement of membranes from porcine spinal cord cells and their extracted lipids. A phase transition is indicated upon the maximum in the heat capacity c_p. The dotted, vertical line around 37 °C indicates the body temperature of the pig. **Right**: FTIR measurements of sperm cells of different organisms. The nonlinearity in the wave number is indicative of a phase transition. The transition temperatures vary for the organisms according to their body temperatures. Figures taken from [11] and [14].

Phase transitions are typically detected within calorimetric measurements as the heat capacity c_p is a nonlinear feature during the transition. The change in *effective* temperature T - and consequently in enthalpy H - is not linear when a phase state transition occurs and is reflected in c_p [26]:

$$\partial H = c_p \partial T \tag{2.1}$$

This holds for isobaric conditions. An example is given in **Fig. 2.5** on the left. Porcine spinal cord cells show a maximum in the heat capacity profile accordingly to the extracted lipids of these cells. This nonlinearity is indicative of a phase transition. On the right in **Fig. 2.5** further examples of nonlinear material behavior in sperm cells extracted from shrimps, humans and goats are depicted. Via Fourier-transform infrared spectroscopy (FTIR) nonlinearities in the wave numbers, which are associated with chemical moieties of lipids, providing information about the phase state [14]. Examples of these nonlinearities are present throughout the literature [11, 14, 15, 10].

CONTROVERSY CONCERNING PHASE TRANSITIONS IN CELLULAR MEMBRANES

It is worth mentioning, that there are negative examples as well where certain cell types exhibit no such behavior respectively where it could not have been detected. In that context, different thoughts have been put forward to doubt the existence of phase transitions in cellular membranes. For one, the existence of relatively high amounts of cholesterol in cellular membranes would lead to a loss of the transition as it has been observed for pure lipid systems [27]. And secondly, the diversity of lipid types present in cells induces a similar distribution of transitions points and it is unclear to what extent a cooperative transition is still possible.

Nevertheless, evidence for cooperative and nonlinear material behavior has been provided manifoldly. It is important to note, that measurements are conducted solely on ensembles of cells or extracted lipids of these cells. Measurement directly in the intact cellular membrane have not been reported yet.

LIVING STATE

Assuming similar phase states as known for lipid interfaces a fluid-disordered-like and a solid-ordered-like phase state is proposed. Based on the data situation so far, it is indicated that membranes of organisms tend to exist in their disordered phase as the transition temperatures T_m are consistently found slightly below the growth respectively body temperatures of these organisms. It is worth mentioning, that the transition in sperm cells is not only linked to the living temperature but is also correlated to the temperature where these particular cells are lethally damaged [14]. While the body temperature of goats and humans differs around 2 °C the detected T_m differs by approximately 8 °C. While human sperm cells ($T_m = 13.6$ °C) can be cooled below room temperature without damage goat sperm cells ($T_m = 21.1$ °C) do not survive a similar cooling. Thus, it is strongly indicated that the physical state is crucial for functionality.

The role of the state itself is not fully explored. Indeed it seems a desired state in nature to have biological regimes close to their critical point. Adaptation experiments reveal that organisms or cells adjust to new growth conditions in the way that T_m is shifted but remains below and close to T_{growth} [11, 12, 13]. This relation appears qualitatively invariant to all adaptations for temperatures where limits of physiology are not yet reached (e.g. protein denaturation). One underlying mechanism identified for adaptions of the membrane is thereby the modulation of the lipid composition. In any case, it seems the preservation of the fluid disordered state is prioritized by organisms.

2.2.3. THERMODYNAMICS OF BIOLOGICAL INTERFACES

In the following the thermodynamics of biological interfaces is analytically examined. In *classic* thermodynamics a system is characterized via its partition function. Roughly speaking, based on the microstates and their distribution macroscopic quantities such as heat capacity can be derived. It is difficult to apply this established approach within a biological system as it requires a deeper knowledge of the system and its microstates. For that reason, an alternative approach from Einstein [28, 29] will be introduced here. Einstein himself criticized the famous equation of Boltzmann which links probability of states W and entropy of a system S ($S = \mathrm{k}\ln W$). He called it *useless* without a complete theory for the microstates and thereby disputed its use as a standalone tool in thermodynamics [28]. He suggested a new route to approaching a given system including an inversion of the methodology. It is based on the inversion of said Boltzmann equation after which a complete theory describing the microstates of the system is no longer necessary. Instead, the system's entropy gets accessible through measurable parameters respectively empirical behavior.

EINSTEINS INVERSION

Thermodynamic laws are universally valid and are here to begin with. The second law introducing the entropy S as a state function is of special interest and appears in different forms. With the Clausius theorem, valid for reversible and cyclic processes, it can be expressed as

$$\oint \frac{\delta Q}{T} = \oint \mathrm{d}S = 0 \tag{2.2}$$

with heat Q, temperature T and the definition of the entropy $S = \frac{\delta Q}{T}$. The line integral yielding 0 demonstrates that entropy is conserved within a reversible process. As a state function the entropy is path independent and owns all characteristics of a potential.
Boltzmann gave the principle of entropy a new shape in statistical physics as he linked entropy S with the logarithmic number of microstates W to a given observable macrostate. Hence, entropy can be interpreted as a measure for disorder and associated with a probability:

$$S = \mathrm{k}\ln W \tag{2.3}$$

Within the equation the proportionality factor k is introduced as the *Boltzmann constant*. W is a measure for the probability as it is proportional to the number of microstates belonging to a certain state. Einstein argued that in contrast to the (not observable) microstates, probabilities of macrostates can be determined.

According to him *every* state that is allowed at a given energy must appear and is merely limited by the observation time. In his words, the differences in orders of magnitude of the probabilities (~ number of microstates) between different states lead to the seemingly rare (or not at all) appearance of certain states [28].

The inversion of (2.3) yields:

$$W = \mathrm{e}^{\frac{S}{\mathrm{k}}} \tag{2.4}$$

For states close to the equilibrium a Taylor expansion of S around x_0 is introduced where x_0 is the value of an order parameter x at maximal entropy S_0. For the sake of simplicity merely one parameter x is considered here. Fluctuations around the equilibrium are expressed as $\delta x = x - x_0$.
Without loss of generality x_0 is set to 0 as a translation on the x-axis does not impact the shape of S. With that, $x = \delta x$ denotes (small) deviations/fluctuations from the equilibrium value x_0. The Taylor expansion yields for the entropy potential:

$$S(x) = S(0) + \frac{1}{2}\frac{\partial^2 S}{\partial x^2}\bigg|_{x=0} x^2 \tag{2.5}$$

As S is a potential its first derivative is similar to a thermodynamic force that is pushing the system back towards its equilibrium after a shift from state $S(0) = S_0$ to $S(x)$. The value with highest probability is $x = 0$ where the entropy has its maximum. The Taylor expansion only considers small deviations from x_0 and consequently these forces can be neglected $\frac{\partial S}{\partial x} \approx 0$. The second derivatives are linked to the thermodynamic susceptibilities. Terms of higher orders can be neglected as only *small* deviations of x are considered here. Most importantly, with this expression entropy becomes a function in which a value $S(x_i)$ can be assigned to each x_i and refrains from the association of S with a constant value. Inserting (2.5) into the inverted Boltzmann equation (2.4) yields an expression for W as a function of x_i:

$$W = W(x) = \mathrm{e}^{\frac{S_0}{\mathrm{k}}}\,\mathrm{e}^{\frac{1}{2\mathrm{k}}\frac{\partial^2 S}{\partial x^2}\big|_{x=0} x^2} \tag{2.6}$$

Consequently, a probability distribution is derived where $\mathrm{d}W$ describes a measure for the probability to find the variable x in the range between x and $x + \mathrm{d}x$ in a given state. Equation (2.6) has the form of a Gaussian distribution ($\backsim \exp(-\frac{x^2}{2\sigma^2})$) with variance σ^2. A comparison of coefficients results in

$$\sigma^2 = \left\langle x^2 \right\rangle = -\mathrm{k}\left(\frac{\partial^2 S}{\partial x^2}\right)^{-1} \tag{2.7}$$

where $\langle x^2 \rangle$ are the mean square fluctuations in x which are related to the second derivatives of the entropy potential [30]. From a mathematical point of view it is directly understood that a smaller σ^2 leads to a sharper maximum in the entropy potential $S(x)$.

In summary, each (macro-)state has an adjunct entropy potential $S(x)$ with an underlying probability distribution $W(x_i)$ of x_i (microstates). The most probable state is at $S(x = x_0)$ with x_0 the mean value where $W(x)$ and $S(x)$ have their maximum. But, it becomes clear as well that also other states of x_i are likely to occur. The entropy potential can be characterized upon macroscopic quantities since the second derivatives of the potential (curvature) are coupled to the thermodynamic susceptibilities. A *broad* potential allows many states of x to occur with a similar probability compared to $W(x_0)$. This results in fluctuations of x around the mean value rather than a constant x_0. Further, a broad potential has a low curvature and a high susceptibility.

Equation 2.7 provides a link between the entropy potential and measurable quantities. The derivative of the entropy S with respect to a parameter x can be written as

$$\left(\frac{\partial S}{\partial x}\right)_U = \frac{X}{T} \tag{2.8}$$

where X ist the corresponding generalized force of the parameter x. This relation can be retraced in the context of the first law of thermodynamics

$$\mathrm{d}U = \delta Q + \delta W \tag{2.9}$$

stating that the energy U is conserved upon an interplay of changes in heat Q and work W performed by the system. The work can be performed as mechanical, electrostatical etc. work according to the parameter at hand. A general formulation applying the total differential of U leads to:

$$\mathrm{d}U(S,x) = \left(\frac{\partial U}{\partial S}\right)_x \mathrm{d}S + \left(\frac{\partial U}{\partial x}\right)_S \mathrm{d}x \tag{2.10}$$

Using the definition of entropy $\mathrm{d}S = \frac{\delta Q}{T}$, the generalized force follows from the partial derivatives within the total differential of U as $X\mathrm{d}x$ describes the additional work when x is increased by $\mathrm{d}x$:

$$\mathrm{d}U = T\mathrm{d}S - X\mathrm{d}x \tag{2.11}$$

According to equation 2.10 the total differential of S can be set up and an expression for the first derivatives of S with respect to x derived:

$$\left(\frac{\partial S}{\partial x}\right) = \left(\frac{\partial S}{\partial U}\right)\left(\frac{\partial U}{\partial x}\right) = \frac{1}{T}X \tag{2.12}$$

Examples of conjunct variables are pressure $-p$ and volume V with the mechanical work $-p\mathrm{d}V$ or in a two-dimensional system, as it will apply for membranes, the lateral pressure $-\pi$ and the area A ($\delta W = -\pi \mathrm{d}A$). For charges q their adjunct force is the electrical potential $-\Psi$ and the electrostatical work $-\Psi \mathrm{d}q$ accordingly.
With that, equation 2.7 can be rewritten and simplified to

$$\left\langle x^2 \right\rangle = -\mathrm{k}T \left(\frac{\partial X}{\partial x} \right)^{-1} \tag{2.13}$$

and further, the following thermodynamic relations for the fluctuations in area A, enthalpy H and charge q are established:

$$\left\langle (\delta A)^2 \right\rangle = \mathrm{k}T \left(-\frac{\partial \pi}{\partial A} \right)_T^{-1} = \mathrm{k}TA\kappa_T \tag{2.14}$$

$$\left\langle (\delta H)^2 \right\rangle = \mathrm{k}T^2 \left(\frac{\partial T}{\partial H} \right)_\pi^{-1} = \mathrm{k}T^2 c_\pi \tag{2.15}$$

$$\left\langle \left(\delta q\right)^2 \right\rangle = \mathrm{k}T \left(\frac{\partial \Psi}{\partial q} \right)_{T,A}^{-1} = \mathrm{k}TC_T \tag{2.16}$$

Note, the fluctuations are denoted with δ to underline the character of a fluctuation ($\delta x = x - \langle x \rangle = x - x_0$) as a deviation from the mean value. Hence, fluctuations of A, H and q are coupled to the isothermal compressibility $\kappa_T = -\frac{1}{A}\left(\frac{\partial A}{\partial \pi}\right)_T$, heat capacity $c_\pi = \left(\frac{\partial H}{\partial T}\right)$ and respectively electrical capacity $C_T = \left(\frac{\partial q}{\partial \Psi}\right)_T$. These are measurable quantities. Moreover, for lipid membranes close to a transition a linear relationship has been established between changes in these susceptibilities [31]:

$$\Delta\kappa_T \propto \Delta C_T \propto \Delta c_\pi \propto \Delta\alpha_\pi \tag{2.17}$$

The isobaric area expansion coefficient α_π is proportional to the correlated fluctuations of A and H $\left\langle (\delta A \delta H) \right\rangle$. Thus, the behavior of one of these susceptibilities allows conclusions for the others as not all of them are easily accessible in every system.

APPLICATION TO LIPID INTERFACES

With that in mind, phase transitions in two-dimensional lipid interfaces are considered. The interface is considered thermodynamically independent with its own entropy. In the following, a typical state diagram of a lipid monolayer is presented. On a film balance the area per molecule A of a lipid monolayer is compressed at constant temperature T and the lateral (two-dimensional) pressure π is recorded simultaneously. A π-A diagram, called isotherm, is obtained analogous to a three-dimensional P-V diagram (**Fig. 2.6**).

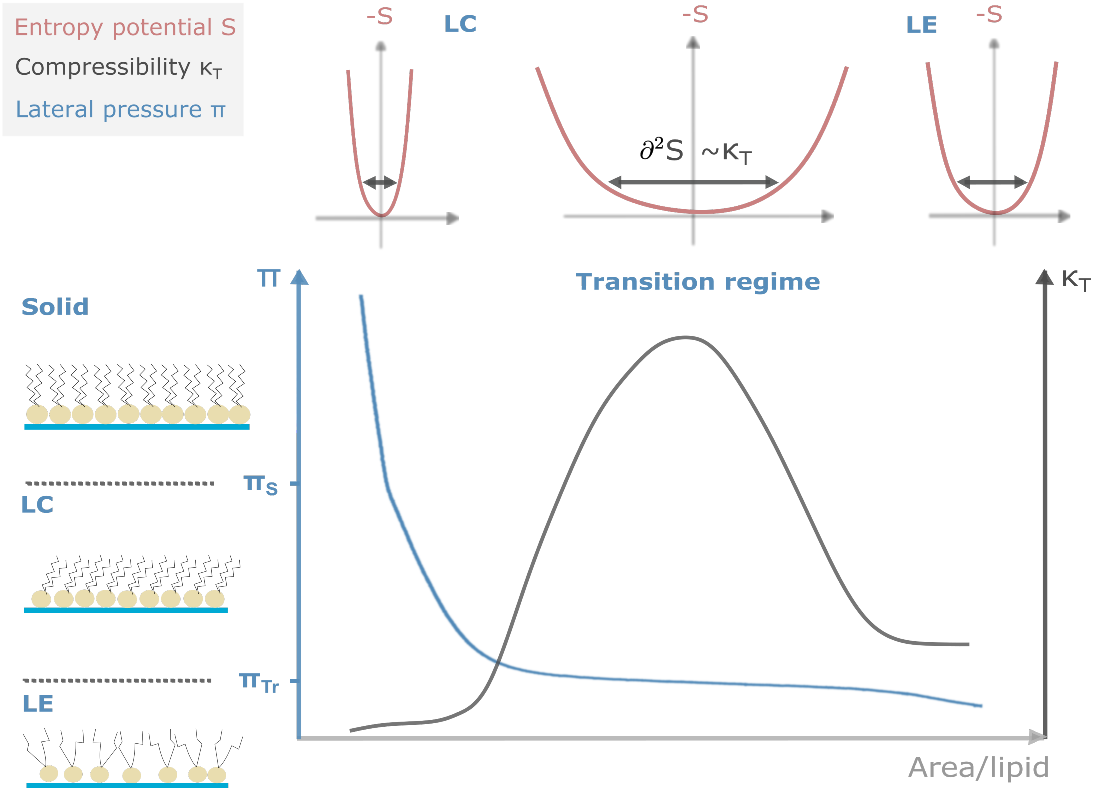

FIG. 2.6.: State diagram of a lipid monolayer. The isotherm (π-A diagram) is connected to the phase states of the lipids and entropy potentials. The phase states **LE**, **LC** and **solid** can be distinguished from the given isotherm. The compressibility κ_T provides information about the entropy potential S as the second derivatives of the entropy potential $\partial^2 S$ are directly coupled to κ_T and the fluctuations in A. Each state $\pi(A, T, ..)$, defined by a combination of variables, has an individual entropy potential. Here, exemplary entropy potentials are illustrated for LE, LC and the transition regime. Note, every *phase* state is a collection of individual states.

At low π values, once the monolayer has formed, the lateral pressure increases linearly upon compression of the area. In this region, the layer is in the *liquid expanded* phase (LE) until a plateau region is reached. Further compression does not lead to a significant increase in π as the latent heat is consumed to rearrange the inner order of the lipid layer. A transformation from an unordered to a more ordered phase, the *liquid condensed* (LC) phase takes place at the transition pressure π_{Tr}. The LC phase is characterized by uniformly tilted hydrocarbon chains in contrast to a randomly distributed orientation of the chains in the LE phase (refer to **Fig. 2.6**). Further compression induces the transition to the solid phase (at π_S). The transition point is visible in the isotherm by an indicated kink in the curve. In the solid phase the chains are still uniformly aligned but not tilted anymore. The transition between LE and LC phase is referred to as *main* transition. Additionally, **Fig. 2.6** demonstrates how conclusions about the entropy potential can be drawn from the isotherm.

The associated susceptibility is the isothermal compressibility $\kappa_T = -\frac{1}{A}\left(\frac{\partial A}{\partial \pi}\right)_T$ and describes to what extent the area changes upon a shift in π. It is a measure for the softness of the system and is directly derived from the π-A diagram. It becomes visible that κ_T gets maximized during the transition. From equation 2.14 the direct coupling of κ_T and the fluctuations in A is known. As stated before, it is possible to derive the shape of the entropy potential from measurable quantities as the second derivatives are equivalent to its curvature. Hence, during the transition the potential is broad as it yields a low curvature. Considering the interpretation of the entropy as a probability function, many states of A are probable and the fluctuations in A are maximal. Entropy potential shapes representative for the transition regime, LE and LC phase are illustrated in **Fig. 2.6** as they can be derived from the compressibility. Note, every point of the isotherm is defined by a combination of π and A describes one state of the monolayer. Accordingly, every state has an individual entropy potential. A phase state cannot be described by *one* entropy potential as a phase is a collection of states.

In summary, it can be derived from the state diagram that the lipid interface has maximal softness during the transition. The first derivatives of the potential, the restoring forces, get small in a broad potential and thus, relaxation is slow.

All other susceptibilities are coupled accordingly and feature similar phenomenological characteristics as to equation 2.17.

2.2.4. THE pH AS THERMODYNAMIC STATE VARIABLE

Classic thermodynamical variables are pressure, temperature or electric field but there are also chemical ones potent enough to act on the state of the membrane. The proton concentration of the bulk $[H^+]$ is specified by the pH value:

$$[H^+] = 10^{-\mathrm{pH}}$$

Molecules in membranes take up protons from the bulk if the pH goes below a specific value. Correspondingly, they release protons above this pH. This value is called the pK and has similar characteristics as a transition point in a two-state process. It determines at which pH a transition between the protonated and deprotonated form takes place in a specific molecule. Thus, lipid order phase transitions are not the only transitions present in membranes. Due to the presence of protonable groups in biomolecules there are protonation transitions in membranes as well. Lipids are either negatively charged or zwitterionic at physiological pH values (~ 7.4) depending on their headgroup. Thus, in general, cellular membranes have an overall negatively charged surface. For example, lipids with a phosphatidylserine headgroup (-PS) have a pK at ≈ 5.5 due to a -COOH group. They are sensitive for pH variations around that pK.

In a simplified electrostatical view, protonation of negatively charged headgroups induces condensation of the lipid interface because the repulsive forces between the headgroups are reduced. Thus, it is possible that the order state of the lipids is directly affected by that pH change. In any case, a shift in pH close to the pK where a membrane is receptive for protons has an effect on the state. Consequently, the system is pushed closer or away from its transition at constant temperature. By that, the transition temperature or respectively the transition pressure are expected to shift at otherwise constant conditions.

These are not only hypothetical speculations but have been investigated theoretically and experimentally before [22, 32, 9]. In 1977 Träuble published theoretical considerations concerning the effect of a surface potential Ψ^0 on the transition temperature T_m of a membrane. There are two crucial parameters for a surface potential. The first is the existence of surface charge σ at the membrane, modulated by pH of the bulk and the pK of the molecules. On the other hand there is the electrolyte concentration n of the bulk determining the Debye length κ ($\kappa \sim \sqrt{n}$) which is a measure for the range of electrostatic effects of the membrane into the bulk.

In the Gouy Chapman theory a charge redistribution in the vicinity of a statically charged surface or interface is assumed. A negatively charged surface attracts positive charges from the bulk which then accumulate and form another *layer* of charges close to the charged interface in that kind that a surface potential Ψ^0 is generated (refer to **Fig. 2.7**). This effect attenuates with a larger distance to the membrane within the bulk. A measure for the thickness of this layer is the Debye length κ

$$\kappa^2 = \frac{8\pi}{\epsilon}\frac{\mathrm{e}^2}{\mathrm{k}T}n \tag{2.18}$$

where k is the Boltzmann constant, ϵ the dielectric constant and e is the elementary charge. The attenuation of the electrical potential Ψ happens exponentially with the length constant κ as it is visible in **Fig. 2.7**. At the distance $\frac{1}{\kappa}$ the potential is reduced to $\frac{\Psi^0}{\mathrm{e}}$ with e denoting the Euler's number. From equation 2.18 it becomes clear that the thickness of the layer of counterions is limited and is merely determined by the salt concentration n. With increasing n the effective length ($\frac{1}{\kappa}$) gets smaller.

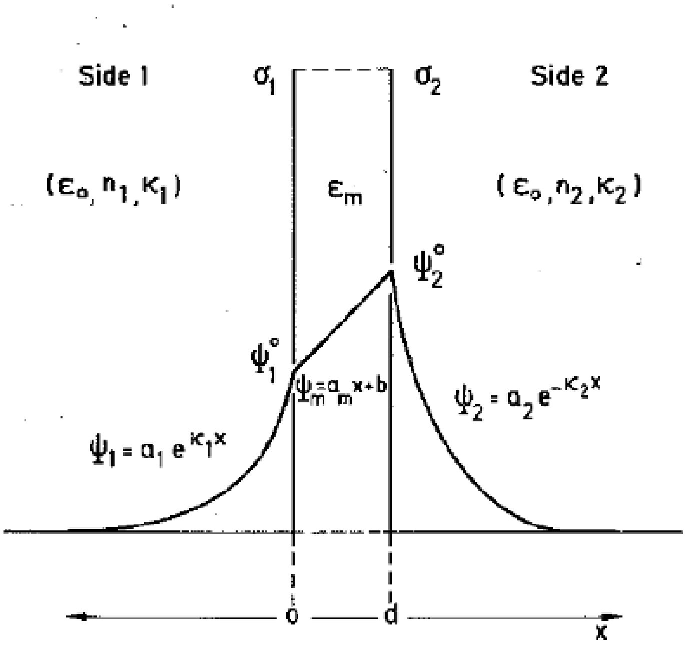

FIG. 2.7.: Surface potentials $\Psi^0_{1,2}$ at two sides (1,2) of an asymmetrically charged double layer ($\sigma_{1,2}$) with charge specific characteristics such as Debye length $\kappa_{1,2}$, salt concentration $n_{1,2}$ and the dielectric constants of bulk (ϵ_0) and membrane (ϵ_m). According to the Gouy Chapman approach the emerging surface potential decays exponentially to each side with the characteristic penetration depth of $\kappa_{1,2}$. Given the asymmetry, a surface potential gradient $\Delta\Psi^0$ across the membrane arises and an additional electrical field with $E = \frac{\Delta\Psi^0}{d}$ is created where d is the width of the membrane. Figure taken from [22].

The relation between electrolyte concentration n, surface charge σ and the surface potential Ψ^0 can be summarized in the following equation according to [32]:

$$\Psi^0 = 2\frac{\mathrm{k}T}{\mathrm{e}}\sinh^{-1}\left(\frac{2\pi\mathrm{e}}{\epsilon\mathrm{k}T}\frac{\sigma}{\kappa}\right) \tag{2.19}$$

It is important to note, in terms of identical surface charges on both sides $\sigma_1 = \sigma_2$ of a bilayer membrane but different salt concentrations $n_1 \neq n_2$ this would still result in $\Delta\Psi^0 \neq 0$ and a *transmembrane* potential would be induced. In other words, a gradient across the membrane would be measurable.

A *semi*quantitative relation was derived by Träuble for the shift in T_m dependent on σ and κ representing the effects of pH and n respectively on the surface potential [22]:

$$\Delta T_m = -2\frac{kT}{\mathrm{e}}\frac{\mathrm{N_A}}{\Delta S^*}\Delta A \quad \sigma \quad + \quad \frac{\epsilon}{\pi}\left(\frac{kT}{\mathrm{e}}\right)^2\frac{\mathrm{N_A}}{\Delta S^*}\Delta A \quad \kappa \tag{2.20}$$

In this equation, changes in the area per molecule ΔA and in the entropy of an uncharged membrane ΔS^* between two phase states (expanded and condensed) are involved. The Avogadro constant is denoted with $\mathrm{N_A}$.
This relation states that an increase in surface charge σ means a respective decrease in the transition temperature T_m. The increase in σ can be induced by a pH shift (acidification) close to the membranes' pK. An elevated salt concentration n would counteract but to a smaller extent since κ is merely proportional to the square root of n.

In the following, it will be elaborated on the starting points of the derivation of equation 2.20. The ideas will be roughly sketched, yet it will be refrained from demonstrating the whole derivation. It can be retraced in the works of Träuble [22, 32].
With the Gouy Chapman theory a surface potential Ψ^0 of the membrane is introduced as shown above in equation 2.19. Thermodynamically, an additional electrostatic free energy ΔG^{el} emerges on a charged surface.
The charged version of a membrane has different characteristics compared to the identical membrane *without* charges as an additional, state-potent parameter (surface charge σ) is introduced. The Gibbs free energies of two phase states G_A and G_B are identical at the transition point between these states

$$G(T_m) = G_A = G_B \tag{2.21}$$

but an additional term for electrostatic interactions, the electrostatic free energy G^{el}, is considered if the surface is charged [32]:

$$G_{A,B} = G^*_{A,B} + G^{\mathrm{el}}_{A,B} \tag{2.22}$$

Here, $G^*_{A,B}$ represents the corresponding Gibbs free energy for the uncharged but otherwise similar membrane. In the following, variables denoted with $*$ represent the uncharged membrane. The general definition of the Gibbs energy is

$$G = H - TS \tag{2.23}$$

where H denotes the enthalpy and S the entropy. Applied to equation 2.21 (valid at $T = T_m$) an expression for T_m of an uncharged membrane can be derived to

$$H_A - T_m S_A = H_B - T_m S_B \tag{2.24}$$

$$\Leftrightarrow T^*_m = \frac{\Delta H^*}{\Delta S^*} \tag{2.25}$$

with $\Delta H^* = H_B - H_A$ and $\Delta S^* = S_B - S_A$ respectively. Equation 2.21 holds true for the extended Gibbs free energy of a charged membrane as well:

$$G^*_A + G^{el}_A = G^*_B + G^{el}_B \tag{2.26}$$

Consequently, using equation 2.24,

$$\Delta G^{\mathrm{el}} = G^{\mathrm{el}}_B - G^{\mathrm{el}}_A = -\Delta H^* + T_m \Delta S^* \tag{2.27}$$

can be derived. Solving for T_m leads to:

$$T_m = \frac{\Delta H^*}{\Delta S^*} + \frac{\Delta G^{\mathrm{el}}}{\Delta S^*} = \frac{\Delta H^*}{\Delta S^*} + \Delta T_m \tag{2.28}$$

The latter term in 2.28 can be summarized to ΔT_m as it describes the resulting shift in T_m for charging the membrane compared to $T^*_m = \frac{\Delta H^*}{\Delta S^*}$ for the uncharged layer.

A link between G^{el} and the surface potential Ψ^0 is provided by the surface electrostatic free energy density Φ as $G^{\mathrm{el}} = \mathrm{N_A} A \Phi$ with Avogadro constant $\mathrm{N_A}$, molecular area A and

$$\Phi = \int_0^\sigma \Psi(\sigma')\mathrm{d}\sigma' \quad . \tag{2.29}$$

The integral resembles the work per area in a charging process from 0 to σ. The outcome of the integral is:

$$\Phi = \sigma\Psi^0 - \frac{\epsilon}{\pi}\left(\frac{\mathrm{k}T}{\mathrm{e}}\right)^2 \kappa \left(\cosh\left(\frac{\mathrm{e}\Psi^0}{2\mathrm{k}T}\right) - 1\right) \tag{2.30}$$

Combined with the expression for ΔG^{el} derived from a Taylor expansion around state A and $\frac{\mathrm{d}\Phi}{\mathrm{d}A} = -\frac{\Psi^0\sigma}{A}$

$$\Delta G^{\mathrm{el}} = \mathrm{N_A}\left(\Phi - \Psi^0\sigma\right)\Delta A \tag{2.31}$$

equation 2.20 can be derived in principle.

It is underlined that electrostatics affect the membrane structure. The relation has been verified experimentally as well [9, 10, 22, 33]. In general, it requires that the membrane is receptive to protons in the investigated pH range, which is determined by the pK. The surface charge σ is then controlled via pH. Protonation (induced by acidification) reduces negative charges at the headgroups in the case of negatively charged headgroups (e.g. -PS at pH < 5.5). Zwitterionic (i.e. net neutral) headgroups would indeed become charged but at rather unphysiological pH values (e.g. -PC at pH < 2). Consequently, repulsive forces decrease and the membrane gets more condensed at otherwise constant conditions. By that, it is in principle possible to induce a phase transition at otherwise constant parameters as temperature T if certain conditions are fulfilled. Note, beside pH ionic strength and divalent cations are potent parameters as well.

From these electrostatical considerations impacts for lipid bilayers or even cellular membranes can be derived. The leaflets of bilayers are electrostatically coupled. It was stated before that similarly charged membranes still provide a transmembrane potential if the electrolyte concentrations differ.
In cellular membranes there is a lipid bilayer framework. A heterogeneous composition of lipids is present which differs between the leaflets. The mutual electrostatical interaction can enhance a phase separation within one leaflet.
Protons can be released by proteins. Hence, proteins induce local pH variations enhancing a phase separation or modulating the transmembrane potential. In turn, a process on the other side of the membrane can be triggered. Membranes can act as a proton sink. Conversely, protons can be released by the membrane into the bulk (upon a pH shift) due to conformational changes in the membrane. These pathways open up potential ways of signal transduction - and thereby communication - within or across cells.

2.3. FROM STATE TO FUNCTION

2.3.1. STATE-DEPENDENT FUNCTIONALITY OF LIPID INTERFACES

Fluctuations diverge when the system enters a critical state. The coupling between fluctuations and susceptibilities provides a basis for inducing function into lipid interfaces. **Figure 2.8** provides an overview over selected functions induced or enhanced by phase transitions.

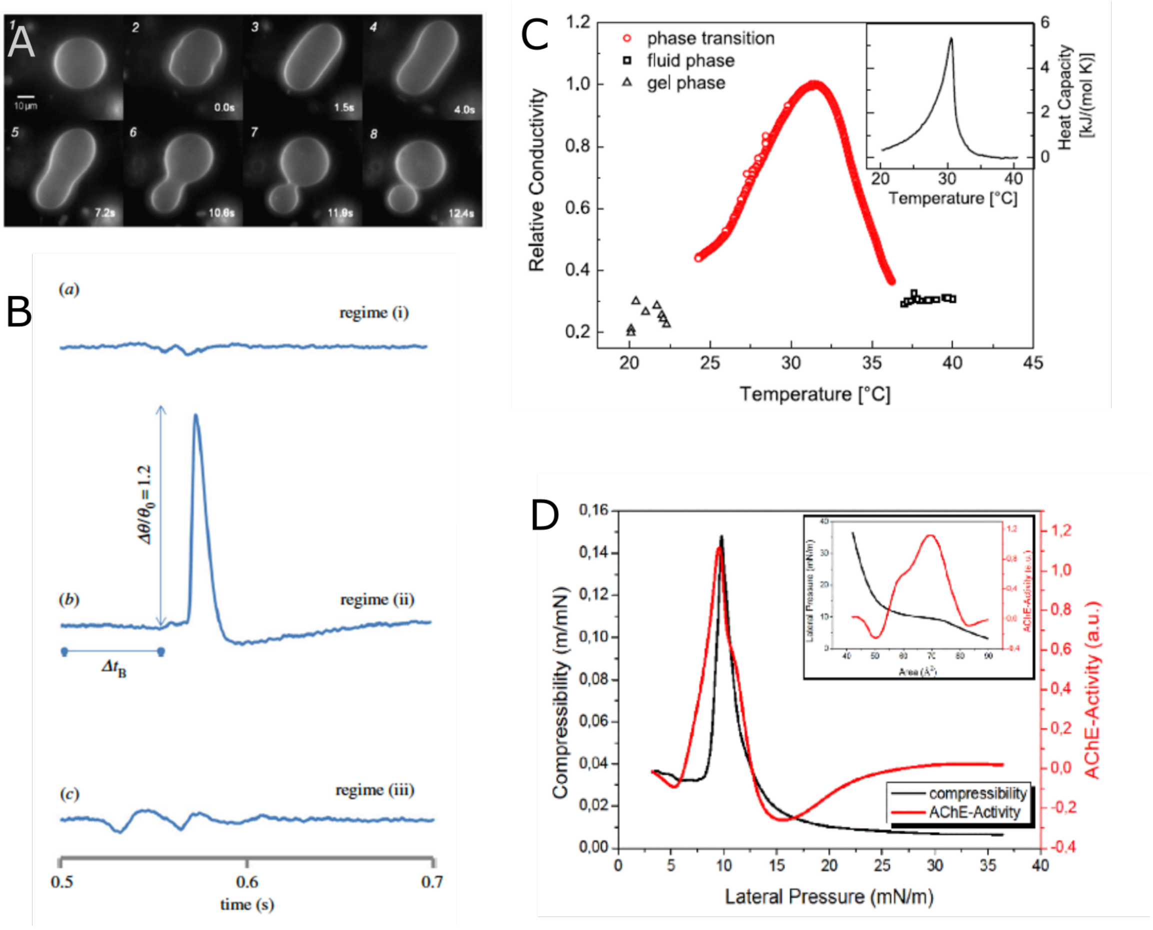

FIG. 2.8.: Examples for state dependent functions in *pure* lipid membranes A: Morphological changes - State induced fission in lipid vesicles upon heating across the phase transition temperature [34]. B: Excitability as a function of state - Triggering of nonlinear acoustic pulses is merely possible when the interface is close to its transition regime at a given excitation strength (regime (ii) in *b*). At all other states (regime (i) and (iii)) an excitation of a pulse is not possible with a similar excitation strength [5]. C: Permeability - Phase state dependent current fluctuations in lipid bilayers [4]. D: Catalysis - State dependent enzyme activity in lipid monolayers [35, 36]. Figures taken from [4, 5, 34, 35].

MORPHOLOGY

As discussed before in the context of monolayers the softness of the interface is drastically increased during the transition. For the bending elasticity κ_{bend} of bilayers the following relation holds [37, 38]

$$\kappa_{bend} = \frac{2\kappa_T^{mono}}{h} \tag{2.32}$$

where κ_T^{mono} denotes the compressibility of a monolayer and h the distance between both leaflets. Hence, this phenomenological behavior holds for bilayer systems as well. Experimentally, the increased bending elasticity is reflected in morphological changes in lipid vesicles, while heating through their phase transition (refer to **Fig. 2.8** A). Vesicle feature first an elongation upon increased elasticity and further a fission.

CONDUCTIVITY

Another arising phenomenon is pore formation in the lipid interface due to the area fluctuations. As to

$$(\Delta A)^2 \sim \kappa_T \tag{2.33}$$

the pore size $(\Delta A)^2$ is proportional to the compressibility of the interface [39]. Ion conduction via the interface is a measurable consequence of this relation. A phase dependent conduction was verified upon permeability measurements on lipid bilayers (**Fig. 2.8** C) [4]. These results are remarkable as they resemble conductivity traces measured on membranes containing ion channel proteins. In both cases, a stepwise current flow is observed. Thus, a doubtless allocation of conduction events to the ion channels is not possible.

CATALYSIS

The fluctuations do not only affect the lipid membrane itself but embedded molecules inevitably couple to the thermodynamic entity of the interface and its hydration shell. Consequently, they are affected by a transition as well. A theory was put forward by Konrad Kaufmann concerning enzyme catalysis enhanced by fluctuations [40]. The underlying relation between fluctuations in the reaction coordinate ξ and the catalytic rate k is given by [25]:

$$\left\langle (\delta\xi)^2 \right\rangle \sim k \tag{2.34}$$

Due to the coupled system of membrane and membrane-bound enzymes the fluctuations in the parameters appear simultaneously. This relation is shown in **Fig. 2.8** D where a phase transition is induced in lipid monolayers containing embedded Acetylcholinesterase.

EXCITABILITY

Due to momentum conservation perturbations in a lipid membrane propagate as pulses. They are triggered by local perturbations as a consequence of a local shift in density or pressure, temperature, pH etc. The state of the lipid interface thereby affects the nature of the pulse propagation. The pulses are adiabatic and feature characteristics of acoustic pulses including their velocity c profile:

$$c \sim \sqrt{\frac{1}{\kappa_S}} \tag{2.35}$$

The adiabatic compressibility κ_S itself is a susceptibility with a similar state dependent behavior as κ_T [41]. In general, linear pulses are excitable in every state but with state dependent quantities such as velocity c, amplitude and attenuation β ($\beta \sim \sqrt{\kappa_S}$) [42]. Thus, the propagation velocity is at its slowest during the phase transition and the attenuation is strongest.

Given the nonlinear material properties (compressibility, thermal expansion coefficient, ...) nonlinear pulses are excitable under certain conditions as well (refer to **Fig. 2.8** D). Close to the phase transition regime solitary waves are have been observed when overcoming an excitation threshold [5].

ROLE FOR CELLULAR FUNCTIONALITY?

These effects are not necessarily limited to artificial membrane systems. Their lipid bilayer framework allows to transfer the line of arguments consequently to cellular membranes as well. The presence of a phase transition in the cellular membrane would, however, be required.

As stated before the membrane is inevitably involved in signal conduction within or between cells. The information has to somehow cross the membrane or otherwise be passed along the membrane. Usually, these processes are approached on a molecular level by an interaction of hormones, receptors and proteins (e.g. ion channels). From the aforementioned relations a rather macroscopic approach based on the thermodynamics of the membrane would be conceivable as well.

A pulse, triggered by local perturbations as they are omnipresent in living systems (local acidification or external stimuli) would inevitably propagate as to momentum conservation. Due to the ability of the lipid interface to transduce these local events an integration of the membrane into the communication pathways is most likely.

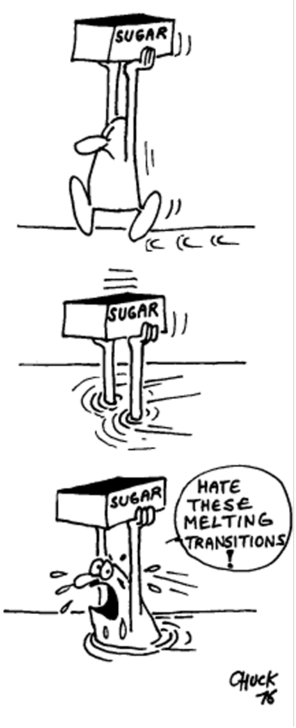

FIG. 2.9.: Figure taken from [43].

It could be indeed demonstrated that pulses on model membranes are excitable upon local acidification (protonation of headgroups). Additionally, pulses are able to even modulate the activity of enzymes during their propagation making them highly biologically relevant [40].

Beside a mechanic mechanism of signal transduction another mechanism based on the interplay between electrostatics (surface potential of the membrane) and structural changes at the membrane were already proposed by Träuble in 1977 [22]. His approach is remarkable as it gets by without transmembrane transport which is necessary in the classic theory relying on ion channel or receptor proteins. The electrolyte environment is able to induce structural changes in membranes but also vice versa, phase transitions, coming along with great structural changes, can affect e.g. the pH. This is based on the interpretation of the (cellular) membrane as a reservoir of protons and divalent cations which can be released due to these structural changes.

Within living organisms evidence has been provided for an effect of the membrane state on cellular (transport) function. For instance, in the bacterium *Escherichia coli* (*E.coli*), phase transitions have been measured in the membrane. An associated, simultaneous nonlinear increase in the transport rate of sugar was detected [43, 9].

2.3.2. NERVE PULSE CONDUCTION FROM A THERMODYNAMIC POINT OF VIEW

During nerve pulse conduction a signal can be conducted over macroscopic distances from the location of the stimulus to its receiver (for example the brain). This requires an effective and cooperative mechanism based on a molecular highly heterogeneous environment (as to the composition of the cellular membrane and the cell itself).
Classically, it is perceived as an electrical mechanism and described by the propagation of action potentials (AP). These are nonlinear pulses yielding a threshold behavior for excitation and are characterized by their electrical phenomenology since a depolarization and subsequent repolarization of the membrane is measured during the propagation.
Molecular mechanisms have been put forward for interpretation assuming ion currents through the membrane due to the opening of voltage-dependent channel proteins [3]. The induction of ion flow through the membrane upon depolarization in turn modulates the transmembrane potential. By that, a self-sustaining mechanism is provided and the electrical stimulus propagates further. The membrane potential is an electrochemical potential which occurrence is classically explained based on the existence of ions (K^+, Na^+, Cl^-) and their variations in intra- and extracellular concentrations (Nernst potential). In the classic theory the membrane has all attributes of an electrical capacitor and the ion channels are interpreted as resistors.

The findings of structural-functional relationships and their similarity to processes in living systems combined with the observation of nonlinear responses in cells encouraged the development of new ideas concerning biological signaling. For example, during action potentials thickness variations in squid nerve axons were detected [44, 45]. In the classic theory the capacitance of the membrane is assumed constant. However, a variation in the membrane thickness would lead to modulated parameters for an electrical capacitor analog as membrane thickness equals the plate separation. Hence, this assumption may not hold. Changes in the membrane potential could instead be explained by changes in the area density of (charged) lipids [7].

Träuble derived from his experiments on transport rates in cells a hypothesis of abrupt (cooperative) conformational changes occurring in the axonal membrane during excitation [9]. It culminated in an attempted emancipation from the established, purely electrical model for describing action potentials and consideration of morphological changes of the membrane as well [46, 9, 44, 45].

A holistic approach was introduced by K. Kaufmann who proposed a thermodynamic theory for describing nerve pulse propagation. In contrast to the electrical approach an adiabatical (acoustic) phenomenon was considered that lived up to measurements during action potentials that could not be explained before. For one, there were the thickness changes in the nerve and on the other hand, a reversibility of heat uptake during the action potential was observed inconsistent with an electrical approach [47]. More precisely, an AP is proposed as a propagating, local phase transition within the cellular membrane [6, 7, 8]. This was also indicated by Tasaki who measured a phase transition in squid axons by fluorescence [44].

A specialty of thermodynamics is the coupling of all variables. It is not possible to merely consider one variable as one is not enough to define a state. Hence, a propagating transition would modulate all variables in that system (pressure, temperature, electrical field...) and induce fluctuations in them. From the section before it is known that transitions have the potential to induce manifold processes. Ion conduction is not merely a feature of proteins but could be explained by area fluctuations of the membrane. A thickness variation in the membrane during excitation is able to explain the variations in membrane potential that are characteristic for the electrical phenomenology of APs [48].

In principle, the existence of acoustic pulses with the required phenomenology has been demonstrated on artificial lipid membranes. They resemble characteristics such as nonlinearity and threshold behavior [5, 49]. The hypothesis of propagating phase transitions in cellular membranes requires the existence of distinct membrane states. The excitation of these pulses is then linked to a sharp transition between these states. Hence, the phase state of an excitable cell membrane must be close to its phase transition regime at physiological conditions. Due to the highly nonlinear nature of the action potentials a rather sharp phase transition in the membrane would be necessary.

3. OPTICAL CHARACTERIZATION OF THERMODYNAMIC STATES IN LIPID INTERFACES

In the following, physical phase states of biological membranes are approached. The previously introduced thermodynamic methodology allows to make predictions concerning the lipid interface via its susceptibilities. The goal is to monitor state diagrams from which the susceptibilities (macroscopic observables) such as compressibility or heat capacity can be extracted. Their coupling to the systems fluctuations enables the identification of thermodynamic states. However, accessibility is a challenge in biological systems and the localized monitoring of a state variable is mostly not straightforwardly possible. Established methods for recording state diagrams of biological samples such as calorimetry have limits concerning their sensitivity. In calorimetric measurements the change in enthalpy ∂H is monitored via the heat transfer ∂Q. With $\partial H = c_p \partial T$, which holds for isobaric conditions ($\partial p = 0$), the heat capacity c_p profile can be determined. This approach usually requires large amounts of sample material and is especially not sensitive on a single cell level.

A more sensitive method is needed allowing localized measurements on single cells and their membrane. It shall be applicable to distinguished artificial membrane systems as well as living systems in their *natural* conformation (adhesive cells).
For that, an optical approach is pursued. Clamping fluorescent dyes as local sensors of thermodynamic state via their spectral emission properties allows a direct observation of state. The thermodynamic coupling of observables is expanded to optical parameters based on the integration of the dye into the thermodynamic entity of the interface and its solvation shell. In the following, this method is introduced (section 3.1) and the characterization based on artificial, pure lipid membranes conducted (section 3.2). Additionally, a fluorescence correlation spectrometer is introduced and its ability to investigate kinetics on a molecular level by fluorescence. It allows the investigation of timescales within the system at hand and is applied for the investigation of state-dependent diffusion times and protonation rates (section 3.3). In principle, by that, a combined observation of state and function is possible.

3.1. FLUORESCENT DYES AS LOCAL STATE REPORTERS

The incorporation of fluorescent dyes into biological systems is not only suitable for imaging. The emission properties of the dyes themselves, such as the emission spectrum or the fluorescence lifetime, can be revealing parameters as well as they can be brought into connection with thermodynamic properties. It is an established method by now to use fluorescent dyes for reporting on the phase state of the surrounding lipid system [50]. By that, optical parameters take the role of a state variable/function within a thermodynamic ensemble or here, the lipid interface.

Although embedding fluorescent dyes into biological membranes seems invasive, there is the huge advantage, that the system must not be altered otherwise (e.g. in terms of conformation). This is especially relevant when it comes to living systems. With this technique they can be observed in their *natural* environment or conformation. Low dye concentrations within a highly sensitive detection setup can ensure a minimized effect of the dye molecules on the systems state in general.

In the following, after an introduction to fluorescence, the photostable dye *Atto488 DPPE* is introduced and it will be demonstrated how it is well suited for this kind of application.

3.1.1. FLUORESCENCE

Fluorescence means the emission of a photon after excitation of a molecule into a higher electronic state and, in course of the deactivation, subsequent transition from the singlet state S_1 back to the ground state S_0.

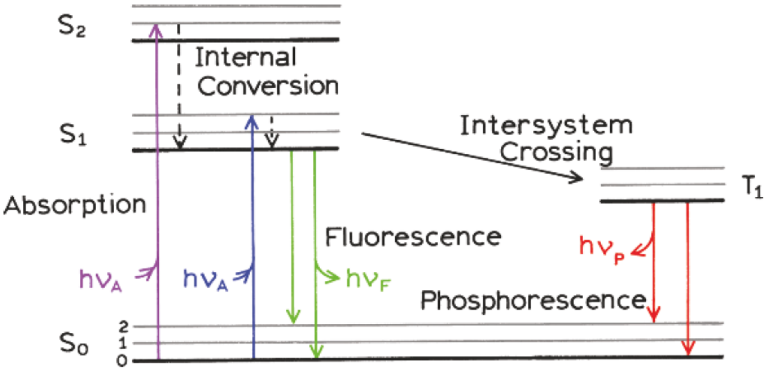

FIG. 3.1.: Jablonski diagram: Electronic states of a molecule and the potential transitions as a term diagram. Figure taken from [51].

Molecules exhibiting fluorescence, dyes, are receptive to photons with certain wavelengths, depending on the energy levels within the given molecule. After absorption of an incoming photon with frequency ν_A and the energy $E_{ab} = \mathrm{h}\nu_A$ the molecule transitions to a higher electronic state (as depicted in **Fig. 3.1**). Between additional vibrational levels or higher electronic levels (e.g. S_2) deactivation happens mostly non-radiative until the lowest vibrational level in S_1 is reached. Consequently, the emitted photon representing the transition between S_1 and S_0 has a lower energy $E_{em} = \mathrm{h}\nu_F$ than the absorbed photon, which is commonly referred to as Stokes shift. In terms of wavelengths this describes a shift of the emitted photon to longer wavelengths.

Although merely photons with defined wavelengths are able to excite a fluorescent molecule there exists a continuous absorption as well as emission spectrum. As visible in the Jablonski diagram in **Fig. 3.1** several vibrational levels and higher electronic levels allow a spectrum of energies for excitation respectively emission.

According to timescales the process of fluorescence happens in the nanosecond range. Transition into a higher ordered singlet state preserves the spin direction of the electron allowing a fast relaxation of the molecule. In rare cases the spin is inverted upon excitation and the subsequent intersystem crossing. The molecule is in its triplet state T_1 and has two parallel oriented spins. The ground state S_0 with two parallel oriented spins is quantum mechanically forbidden, and the time for relaxation is order of magnitudes longer than the fluorescence process. The relaxation from the triplet state is called phosphorescence.

3.1.2. SOLVATOCHROMISM

The position of energy levels within a molecule as depicted in a term diagram is not only unique for different structures of molecules/fluorophores but the observed Stokes shift depends on the surrounding solvent as well. Thus, the same molecule might have distinguished levels when embedded in different types of solvents and consequently different emission spectra.

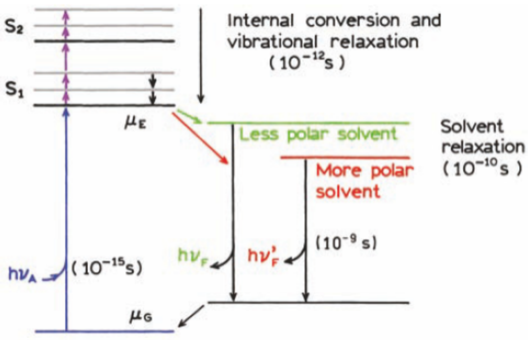

FIG. 3.2.: Jablonski diagram with effects due to solvatochromism. Figure taken from [51].

The excitation of the dye molecule affects also its dipole moment and its orientation because a charge shift happens within the molecule upon the electronic transition. The surrounding solvent reacts to that change and reorientates accordingly as a consequence of the interaction between the solvation shell of the fluorescent dye and solvent molecules. As a consequence of *solvent relaxation* energy levels of the excited state are lowered compared to an apolar solvent. The shift depends among others on the polarity and dielectricity constant of the solvent. As the *solvent relaxation* happens typically on much faster timescales ($\sim 10 - 100$ ps) than the fluorescence itself (~ ns) the solvent relaxed state determines the gap between the energy levels and consequently the emission spectrum of the fluorophore (**Fig. 3.2**) [51, 52]. This characteristic is referred to as solvatochromism. The timescale of the relaxation process determines whether a solvatochromism effect is measurable. If the relaxation process takes longer than the dye stays in its excited state (lifetime) no significant effect is present.

Phase states in lipids are featured by their distinguished structural order. Given the dipole moments of the lipid layer, they are expected to vary significantly between the ordered and disordered state. Especially, since the ordered state includes an uniform tilted chain of all lipids.
Thus, a lipid interface as *solvent* of the dye provides significantly different chemical properties for the dye dependent on the phase state. If a dye reveals solvatochrome characteristics it will be influenced differently in each phase and an altered emission signal of the dye characteristic for each phase state is expected. This scenario is depicted in **Fig. 3.3** as well.

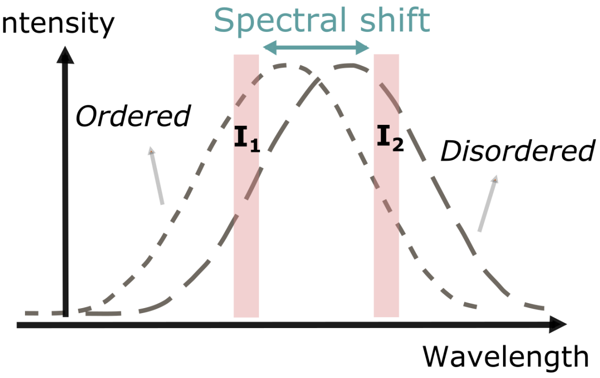

FIG. 3.3.: Spectral shift in the fluorescence emission spectrum. Two wavelengths are indicated where changes in intensities $\mathbf{I_1}$ and $\mathbf{I_2}$ would reflect the spectral shift. For the sake of simplicity a model with two potential states is introduced. Each spectrum is associated to one phase (here: ordered vs. disordered).

3.1.3. INTRODUCTION OF *ATTO488 DPPE* AS STATE REPORTER

At first chosen for its photostable characteristics the dye *Atto488 DPPE* became exemplary for a dye reflecting a coupling to the surrounding system in this study. It consists of the hydrophilic dye *Atto488* coupled to the head group of the zwitterionic lipid dipalmitoylphosphatidylethanolamine (DPPE). Due to its photostability *Atto488* is mainly used throughout this work as it resists laser excitation, which is used in the later introduced confocal setup.

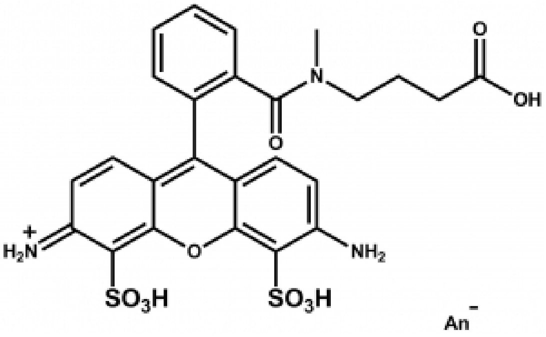

FIG. 3.4.: Chemical structure of *Atto488*. Figure taken from [53].

Although not yet reported for a sensitivity towards its chemical environment, the dependent behavior of the dye is already visible by eye: A stock solution of 0.5 μM *Atto488 DPPE* in dimethyl sulfoxide (DMSO) is stored in the fridge at 7 °C where it is in its frozen state and appears in a red-pink color (**Fig. 3.5**). DMSO has its melting temperature at 18.5 °C ([54]), around room temperature, where simultaneously the color of the solution changes to yellow when it becomes fluid.
This effect is not only a temperature induced effect, as a dilution of, for instance, 1 μl of this *yellow* stock solution in 3 ml of an aqueous buffer solution (5 mM HEPES, 2 mM CaCl2, 3 mMKCl, 147 mM NaCl, pH 7.4) appears *red-pink* at room temperature. This clearly demonstrates a strong environmental coupling of the dyes properties prior to any quantifying measurements. Quenching effects can be most likely neglected as they are not expected in these concentration ranges [53].

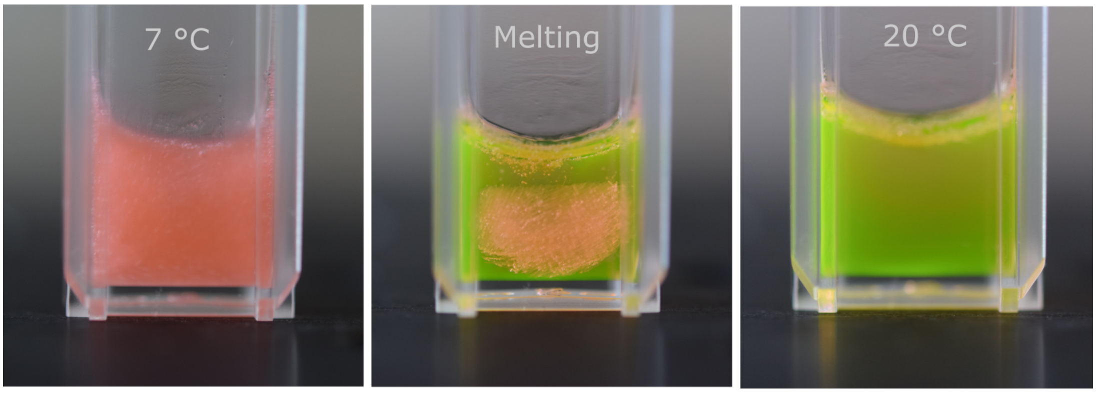

FIG. 3.5.: *Atto488 DPPE* in DMSO (0.5 μM). Left: Solution stored in the fridge at 7 °C is frozen and appears red-pink. Center: At room temperature the solution is melting due to the crossing of the melting temperature of DMSO (18.5 °C [54]). A coexistence of the frozen and liquid state is visible. Right: After acclimation to the room temperature (T = 20 °C) the solution is completely liquid and appears yellow.

FLUORESCENCE EMISSION SPECTRA

To investigate the fluorescence emission of the dye, spectrometer measurements were conducted. The emission spectra were recorded with a spectrometer (Thorlabs Compact Spectrometer [CCS100/ M]) plugged into an Olympus IX71 microscope via an optical fiber. The samples were excited with a mercury burner at $\lambda = 470\,\text{nm}$.

The fluorescence emission spectrum of 0.1 mol% *Atto488 DPPE* embedded in vesicles of DMPC lipids ($T_m = 24\,°\text{C}$ [55]) was monitored upon temperature variation. The results in **Fig. 3.6** demonstrate that there is indeed a variation in the position of the emission spectra. The main shift of the spectrum, characterized by the position of the wavelength with maximum intensity, coincides with the crossing of the melting temperature T_m of the lipids between 20 °C and 24 °C where it amounts to $\approx 1\,\frac{\text{nm}}{°\text{C}}$. This is significant compared to a rather linear, temperature dependent shift of the whole spectrum which amounts to $\approx 0.05\,\frac{\text{nm}}{°\text{C}}$. These data strongly suggest a correlation between emission spectrum and phase states of the lipids.

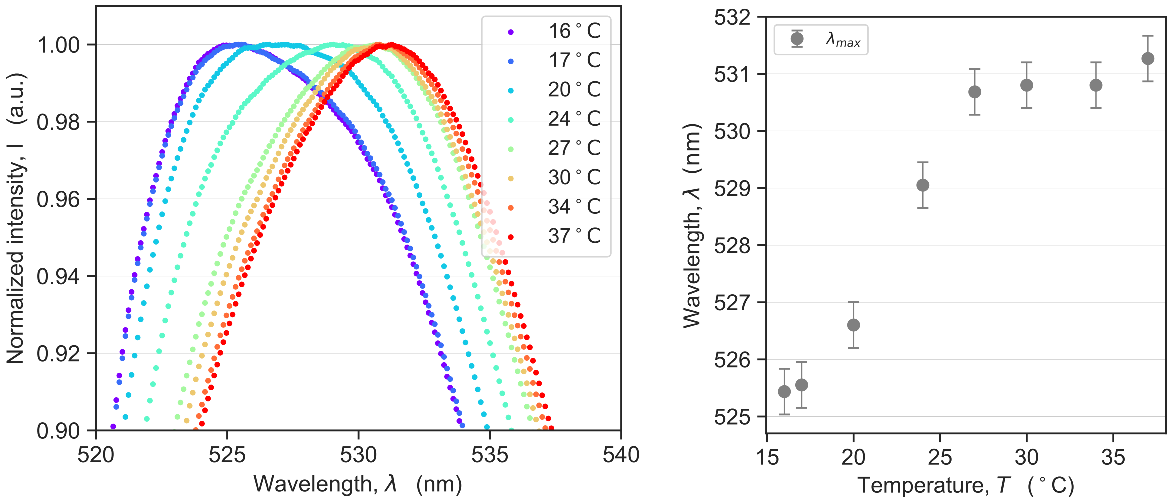

Fig. 3.6.: *Atto488 DPPE* in DMPC vesicles. Left: Normalized emission spectra upon temperature variation. Increasing temperatures from violet (outer left, 16 °C) to red (outer right, 37 °C). Right: Wavelength with maximal intensity extracted from the emission spectra against temperature. A nonlinearity due to an according blue shift in the emission spectra for decreasing temperatures is detected around 24 °C.

The absolute shift of the maximum is approximately 7 nm which is quite small compared to more established dyes as Laurdan or di-4-ANEPPDHQ where the shift amounts to up to 50 nm [56, 57]. However, within a sensitive setup for detection it is significantly resolvable.

The spectrometer used in these measurements has a resolution of 1 nm.
For temperatures further away from the transition the maximum of the spectrum remains at its position or shows at most a comparably small linear shift within the position ($\approx 0.05\,\frac{\mathrm{nm}}{^{\circ}\mathrm{C}}$) and indeed this is similar to the scenario described in **Fig. 3.3** where a simplified two state model is assumed.
For temperatures $> 27\,^{\circ}\mathrm{C}$ another change in the shape of the spectrum is apparent as especially the left flank *decreases* without an according shift of the wavelength at maximal intensity (refer to **Fig. 3.6**). This indicates that the spectrum is a superposition of two state dependent spectra with one vanishing at some point. It can be expected that not all vesicles are going through a transition simultaneously as there is a distribution of different vesicle sizes present which influences the transition parameters as well [55]. Consequently, a coexistence of both states over a limited temperature range is most likely.
The recorded spectrum at 20 °C is the widest of all recorded spectra and appears as a superposition where both apparent spectra are equally involved. Considering the spectrum as an energy distribution this observation is in compliance with the expected maximal fluctuations during a phase transitions. They would be mirrored in a wide energy distribution ergo a wide spectrum analogous to the fluctuations in other thermodynamic parameters as discussed in section 2.2.3. This strongly supports the hypothesis that the dye is thermodynamically involved in the lipid interface and enters into a coupling with the interface system.

The existence of an enlarged dipole moment upon excitation within the dye molecule is held responsible for the dye being sensitive to the polarity of a solvent or rather solvatochrome. It offers a higher level of interaction upon excitation with the (polar) solvent molecules. The dipole may originate in a shift of charge between distant chemical groups within the dye molecule as proposed in [51]. Analogous to the exemplary presented dye in [51], *Atto488* has spatially separated electron donor and acceptor groups (refer to **Fig. 3.4**) between which the electron can wander upon excitation of the dye molecule. Here, a potential electron donor is an amino group and a potential acceptor the carbonyl group. From this point of view it appears likely that the *Atto488* dye is sensitive to the solvent in general.

3.2. (OPTICAL) STATE DIAGRAMS OF LIPID INTERFACES

By choosing dyes as reporters for the physical state it is necessary to introduce optical parameters into the collection of thermodynamic observables. In the following, emission parameters of *Atto488 DPPE* are systematically investigated in various lipid systems. As all parameters are coupled within a thermodynamic system and the dye is getting part of the interface upon embedding into the membrane, it can be utilized as a probe. The emission of the dye is coupled to the systems state as it has been verified in the section before. Further, it can be concluded that the variation of the dyes emission properties are proportional to the changes in other thermodynamic observables. Thus, optical susceptibilities should be directly measurable as well as optical state diagrams. By this, a sufficient way is brought up to describe the thermodynamics representatively by optics.
Note, in principle, a thermodynamical coupling should hold for all molecules embedded into an biological interface as it has been demonstrated for enzymes as well. However, similar to a sensitivity of membranes/molecules to pH variations a sensitivity of a fluorescent dye to its environment is expected only under certain conditions. For each molecule a sensitivity towards protons is in principle given but whether it is observable depends on the applied shift in pH in combination with the pK of the molecule. In principle, the same holds for the dyes and its emission properties at given conditions.

3.2.1. OPTICAL SUSCEPTIBILITY

In order to record state diagrams optically a suitable parameter is needed displaying a phenomenological coupling to the physical states of the system. Upon coupling the position of the energy levels, and respectively the emitted energy of the dye, are sensitive to the surrounding system e.g. dipoles of the solvent (solvatochromism). Here, the solvent means the lipid interface and the dye becomes a part of its thermodynamic entity and will mirror its state. It can be used as a state reporter. As the spectrum measurements in section 3.1.3 demonstrate *Atto488 DPPE* is indeed sensitive to the state of the lipid membrane. The parameter of interest will be the ratio of the intensities at two wavelengths of the emission spectrum, namely $r = I(520\,\mathrm{nm})/I(530\,\mathrm{nm})$. It is chosen in such way that λ_{max} is between these two wavelengths and a change in spectrum will be reflected in r.

A variation in the spectrums position represents a shift in the emission energy of the dye E_{em} which is a direct result of the change in the dipole ordering within the membrane and further the lipid order. In general the phenomenological relation

$$\mathrm{d}E_{em} \propto \mathrm{d}\lambda_{max} \propto \mathrm{d}r \propto \mathrm{d}H \tag{3.1}$$

will hold true. Even a displacement in the flanks of the spectrum towards one side (without a corresponding shift in λ_{max}), which already means a relocation of the energy, will be recognized in r. Importantly, by that, a measure proportional to the enthalpy H of the system is provided. Hence, its derivative according to temperature T ($\frac{\partial r}{\partial T}$) is analogous to the heat capacity $c_p = \frac{\partial H}{\partial T}$ in calorimetric measurements and has the nature of a thermodynamic susceptibility ($\frac{\partial H}{\partial T} \propto \frac{\partial r}{\partial T}$).

This can be derived as well from the correlated fluctuations of the system: Assuming the (thermodynamic) state variable character of the ratio parameter as given, the correlated fluctuations of r and enthalpy H can be calculated and yield:

$$\left\langle (\delta r \delta H) \right\rangle = \mathrm{k} \left(\frac{\partial S^2}{\partial H \partial r} \right)^{-1} = \mathrm{k}T^2 \left(\frac{\partial r}{\partial T} \right)_{\pi} \tag{3.2}$$

A (phenomenological) parameter $\left(\frac{\partial r}{\partial T}\right)_{\pi}$ can be derived proportional to a susceptibility which correlates according to equation 2.17 with other susceptibilities such as the isobaric heat capacity c_π or isothermal compressibility κ_T. Analogously a relation between fluctuations in r, δr, and area δA can be derived:

$$\left\langle (\delta r \delta A) \right\rangle = \mathrm{k} \left(\frac{\partial S^2}{\partial A \partial r} \right)^{-1} = \mathrm{k}T \left(\frac{\partial r}{\partial \pi} \right)_{T} \tag{3.3}$$

Hence, a mechanical coupling of r can be established as well, which comes into play for isotherms where the isothermal compressibility κ_T is the susceptibility at hand. With that, the ratio r is most likely a well suited parameter for the recording of optical state diagrams.

3.2.2. CONFOCAL SETUP

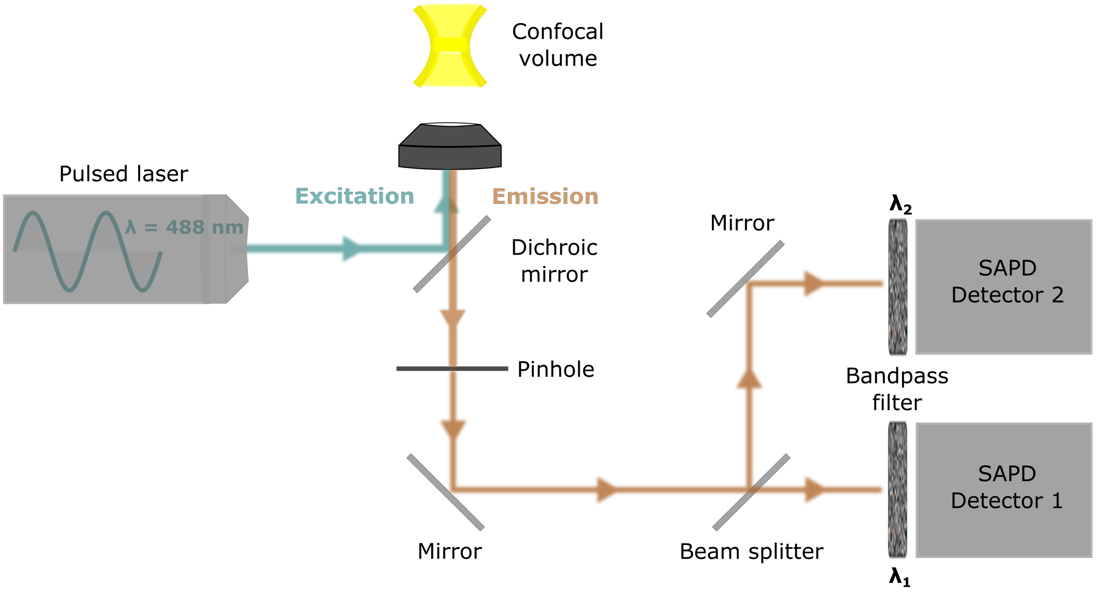

FIG. 3.7.: Scheme of the underlying detection setup for all consecutive measurements: The basic parts are the pulsed laser excitation, a fluorescence microscope and a detection unit with a pinhole for determining the confocal volume and two single photon detectors.

The general, basic setup for the measurements throughout this study is a confocal microscope system (Microtime 200 device; PicoQuant) which is schematically depicted in **Fig. 3.7**. Samples are excited by an integrated laser line at 488 nm which is operated in pulsed mode (mostly 20 MHz). The laser pulses are coupled into a single mode optical fiber and guided to the sample via an objective of the fluorescence microscope (Olympus IX73). The objective is a 60X water immersion objective (UPLSAPO60XW; Olympus) with NA =1.2. The microscope is extended by an optical detection unit containing the pinhole (50 μm) and two single-photon avalanche diodes (PCM-AQRH-14-TR; Excelitas) where the emission signal is detected. The emission signal is separated by a beam splitter either according to a 50/50 ratio or according to polarization directions. If not otherwise stated the 50/50 beam splitter is used. Bandpass filters in front of each detector allow the extraction of certain wavelength bands from the emission signal.
This setup is highly sensitive as it allows the detection of single photons. Due to the integrated pinhole the emission signal can be allocated within a cutout of the focus volume given from the objective, the confocal volume. By that, the spatial resolution is increased and with the combination of the given pinhole and objective the confocal volume has a radial diameter of $\sim$ 300 nm in xy direction and $\sim$ 800 nm in z direction.
An additional piezo below the objective functions as a scanning unit and is able to raster a 80 μm x 80 μm x 80 μm range in xyz direction for imaging.

MEASURING TECHNIQUES

The **T**ime **C**orrelated **S**ingle **P**hoton **C**ounting (TCSPC) mode works with a pulsed laser excitation. It requires relatively low dye concentrations such that a maximum of **one** photon is detected between two excitation pulses. This is due to the detection mode of the avalanche diodes as they recognize whether there was a photon or not with a high temporal accuracy but not whether the signal was triggered by more than one photon. Thus, one pulse should excite less than one fluorophore on average. Then, the time τ between the excitation pulse (*start*) and the detection of the **first** responding photon (*stop*) is measured by the system as the TCSPC unit (Hydra harp 400; PicoQuant) connects the laser driver with the detector output (**Fig. 3.8**). By that, τ is a measure for the time the molecule stays in its excited state, the fluorescence lifetime. Each start-stop time τ is filed into a histogram with a bin width of 16 ps which meets the temporal accuracy of the setup. The timing uncertainty mainly derives from the conversion of the photon into an electrical signal within the detector.

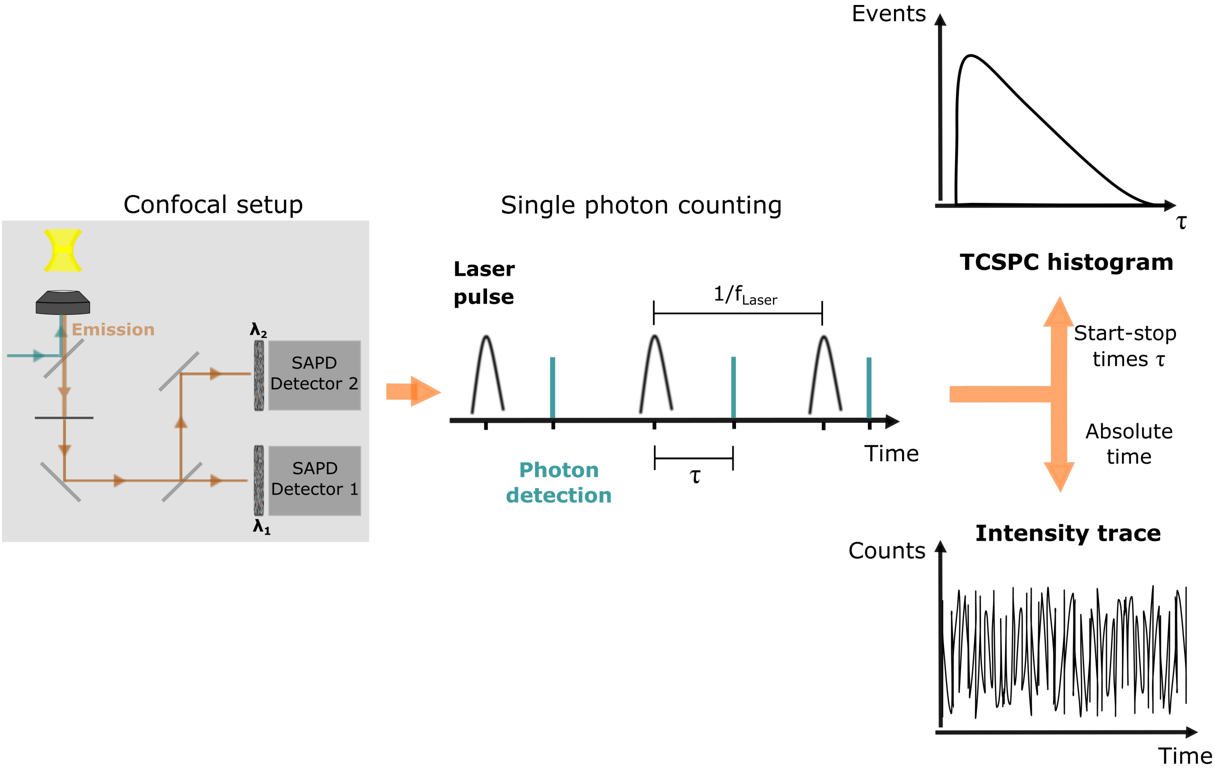

FIG. 3.8.: **T**ime **C**orrelated **S**ingle **P**hoton **C**ounting: The interval between two pulses is $1/f_{\text{Laser}}$ where f_{Laser} is the pulse frequency of the laser. The start-stop times τ are sorted within a histogram from which the fluorescence lifetime can be extracted. The start-stop times sorted on an absolute timeline deliver an intensity trace.

The dye concentration has to be chosen carefully as more than one photon per pulse interval (50 ns for $f = 20\,\mathrm{MHz}$) is not detectable as to the operation mode of the detectors. Their response is triggered by one photon and they are not sensitive for more than one photon within the dead time. The dead time is composed of the dead time of the detector (22 ns [58]) and the dead time of the TCSPC timer module (80 ns [59]). Further, it is recommended to use a dye concentration such that approximately one in ten pulses is responded by an emitted photon. Otherwise systematic errors in the photon counting such as a pile up effect would most likely occur. By that, early arriving photons would be over represented in the histogram as the detectors are not sensitive for later arriving photons.

The time between two pulses is typically 50 ns as the laser pulse frequency is set to $f = 20\,\mathrm{MHz}$.

The resulting histogram mirrors a distribution of lifetimes and can be described analogously to a decay process via an exponential relation. Additionally, an intensity time trace is generated by arranging the detection times of the single photons on an absolute timeline, which in turn is used for calculation of correlation functions or ratiometric parameters (**Fig. 3.8**). It becomes clear that the intensity trace has a limited temporal resolution of $1/f_{\mathrm{Laser}}$ where f_{Laser} is the pulse frequency of the laser.

RATRIOMETRIC PARAMETER

The ratiometric parameter is yielded by:

$$r = \frac{I(\lambda_1)}{I(\lambda_2)} \tag{3.4}$$

The intensities can be either extracted from the integral over the TCSPC histograms for each wavelength or directly from the intensity traces. For most measurements on *Atto488 DPPE* bandpass filters with a width of 10 nm each at the following wavelengths

$$\begin{aligned} \lambda_1 &= 520\,\mathrm{nm} \quad (10\,\mathrm{nm}) \\ \lambda_2 &= 530\,\mathrm{nm} \quad (10\,\mathrm{nm}) \end{aligned}$$

are used. By that, a shift of $\sim$ 10 nm in the emission spectrum is sufficiently resolved.

FLUORESCENCE LIFETIME

An exemplary recorded TCSPC histogram is shown in **Fig. 3.9**. The number of events is scaled logarithmically on the y-axis and is plotted against the start-stop times on the x-axis. From this histogram the fluorescence lifetime is extracted which is an optical parameter of interest as it represents the relaxation process of the dye molecule.

The lifetime is a quantity independent from the concentration of the fluorophore which makes it robust for intensity variations throughout measurements. The only restriction in dye concentration exists due to the given setup and its single photon readout limitations as discussed in the previous subsection.

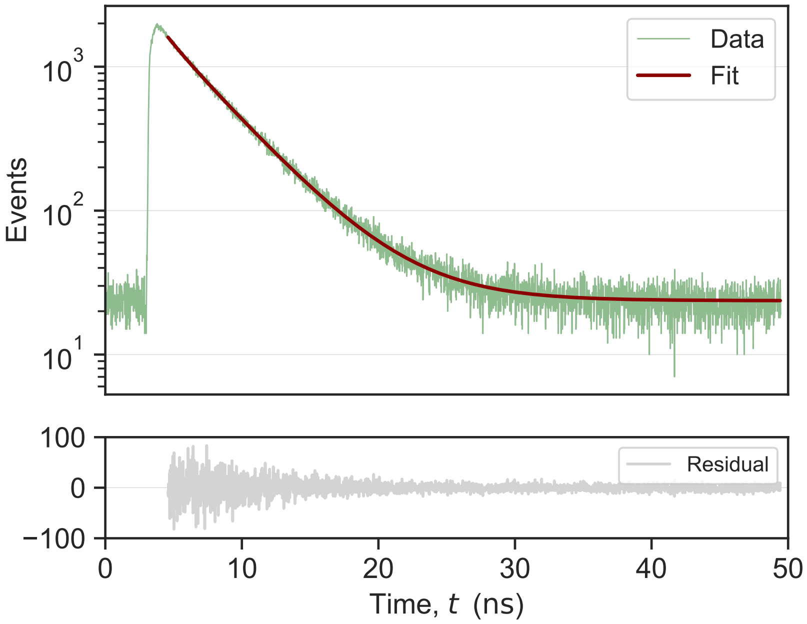

FIG. 3.9.: Time **C**orrelated **S**ingle **P**hoton **C**ounting histogram: Overview of the detected start-stop times of single (emitted) photons. The maximum in time is defined by the time between two excitation pulses ($t_{\max} = 50\,\mathrm{ns}$ for $f = 20\,\mathrm{MHz}$). Within this interval the excitation happens at $\approx 3\,\mathrm{ns}$. An exponential decay describes the course of the histogram and the fluorescence lifetime can be associated with the time constant of the decay. Bottom: Residuals of the fit describing the deviation of the fit from the measured data (Residuals = Data - Fit).

The pulse interval (set by the excitation frequency) is chosen in that way that the decay of the curve is mostly saturated into the background within the given interval. By that, an incorrect allocation of the start-stop time shall be avoided. Times longer than $t_{\max}$ (here: 50 ns) would be detected in the next pulse interval and mistakenly associated with the latter pulse. Thereby, longer lifetimes would be detected falsely as *short* lifetimes in the next interval. Which pulse interval is necessary cannot be concluded in general but is dependent on the lifetime of the dye.

The fluorescence lifetime, the relaxation time of the molecule, describes a statistical process similar to a nuclear decay. The decrease in time is linear on the logarithmic scale as it underlies an exponential decay. It appears, that in most cases two lifetimes are needed to describe the measured histograms sufficiently. The second, shorter, lifetime most likely exists due to technical reasons (instrument response function, thermal noise..) as it is very fast (~ 1 ns) and rather not related to the dye itself. The fluorescence lifetime of *Atto488* is around 4 ns. In general, since lifetimes are sensitive to environmental influences different *state-associated* lifetimes would be conceivable as well. In fact, there are dyes exhibiting more than one fluorescence lifetime and a multiexponential decay model could be applied [51].

Throughout this study it has proven itself to apply a two-exponential decay as follows

$$y(t) = A_1 \exp(\frac{t - t_0}{\tau_1}) + A_2 \exp(\frac{t - t_0}{\tau_2}) + B \tag{3.5}$$

where τ_1 and τ_2 are two fluorescence lifetimes The background noise level is expressed by B. The time at which the fit starts is t_0 and resembles the point of time with the maximum of the curve. Based on that model a fit is placed through the curve as visible in **Fig. 3.9**.

However, for the analysis of the fluorescence lifetimes the focus lies not on absolute values but rather on the identification of relative changes for varying conditions. Since the signal is (phenomenologically) treated as a superposition of two lifetime species, a shift might be missed as there are four coupled fit parameters that are influenced by each other. Therefore, a parameter is derived representing the whole histogram and which is comparable throughout a measurement series. Mathematically, weighted lifetimes are suited parameters. Lifetimes can be either weighted according to their amplitudes A_1 and A_2 mathematically referring to the distribution of the lifetimes at the time $t = t_0$ (denoted with τ_{av}), or by their intensities (I_1,I_2). For the intensity weighted lifetime $\tau_{I_{av}}$ the intensities (I_1,I_2) are derived by the integration over all photon counts associated with each lifetime:

$$\tau_{av} = \frac{A_1}{A_1 + A_2}\tau_1 + \frac{A_2}{A_1 + A_2}\tau_2 \tag{3.6}$$

$$\tau_{I_{av}} = \frac{I_1}{I_1 + I_2}\tau_1 + \frac{I_2}{I_1 + I_2}\tau_2 \tag{3.7}$$

The intensity weighted lifetimes $\tau_{I_{av}}$ is the more representative value as it accounts for the share to which the lifetimes appear. By that, an overestimation of a lifetime with minor relevance is avoided.

The intensities (I_1, I_2) associated to each lifetime species (τ_1, τ_2) are derived from the integration of the fit function:

$$\begin{aligned} I^*_{\text{sum}} &= \int_{t_0}^{t_{\max}} \left(A_1 \mathrm{e}^{-\frac{(t-t_0)}{\tau_1}} + A_2 \mathrm{e}^{-\frac{(t-t_0)}{\tau_2}} + B \right) \mathrm{d}t & (3.8) \\ &= A_1\tau_1 \left(1 - \mathrm{e}^{\frac{t_0 - t_{\max}}{\tau_1}}\right) + A_2\tau_2 \left(1 - \mathrm{e}^{\frac{t_0 - t_{\max}}{\tau_2}}\right) + (t_{\max} - t_0)B & (3.9) \\ &\mathrel{\widehat{=}} \qquad I^*_1 \qquad + \qquad I^*_2 \qquad + \quad I^*_B & (3.10) \end{aligned}$$

The integral is limited by t_0 which is related to the maximum of the histogram and $t_{\max}$ referring to the interval between two laser pulses (here: $t_{\max} = 50\,\text{ns}$).

It is important to note, that the amplitudes (A_1, A_2) have similar units as entries of the histogram which correctly amount to counts/binsize. Thus, a factor 1/binsize (1/16 ps) must be multiplied either with the fitted amplitudes (A_1, A_2) or respectively with the yielded intensity values (I^*_1, I^*_2) to verify the integration over time ($I = \frac{I^*}{\Delta t}$ with $\Delta t = 16\,\text{ps}$). For the error analysis of these parameters refer to A.5.1 in the Appendix.

An alternative, phenomenological way for comparing the TCSPC histograms can be approached by comparing the width at the histograms. It gets by without a fit of the curves and has itself proven to come to similar results as the lifetime analysis regarding the comparison of curves. It is not useful when absolute values are needed. For that, the histograms are normalized and a width is calculated at a given level (e.g. 0.3). For an example refer to A.5.3 in the Appendix.

To verify that the lifetime is indeed a concentration independent parameter and to characterize potential intensity effects not related to the lifetime a power series can be conducted. By that, the excitation strength of the laser is successively increased and the TCSPC curves compared. The lifetimes should not be affected by the increase in excitation strength. For more detailed explanations and an example refer to A.5.2 in the Appendix.

3.2.3. LIPID VESICLES: RESULTS AND DISCUSSION

The most simplified model system of a cell is a lipid vesicle in aqueous solution. Pure lipid vesicles are already thoroughly characterized regarding their melting temperatures and are an appropriate system for starting a systematic thermodynamic characterization by the optical parameters.

MEASUREMENT DETAILS

For the measurement on vesicle suspensions a closable chamber (FCS2; Bioptechs) is introduced into the setup (refer to A.4 in the Appendix). It is closable by a coverslip and contains the sample. The coverslip as part of the chamber is coupled to the immersion objective. The chamber is connected to a heating bath (Lauda Eco Silver). Outer pipes ensure a flow around the sample with heating bath fluids and allow temperature control of the sample. Temperature is measurable with a thermometer (TMD-56; Amprobe) coupled to the chamber with an accuracy of 0.1°C. However, absolute temperature values will be most likely affected by the coupling of the chamber to the nonheated immersion objective. The extent depends on the deviation between sample temperature and room temperature. For experiments above room temperature the measured temperature is expected to be an overestimation of the *real* temperature as the coupling cools the sample.
All vesicle suspensions are prepared with 0.1 mol% of *Atto488 DPPE*. For a description of the production of vesicle suspensions refer to section A.2 in the Appendix.

STATE DIAGRAMS

In the following, the state of vesicle suspensions of different lipid types is monitored under temperature variation. The emission spectrum is reduced to the ratiometric parameter $r = \frac{I_{520\text{nm}}}{I_{530\text{nm}}}$ which is monitored as a potential state variable. As temperature is the most obvious thermodynamic parameter for accessing and controlling the vesicle suspensions a state change is induced by heating/cooling across the melting temperature of the lipids at hand.

In **Fig. 3.10** the ratio parameter of *Atto488 DPPE* embedded into DMPC vesicles is monitored under temperature variation. A significant nonlinearity is detected in the optical response between 25 and 28 °C yielding a sigmoidal course. The change in r amounts to $\approx \frac{0.025}{°\text{C}}$ within this nonlinear regime compared to $\approx \frac{0.001}{°\text{C}}$ outside of that temperature range. An increase in the ratio parameter at lower temperatures indicates a blue shift in the emission spectrum. This behavior resembles the spectral shift in the dyes emission that has been already identified within spectrometer measurements and underlines the existence of the two-state system.

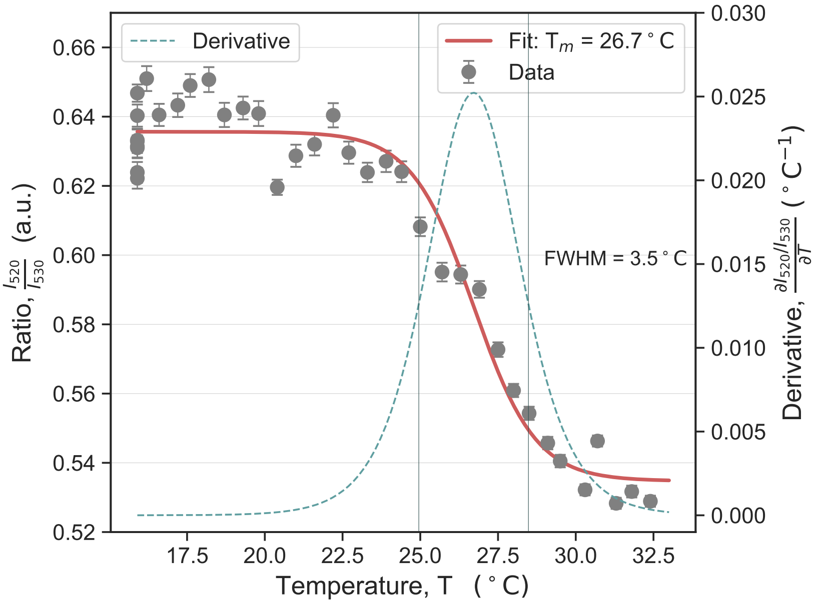

FIG. 3.10.: Exemplary optical state diagram of DMPC lipids: Ratio parameter (grey dots) measured under temperature variation. The nonlinear shift in the ratio parameter around 26 °C resembles an associated spectral shift in the emission spectrum of the dye.

The main transition temperature T_m is at 24 °C for DMPC [55]. This aligns quite well with the temperature associated with the greatest change in r, which is visualized by the derivative of r with respect to T in **Fig. 3.10**. The derivative has been already introduced in section 3.2.1 as a measure for the susceptibility. The concept has successfully proven itself here and a maximum in this observable can be identified as a phase transition.
Note, as already mentioned in the section before, the measured temperature contains an overestimation for temperatures above the room temperature which amounts for the small deviation between theoretical and measured T_m.

The measurement in **Fig. 3.10** is an exemplary curve as it was repeated several times with a similar outcome. All measurements present the nonlinearity around 26 °C. A generalized illustration over all measurements is not reasonable as absolute ratio values may differ between different series and a mean series would not provide more information.
Each curve is considered individually for an analysis. The sigmoidal shape is fitted with a logistic function from which the midpoint of the sigmoid is extractable. It is associated with the melting temperature of the lipid T_m as it describes the point with the strongest shift in r. With that $T_m = (26.7 \pm 0.3)$ °C is derived for the presented measurement.
The transition is characterized by the melting temperature T_m and its width. The width is represented by the full width of the half maximum (FWHM) of the optical susceptibility (derivative) and yields (3.3 ± 0.3) °C. In conclusion, the phase transition can be fully characterized by the ratiometric parameter and it is indeed a state variable.

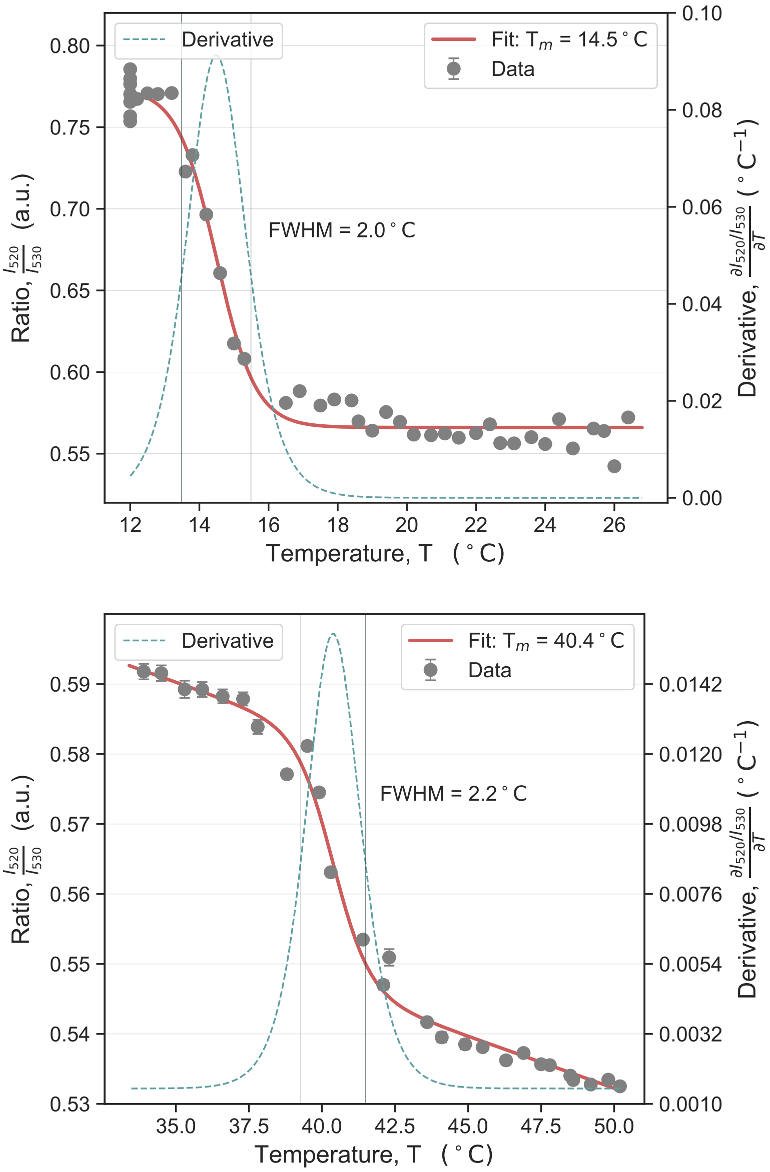

FIG. 3.11.: Optical, nonlinear, response of *Atto488 DPPE* embedded in DLPS vesicles (top) and DMPS vesicles (bottom) upon temperature variation. The maxima of the optical susceptibilities correlate quite well with the expected transition temperatures for DLPS (T_m = 14 °C [60]) and DMPS (T_m = 38 °C [61]).

Further lipid types were investigated in a similar manner to verify that the shift in the emission spectrum is coupled to the lipid state and to exclude that the results on DMPC are a coincidence. In **Fig. 3.11** the derived diagrams for DLPS and DMPS are shown. The main difference compared to DMPC is the headgroup (-PS) which is negatively charged at a physiological pH and has a pK at ≈ 5.5. While the lipid anchor of the dye, DPPE,

is zwitterionic, similar to DMPC, a mixture with charged (-PS) lipids could enforce a separation of both lipid types. However, the used dye concentrations are small ($\sim 0.1\,\%$) and a separation is very unlikely.
Vesicle suspensions of DLPS as well as DMPS (or rather the embedded dye within these systems) report again a nonlinear behavior that aligns with the expected melting temperatures of the lipids. For the DLPS vesicle suspension (in **Fig. 3.11** on the left) the melting temperature could be identified at $T_m = (14.5 \pm 0.4)\,°\mathrm{C}$ and for DMPS (in **Fig. 3.11** on the right) at $T_m = (40.4 \pm 0.3)\,°\mathrm{C}$.
In general, a correlation between absolute emission intensity I and ratio values r has been observed. This comes merely into effect when there are significant intensity variations present throughout a measurement series. As this effect can potentially dominate the rather small shift in the ratio parameter, which is related to the state change, a correction of the ratio parameter values is performed in that cases. In order to quantify the correlation between r and I a reference measurement prior to the measurement series is conducted. For more details refer to section A.6 in the Appendix.

Additionally, all presented curves contain a more or less pronounced linear incline in the ratio parameter upon temperature variation $\approx 0.001/°\mathrm{C}$. Indeed, this was already visible by a shift in the flanks of the spectrum in the spectrometer measurements in section 3.1.3. This general phenomenon has already been reported in the literature and can be associated with the temperature dependent solvent motion [51]. Nonetheless, these linear dependencies are not significant compared to the nonlinearity residing in these curves at the transition ($0.02/°\mathrm{C}$ - $0.1/°\mathrm{C}$).
In summary, it is apparent that *Atto488 DPPE* undergoes a thermodynamic coupling to its environment and mirrors reliably the phase state regardless of the lipid type.

INFLUENCE OF PH

To examine the usability of the dye under physiological conditions a potential sensitivity towards pH must be clarified. For that, *Atto488 DPPE* is again embedded into DMPC vesicles and measured (under temperature variation) in suspensions at pH 7.4 and pH 5.5 respectively.

The melting temperature is affected by pH changes when the membrane is close to its pK which has been discussed in section 2.2.4 before. As DMPC has its pK around pH 2 the melting temperature should remain unchanged and no effect on the optical response of the dye in its role as phase state sensor is expected, unless it is sensitive to pH in general. The comparison of both state diagrams in **Fig. 3.12** reveals that there is no significant difference between them. This is confirmed by the melting temperatures $T_m(\text{pH } 5.5) = (26.1 \pm 0.2)\,°\text{C}$ and $T_m(\text{pH } 7.4) = (26.7 \pm 0.3)\,°\text{C}$. The profiles of the optical susceptibilities (**Fig. 3.12** on the right) are quite similar as well. Width and amplitude are not significantly affected by the pH change. For that matter, a (general) pH sensitivity of the dye can be excluded.

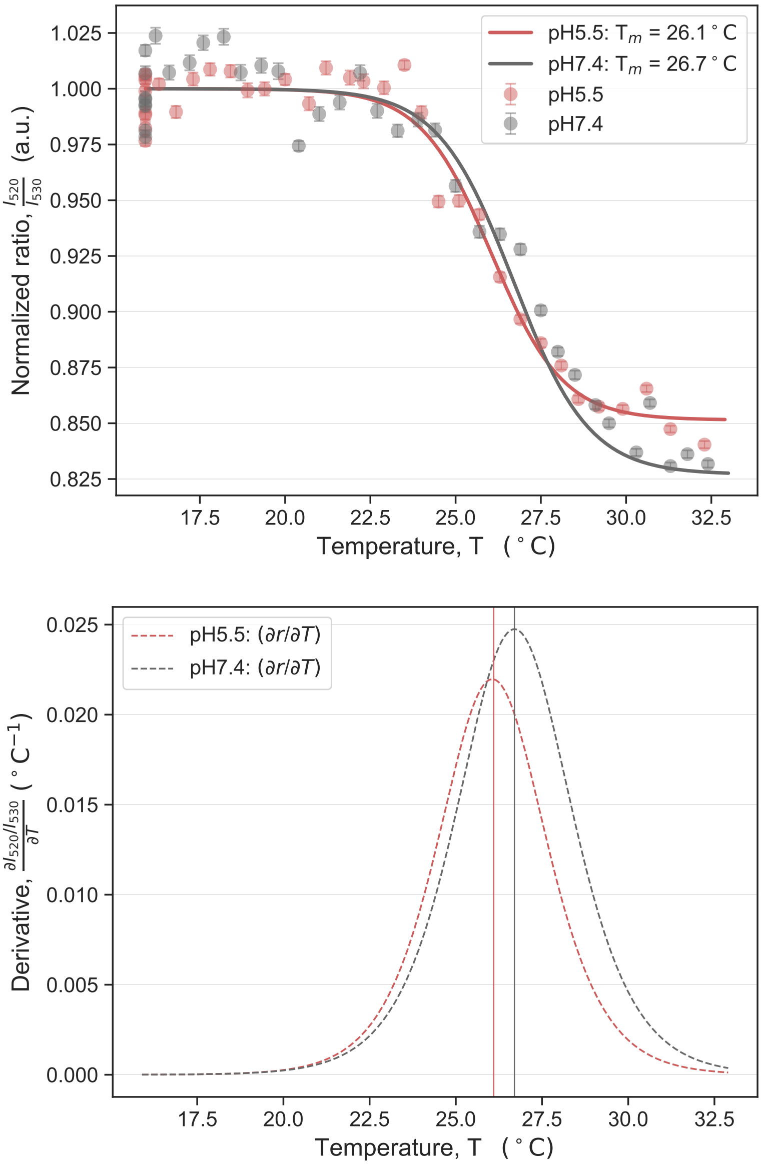

Fig. 3.12.: Comparison of the state diagrams for DMPC vesicle suspensions at pH 5.5 (red) and pH 7.4 (grey). Left: Normalized ratios upon temperature variation. Right: Profiles of the respective optical susceptibilities. The maxima points correlate with the transition temperatures. Both series were recorded upon heating.

A similar comparison for *Atto488 DPPE* in DLPS vesicles (p$K \approx 5.5$) at pH 5 and pH 7 reveals significant differences in the optical state diagrams (refer to **Fig. 3.13**). The melting temperature is increased by ~ 5.5 °C for the pH 5 suspension compared to pH 7.

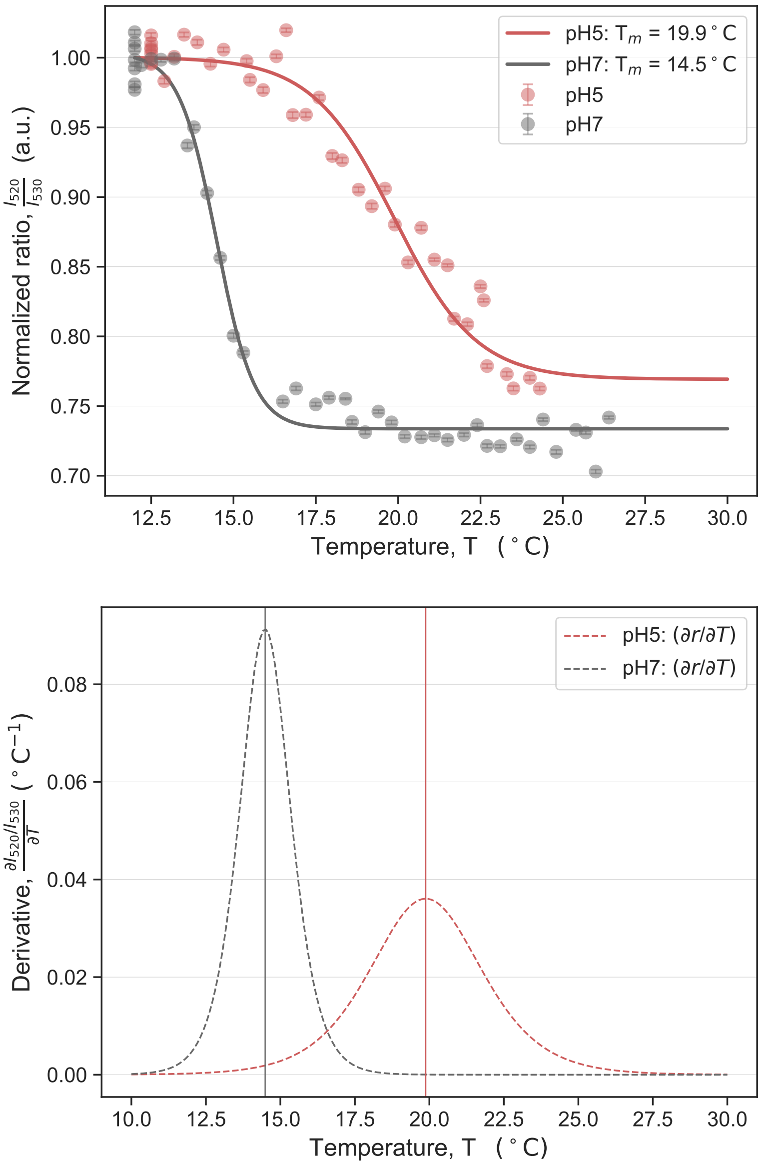

Fig. 3.13.: Comparison of the state diagrams for DLPS vesicle suspensions at pH 5 (red) and pH 7 (grey). Left: Normalized ratios upon temperature variation. Right: Derivatives of the optical signal. The maxima of these susceptibilities point at the temperatures of the transition. Both series were recorded upon heating.

This confirms the qualitative prediction from equation 2.20 in section 2.2.4 for the correlation between pH and T_m as the pK of the -PS headgroup is at $\sim$ 5. In contrast to DMPC a sensitivity of the melting temperature is expected and adequately reflected in the optical measurements. A final quantitative evaluation of the shift remains difficult since the dependency is not linear but rather most pronounced around the pK.
The profiles of the optical susceptibilites differ as well. The amplitude is significantly reduced at pH 5 compared to pH 7.

LIFETIMES

Another optical parameter of interest is the fluorescence lifetime. It describes the relaxation process within the molecule and is calculated with the beforehand presented intensity weighted lifetime $\tau_{I_{av}}$ (refer to equation 3.6). For the DMPS vesicle suspension an increased lifetime could be detected in the fluid disordered phase compared to the ordered phase within the λ = 530 nm signal. For λ = 520 nm the effect is not as pronounced (**Fig. 3.14**). The change in $\tau_{I_{av}}$ is correlated to the shift in the ratio which has been identified with a phase transition. It is illustrated by the maximum in the derivative of the ratio signal in **Fig. 3.14**.

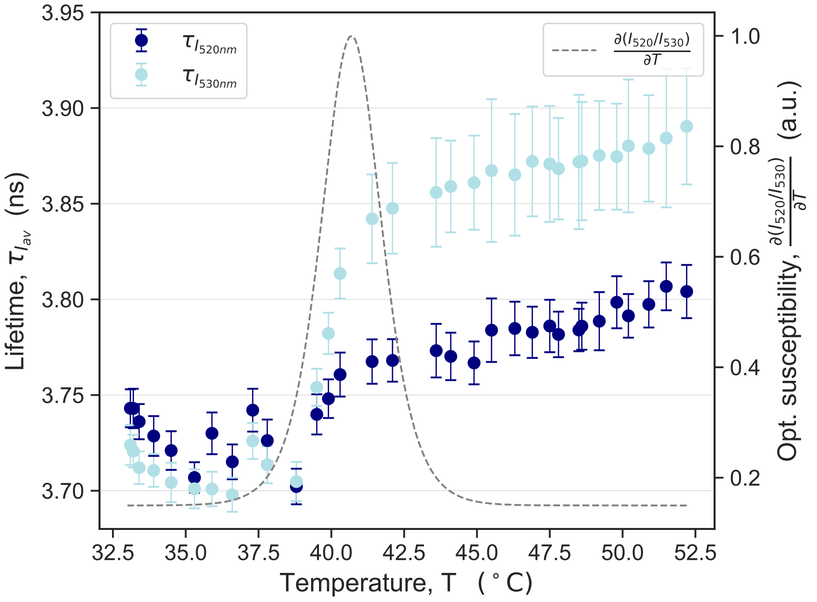

FIG. 3.14.: Optical parameters extracted from a measurement on a DMPS vesicle suspension. The intensity weighted lifetime $\tau_{I_{av}}$ calculated from the TCSPC histograms for both monitored wavelengths. A nonlinear behavior is detected correlating with the phase dependent ratio shift which is presented by its derivative, the optical susceptibility.

For DLPS a dependency could be detected as well but in a reversed manner. There, the lifetime is lower in the disordered phase than in the ordered phase. This effect is most pronounced in the $\lambda = 520\,\mathrm{nm}$ channel where the shift amounts to $\sim 0.2\,\mathrm{ns}$ (data not shown). In contrast, in DMPC vesicles, no conclusive results could be derived as there were no significant and consistent shifts present during the measurements. Note, measuring the width of the normalized TCSPC histograms delivers similar results and an artefact from the analysis can be excluded.

In summary, the use of the lifetime as a state parameter is limited to certain systems. Both presented charged lipid types (-PS) reflect a nonlinearity in the dyes lifetime whereas the zwitterionic lipid (-PC) does not. Whether the origin of this distinguished behavior lies in the dipole moments cannot be clarified beyond doubt.

3.2.4. LIPID MONOLAYER: RESULTS AND DISCUSSION

Lipid monolayers are a quite unique system in terms of direct accessibility of the phase state. They are easily preparable on a water surface due to the amphiphilic structure of phospholipids. Within a Langmuir trough setup the lateral pressure π of the monolayer is monitored as a function of its area A. By that, an isotherm is derived and presents a state function of the monolayer. The constant compression of the area A reveals a nonlinearity in the lateral pressure π, where a comparably large compression of A is induced without an aligned, significant increase in π, the so-called plateau region of the isotherm. It is a consequence of the rearrangement of the lipid molecule alignment within the layer into a higher ordered state. The area associated thermodynamical susceptibility, the isothermal compressibility $\kappa_T \sim \frac{\partial A}{\partial \pi}$ is a measure for the softness of the system. It is maximal during the plateau region accordingly to the principle of maximization of fluctuations.

By that, a state diagram of the lipid monolayer is directly accessible and upon introduction of dyes into the system it is well suited for a mechano-optical coupled approach to the physical states of the monolayer [62]. Optical and mechanical measurements can be performed simultaneously on the lipid interface. Moreover the state of the monolayer is controllable and can be set accurately to a defined state when the isotherm is known. This is in contrast to temperature guided experiments where the transition of the lipid system is assumed upon the accessible transition temperature. This might be a potential error source depending on the setup and especially the location of the temperature measurement (sensor).

A lipid monolayer is a versatile system for investigating different aspects of the artificial membrane. It provides not only a basis for monitoring quasi-statically (state diagrams) but has been used to investigate the nature of propagating perturbations, acoustic pulses, phase dependently as well [42]. Within the confocal system the monitoring of the monolayer can be taken to a new level. It is possible to observe two-dimensional dynamics on a molecular level, e.g. lipid movement. Whereas in vesicle suspensions the movement of the vesicle as a whole is monitored. Hence, it is a promising system to establish within the given confocal setup and its optical response will be characterized in quasi-static experiments. Dynamics of the system are presented later in section 3.3.2.

SETUP

The general setup for monolayer measurements is illustrated in **Fig. 3.15**. Basic element is the Langmuir trough, a teflon trough, containing a subphase which is ultrapure water or a buffered saline. On the surface of the subphase the layer is prepared upon spreading lipids solved in chloroform. The chloroform evaporates and the lipids gather on the surface. The area of the layer is controlled via teflon barriers and its two-dimensional (lateral) pressure

π is monitored with a pressure sensor. The sensor itself is coupled to a Wilhelmy plate, a piece of filter paper touching the surface of the layer and measuring the force caused by the surface tension acting on that plate. By that, the decrease of the surface tension of the subphase with additional surfactant π_L compared to the surface of the subphase without surfactant π_W is detected corresponding to the lateral pressure π:

$$\pi = \pi_W - \pi_L \tag{3.11}$$

The formation of a lipid monolayer reduces the surface tension as the surface water molecules interact with the lipid molecules instead of the gas molecules of the air. A compression of the layer leads to a further reduction of the surface tension and the lateral pressure is increasing upon compression once a monolayer has formed.

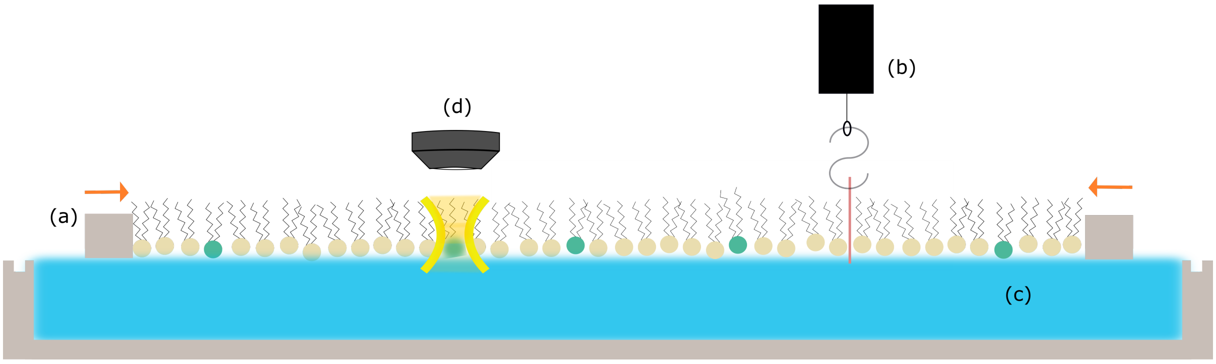

Fig. 3.15.: Langmuir trough setup: A teflon trough filled with a subphase (c) is the basis on which surface a lipid monolayer is spread. Teflon barriers (a) can compress the area of the monolayer and by that, induce phase transitions within the layer. The lateral pressure of the layer is monitored upon a pressure sensor via a Wilhelmy plate (b). Simultaneously, embedded dye molecules in the monolayer (blue-green heads) are excited and deliver an optical response via the optical detection (d).

To integrate a Langmuir trough into the confocal system an objective inverter (InverterScope; LSM Tech) is introduced. It inverts the objective by 180° and elongates the signal pathway by a fibre within an arm to the point were the objective is mounted. By that, it is possible to place the trough next to the microscope and measure directly at the surface of the trough where the lipid interface is located.

For optical detection typically 0.05 mol% of dye molecules are incorporated into the layer. Due to the geometrical conditions of the inverted objective and its use at the surface of the subphase the immersion objective is replaced by a 40X air objective (40X, NA = 0.65, WD = 0.6 mm, PLCN40X, Olympus). During the monitoring of the π-A diagram the optical signal is tracked simultaneously. The intensities are recorded over t whereas the pressure is recorded over A which is proportional to the time elapsed t.

An exemplary output of the raw data from a DPPC monolayer is shown in **Fig. 3.16** where the area is compressed with increasing t. Note, these measurements reflect a compromise between slow compression velocities to ideally ensure a *quasi-static* recording of a phase state diagram and on the other hand fast compression velocities as the surface level lowers over time due to evaporation of the subphase. Usually, an isotherm would be recorded slower than the here presented results since the monolayer needs time to adapt to the *new* state induced during the steady area compression.

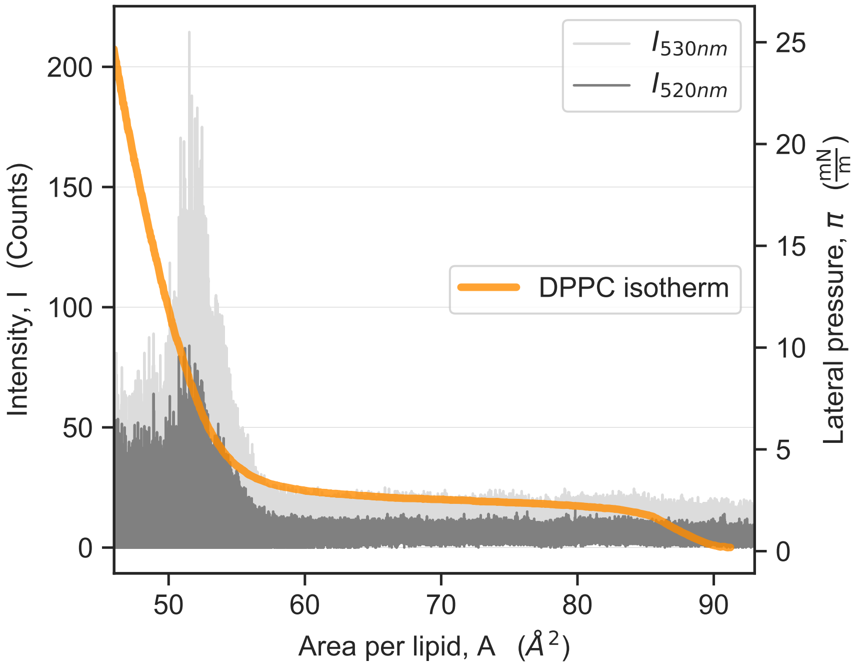

Fig. 3.16.: Raw data recorded during an isotherm of a DPPC monolayer with 0.05 mol% *Atto488 DPPE*. Mechanical compression of the area delivers a state diagram in π (orange). The intensities of both wavelengths of the emission signal are shown as well (light and dark grey). The compression was conducted with a constant velocity of the barrier t which is proportional to the compression of A.

A classic isotherm including a pronounced plateau region is yielded in the pressure signal. The plateau appears once further compression of the area does not lead to a corresponding increase in π. Instead, the performed work is consumed for rearrangement of the lipid order within the layer into the liquid condensed phase state. After the transition π increases again proportional with the compression of A. The existence of one pronounced plateau shows that the cooperativity of the transition is preserved and that the dye-lipid complex does not interfere with the systems thermodynamics. On the contrary, it forms a new thermodynamic entity as expected. Otherwise, a phase separation mirrored in two plateaus would be apparent. The intensity traces of the emission wavelengths are unchanged until the end of the plateau region where a maximum in both channels is apparent. The increase happens nonlinear with the compression and is not a consequence of increased dye concentration in the focus. For further increased pressures the intensity decreases again.

OPTO-MECHANICAL COUPLING

The analysis of the mechanical and the optical response of the DPPC monolayer during compression is shown in **Fig. 3.17**. As the area A or more precisely the area per lipid is an order parameter of the lipid monolayer the results are plotted against π as in **Fig. 3.17**. Especially, since the susceptibilities are proportional to $\left(\frac{\partial A}{\partial \pi}\right)_T$ for the isothermal compressibility κ_T and respectively to $\left(\frac{\partial r}{\partial \pi}\right)_T$ for the optical susceptibility according to equations 2.14 and 3.2.

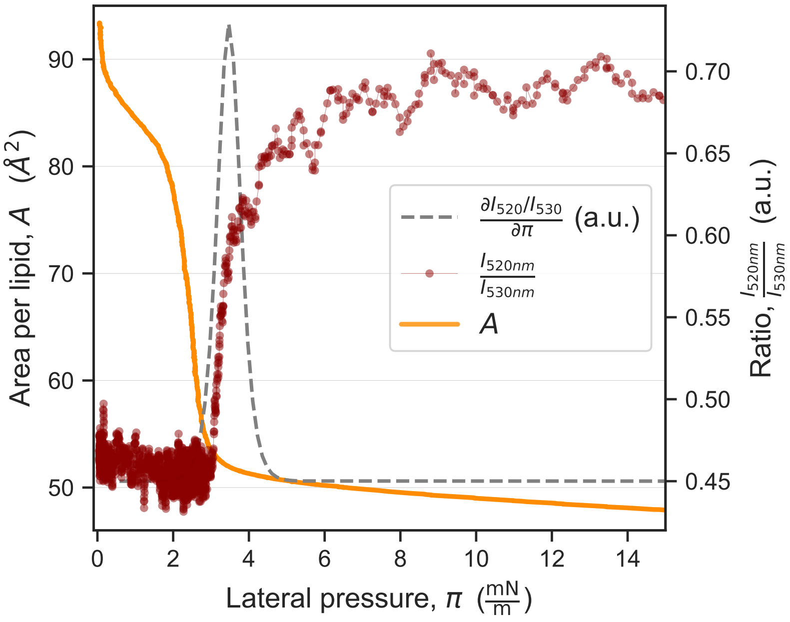

FIG. 3.17.: Mechanical and optical response of a DPPC monolayer under variation of the lateral pressure π. The order parameters of the system, the area per lipid A (orange line) and the optical ratio parameter $\frac{I_{520nm}}{I_{530nm}}$ (red dots) are presented. The derivative of the optical signal, the optical susceptibility (grey dashed line) reveals a sharp maximum during the transition.

The area A shows a sharp nonlinear shift resembling the transition of the monolayer over a width of $\approx 1\,\frac{mN}{m}$ at $\pi = 3\,\frac{mN}{m}$. This reflects the drastical reduction of the area per molecule upon entering the LC phase where the lipid tails become overall ordered and the distance between the lipid heads gets smaller. A similar nonlinear shift is detected in the ratio and amounts to $\approx 0.1/\frac{mN}{m}$. The ratio parameter is increased in the LC phase of the monolayer corresponding to the results in vesicle measurements where the ratio got increased in the ordered phase compared to the fluid disordered phase.

The width is similar to the detected transition width in the mechanical signal (FWHM = $(1.0 \pm 0.2)\,\frac{\mathrm{mN}}{\mathrm{m}}$).
The transition points are slightly shifted comparing the optical and the mechanical signal. It appears that the transition is detected at a higher pressure in the optical signal. In [62] temperature gradients between the measurement spots of the optical and the mechanical signal are discussed as origins for the small offset of the signal. The measurement spot of the optical signal is illuminated with a laser and a local warming of the lipid layer is most likely induced. Since the detection spots of the optical and the mechanical signal are spatially separated, they do not experience the same temperature during the measurement. In general, a temperature increase $T \uparrow$ leads to a new isotherm where the transition pressure $\pi_{Tr} \uparrow$ is increased. The whole plateau gets shorter and is shifted towards higher pressure values. At a given combination of A and π which is located in the plateau region at T_0 ($\pi = \pi_{Tr}(T_0)$) a local temperature increase to T_1 would shift the state away from the plateau at constant A. The heated layer spot is shifted towards the LE phase as $\pi_{Tr}(T_1)$ is higher than $\pi_{Tr}(T_0)$ and the plateau of T_1 is shorter. To induce the transition in this spot a further compression is necessary which is mirrored in these results. Nevertheless, it can be concluded that both signals mirror the transition correctly.

Hence, a coupling of optical and mechanical parameters of the monolayer can be established. The optical signal (the ratio parameter) is able to record the phase transition and can be used as reference for all other optically measured parameters.

LIFETIMES

To investigate the lifetime of *Atto488 DPPE* state-dependently an isotherm is driven stepwise. For each lifetime a single point measurement is necessary as a continuous recorded intensity trace would deliver merely one TCSPC histogram and consequently one lifetime for the whole measurement. At each approached point on the isotherm three measurements are conducted for 30 s. In **Fig. 3.18** the mean values of the intensity weighted lifetimes $\tau_{I_{av}}$ for varying lateral pressures π are shown. The associated stepwise recorded isotherm can be looked up in section A.7 in the Appendix.

A significant, nonlinear increase in the lifetime, $\tau_{I_{av}}$, with increasing π is correlated to the shift in the ratio parameter (**Fig. 3.18**). The nonlinearity in the ratio parameter is in accordance with the results on the continuously recorded isotherm (**Fig. 3.17**) where it was induced at similar pressures. In the LC phase the lifetime is increased by $\sim 0.25\,\mathrm{ns}$ compared to the LE phase.

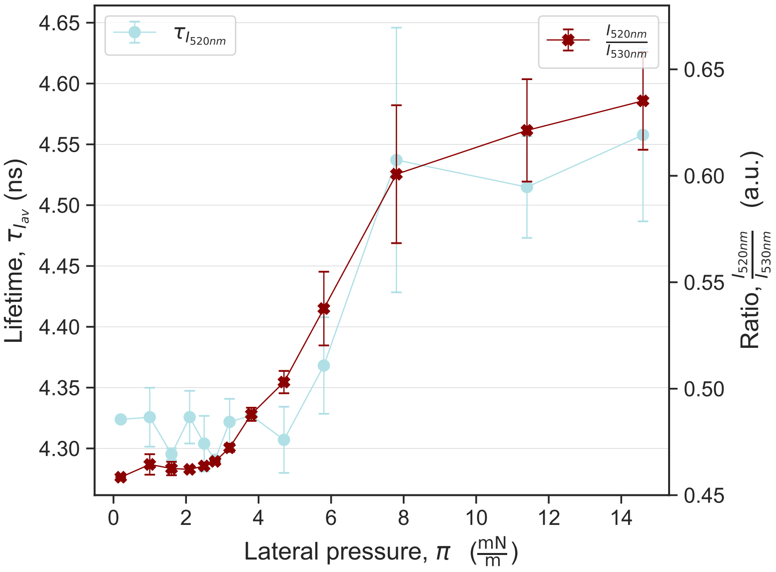

FIG. 3.18.: Intensity weighted lifetime $\tau_{I_{av}}$ (dots) of the 520 nm emission channel and the ratio parameter (x) upon state variation in the DPPC monolayer.

Thus, in contrast to the results obtained on DMPC vesicle measurements the fluorescence lifetime of *Atto488 DPPE* within a -PC monolayer reacts state-dependently. As both optical parameters presented here ($\tau_{I_{av}}$ and $\frac{I_{520\mathrm{nm}}}{I_{530\mathrm{nm}}}$) reveal their nonlinearity at similar pressures it is confirmed that both parameters are coupled to a similar underlying process, the phase transition.

The reason for the altered behavior of the dye regarding its lifetime in the -PC monolayer compared to -PC vesicles cannot be further clarified at this point. Concerning their conformation, both systems are fundamentally different whereas DMPC and DPPC merely differ in their chain length. It remains to mention, that similar results could be achieved for DMPS monolayer. In contrast to -PC, the -PS systems already showed a state-dependent fluorescence lifetime during the vesicle measurements.

FLUCTUATIONS IN THE FLUORESCENCE EMISSION SIGNAL

A phenomenon directly emerging in the fluorescence emission intensity signal will be discussed in the following. In **Fig. 3.19** the intensity data of the 530 nm channel is shown together with the simultaneously recorded isotherm during compression of the DPPC monolayer. The intensity trace has a binning of 1 ms and is not further smoothed. The raw data reveals a maximum in the intensity towards the end of the (compressed) plateau and simultaneously the signal gets noisier. These fluctuations start accordingly to changes in the ratio parameter and decline again when the shift is completed in the liquid condensed phase. Interestingly, comparing the optical susceptibility of the ratio parameter and the raw data of the intensity trace (as shown in **Fig. 3.19**) yields an apparent correlation of both maxima. Since the maximum in the optical susceptibility indicates the phase transition in the optical parameters the prominent behavior of the intensity seems transition related.

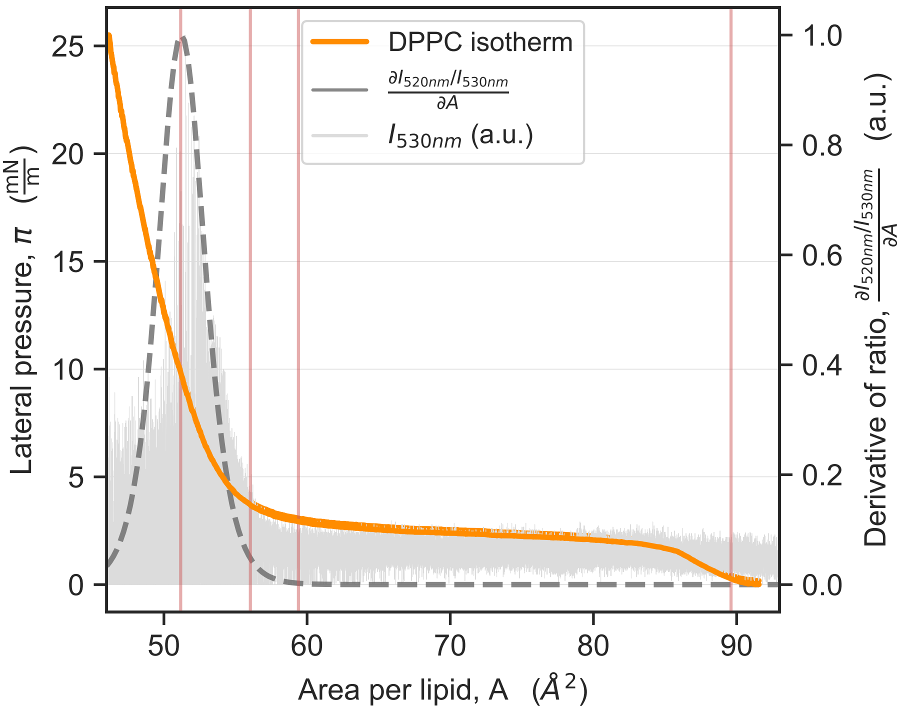

FIG. 3.19.: Raw data of the intensity channel at $\lambda = 530$ nm (light grey) superimposed in time with the output of the pressure sensor (orange). The optical susceptibility (grey dashed) derived from the ratio parameter reveals a maximum correlating with the maximum in the fluorescence emission intensity. The bars indicate the areas from which excerpts of the intensity are presented in the next figure.

A linear increase in the intensity upon compression of the area from the LE phase to the transition regime (plateau) would be expected due to an increased dye concentration in the focus volume. But the extent of noise here is not a consequence of the increasing intensity as it does not rise proportionally ($\Delta I \sim \sqrt{I}$) and the intensity itself increases highly nonlinear. However, the *noise* consists rather of deflections in the intensity signal as the signal decays to zero in between which is clearly visible in **Fig. 3.20** where excerpts of the fluorescence intensity traces are shown. The points within the isotherm where the excerpts are extracted from are marked as red bars in **Fig. 3.19**. Note, merely one intensity channel is shown in the following figures as both channels exhibit similar characteristics.

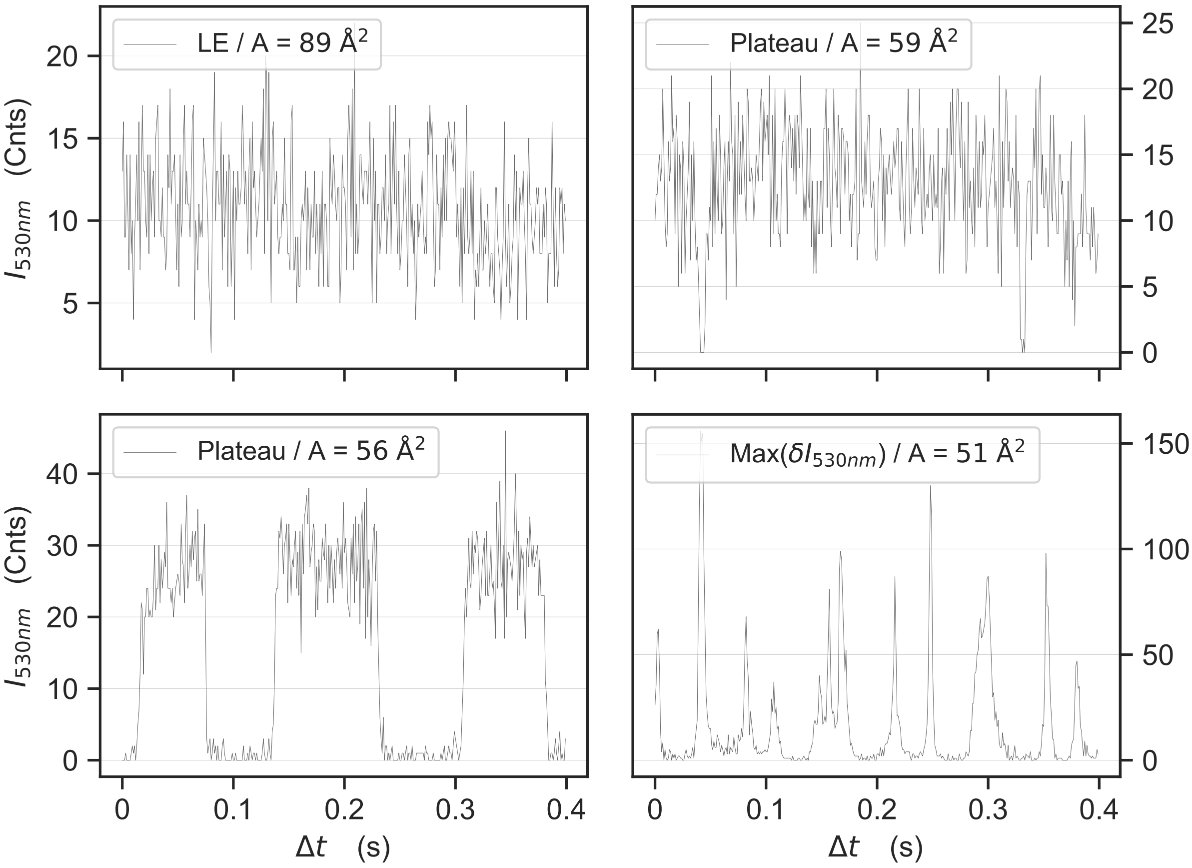

FIG. 3.20.: Excerpts of the intensity trace taken from **Fig. 3.19**, to which the area per lipid values A relate to. In the LE phase the intensity signal is unspectacular with a normal level of noise. In the plateau region gaps in which the intensity drops to zero start to appear. With increasing compression these gaps are getting more pronounced until there are rather bursts in the intensity from the zero level.

The first gaps appear in the transition region. With increasing compression (here: increasing time) more gaps appear and the time intervals or *opening times* of these gaps are getting longer. At some point a reversion takes place such that the gaps dominate and rather bursts in the intensity appear as outlier ($A = 51^{\,2}$ in **Fig. 3.20**). Note, the term *opening time* is not intended to anticipate the interpretation of this observation. It could as well be called *time interval* or *blinking time*.

To quantify the apparent fluctuations in the intensity a measure as follows is used:

$$(\delta I)^2 = (I(t) - \langle I(t) \rangle)^2 \tag{3.12}$$

The mean value of the intensity over time $\langle I(t) \rangle$ is realized through a moving average with an appropriate window length. By that, a sectional calculation is possible as the average should be calculated regarding to one state. The whole intensity trace, on the other hand, contains *all* states of the isotherm. With that, a parameter is accessed characterizing the raw data of the fluorescence intensity. Its course is shown in **Fig. 3.21** at the bottom. Apparently, $(\delta I_{530nm})^2$ is another parameter whose maximum aligns with the maximum in the optical susceptibility and the phase transition. An overview of the derived optical parameters in combination with the raw data of the emission intensity is presented in **Fig. 3.21**.

Thus, following the straightforward application of the definition of fluctuations to the fluorescence emission intensity a typical profile featuring a phase transition is derived as fluctuations are maximized. These fluctuations might originate directly in the dye molecule itself as the whole system is subject to massive fluctuations in *all* variables during the transition. The dye is coupled to and reflects the state of the interface which was already demonstrated by the optical susceptibility. Thus, the wording of this phenomenon with *fluctuations* seems to be appropriate after all independently of its origin.

With equation 3.12 the amplitude of these fluctuations is characterized. Now, the timescales shall be investigated likewise before a more profound interpretation of the results is in order. Upon the first impression a steady increase of the opening times appear which could identify floating domains as possible causers as well. On the other hand, it is conceivable that there is merely one underlying timescale and traces reflect different degrees of superimposition due to an increased occurrence of the single events.

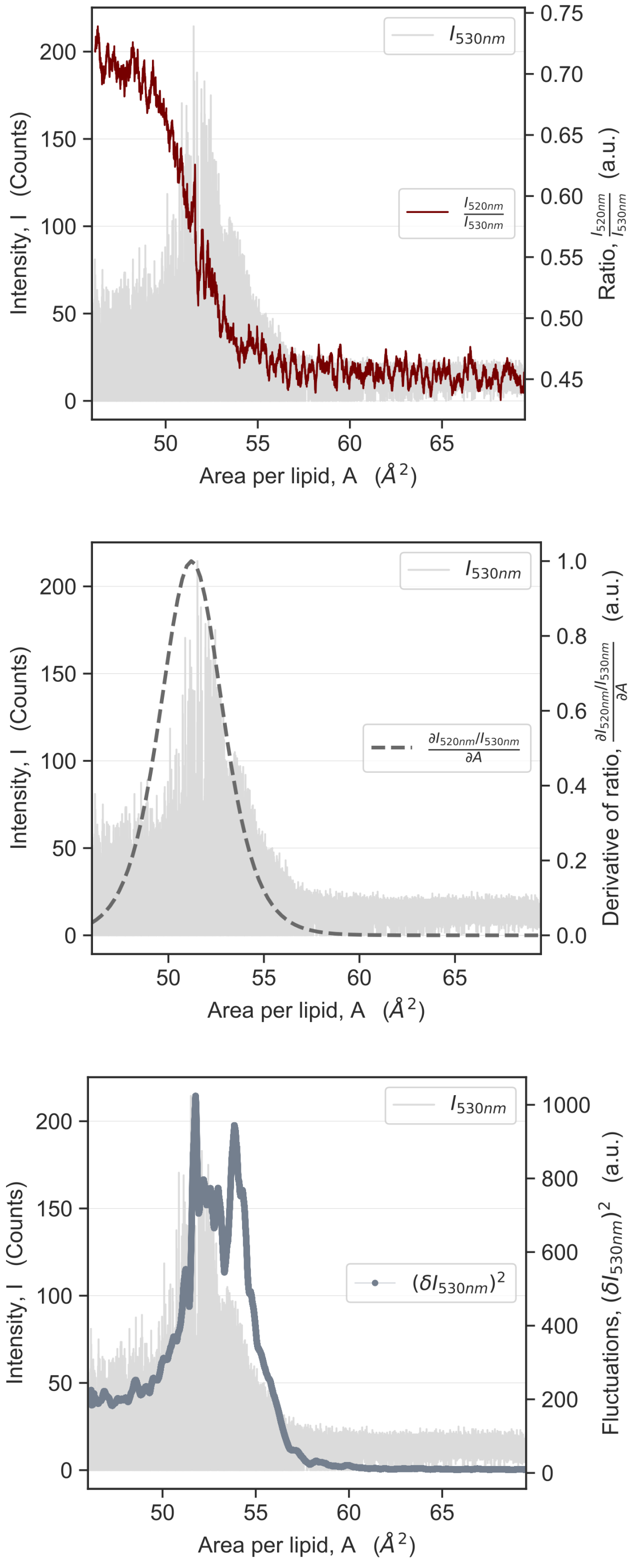

FIG. 3.21.: The raw data of the intensity I_{530nm} (light grey) combined with different optical parameters: the optical ratio parameter $r = \frac{I_{520\text{nm}}}{I_{530\text{nm}}}$ (top), the derivative of the ratio parameter $(\frac{\partial r}{\partial A})$ (center) and the fluctuations of the intensity $(\delta I_{530\text{nm}})^2$. The maximum in $(\delta I_{530\text{nm}})^2$ correlates with the maximum of I_{530nm} and the maximum of the optical susceptibility describing the derivative of the ratio parameter.

To avoid effects or artefacts of the driving barrier in the intensity time trace during the recording of the isotherm, point measurements are conducted. An isotherm is again driven stepwise and at every stopping point a measurement is conducted at steady conditions. It comes with no surprise that similar results are gained from the steady measurements. **Figure 3.22** shows the location of the maximum of $(\delta I_{530\mathrm{nm}})^2$ close to the transition pressure π_{Tr} and aligned to the transition regime mirrored by the shift in the ratio parameter $\frac{I_{520\mathrm{nm}}}{I_{530\mathrm{nm}}}$.

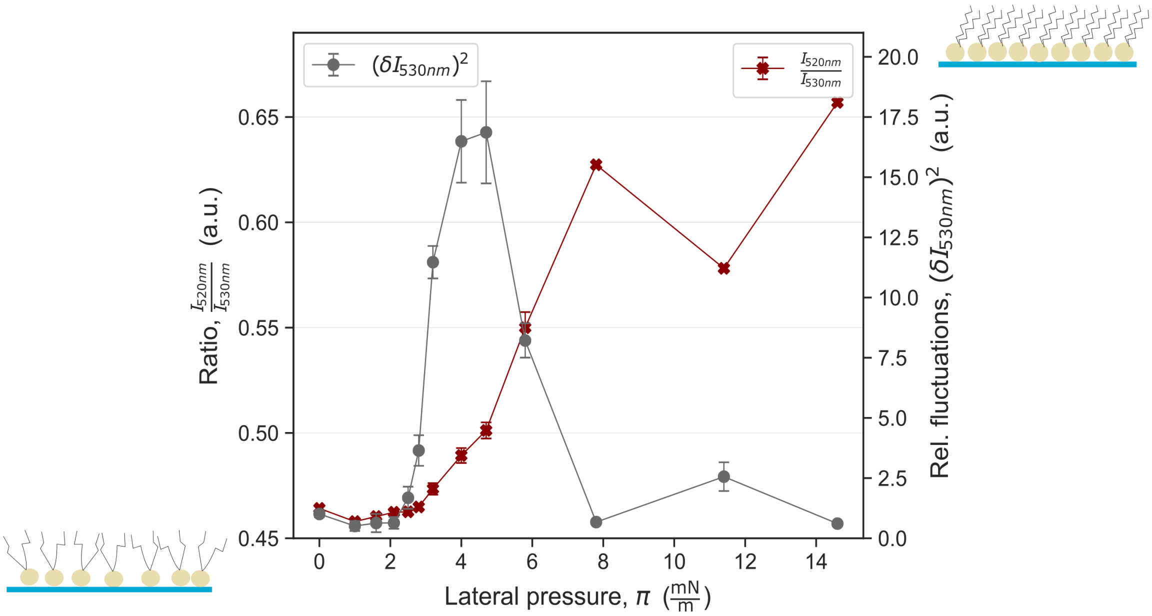

FIG. 3.22.: Results of the optical ratio parameter $\frac{I_{520\mathrm{nm}}}{I_{530\mathrm{nm}}}$ and the intensity fluctuations $(\delta I_{530\mathrm{nm}})^2$ during steady state point measurements at different lateral pressures π. The nonlinear increase in the ratio parameter indicating the transition from the LE to the LC phase correlates with the maximum in the amplitude fluctuations $(\delta I_{530\mathrm{nm}})^2$.

Note, with this type of measurement it is possible to resolve the single phase states of the monolayer in more detail. Referring to the isotherm in **Fig. 3.19** the LE and LC phase are monitored for ~ 30 s each whereas the plateau region is monitored over ~ 200 s. Especially in the LC phase the isotherm is not recorded far enough in order to make sufficient statements about that phase. Since the transition in the optical parameters is slightly delayed upon compression there is most likely not enough time for the system to fully adapt into the LC state. That becomes visible as $(\delta I_{530\mathrm{nm}})^2$ in the LC phase decreases back to the level prior to the transition (LE phase) in the steady point measurements (**Fig. 3.22**) while this decrease is merely indicated in the continuous measured isotherm (**Fig. 3.21**). **Fig. 3.23** underlines this observation: There are again four excerpts of intensity traces presented, this time taken from the steady measurements. The fourth plot at 7.8 $\frac{\mathrm{mN}}{\mathrm{m}}$ (LC phase) shows a trace similar to the one extracted from the LE phase in **Fig. 3.20**. Thus, the intensity signal is restored after the transition. The other traces appear similar to the already presented ones: At $\pi = 2.1\,\frac{\mathrm{mN}}{\mathrm{m}}$ the layer is in the LE phase. At $\pi = 3.2\,\frac{\mathrm{mN}}{\mathrm{m}}$ and $\pi = 4.7\,\frac{\mathrm{mN}}{\mathrm{m}}$ the transition takes place. Between 3.2 $\frac{\mathrm{mN}}{\mathrm{m}}$ and 4.7 $\frac{\mathrm{mN}}{\mathrm{m}}$ a shift in the perceived level of intensity happens: At 3.2 $\frac{\mathrm{mN}}{\mathrm{m}}$ the general intensity level is at $\sim$ 35 Cnts and is interrupted by sections where the intensity drops to zero. But, at 4.7 $\frac{\mathrm{mN}}{\mathrm{m}}$ it seems like the overall intensity level dropped to zero and there are rather bursts of the intensity where $I_{530nm} \neq 0$. Nevertheless, a signal without gaps or bursts is restored at 7.8 $\frac{\mathrm{mN}}{\mathrm{m}}$ in the LC phase.

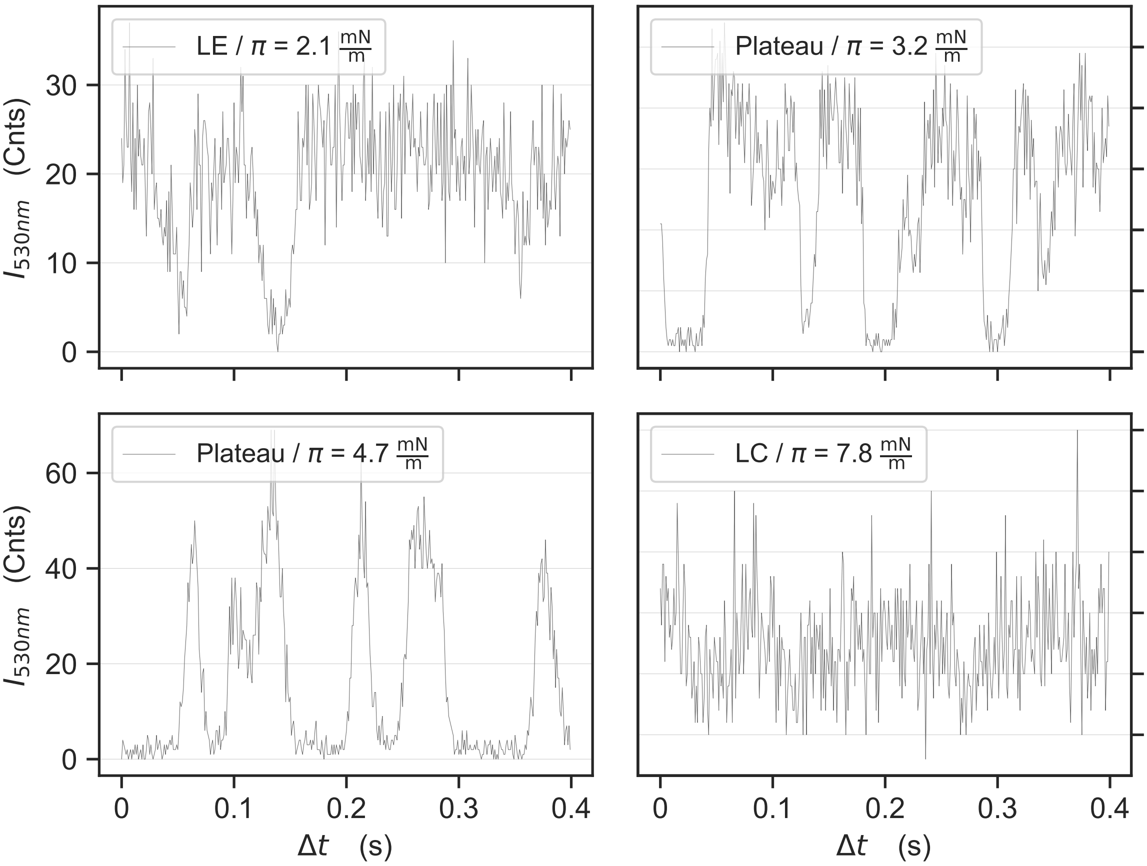

FIG. 3.23.: Excerpts of fluorescence emission intensity traces at different pressures. The lateral pressure values relate to the results in **Fig. 3.22**. 2.1 $\frac{\mathrm{mN}}{\mathrm{m}}$ is in the LE phase while 3.2 $\frac{\mathrm{mN}}{\mathrm{m}}$ and 4.7 $\frac{\mathrm{mN}}{\mathrm{m}}$ are in the transition regime. At 7.8 $\frac{\mathrm{mN}}{\mathrm{m}}$ the transition is completed and the monolayer in the LC state.

The lifetimes of these intensity fluctuations or rather the durations of the *off* sections in which the intensity is dropped to ~ 0 are systematically investigated. They will be called *opening times* in the following and refer to the temporal length of the *gap* in the emission intensity. They are detected automatically via a self-implemented algorithm in python.

In **Fig. 3.24** the results are presented as classifications of the opening times τ in histograms (binning size: 6 ms). The results of four different intensity traces, namely the associated full length traces (30 s) to the excerpts shown in **Fig. 3.23** are presented.
There are mostly isolated and rather short gaps in the LE and LC phase state (2.1 $\frac{\text{mN}}{\text{m}}$ and 7.8 $\frac{\text{mN}}{\text{m}}$). Whereas the distribution of events respectively their opening times τ is much broader during the transition ($\pi = 3.2\,\frac{\text{mN}}{\text{m}}$ and $\pi = 4.7\,\frac{\text{mN}}{\text{m}}$).

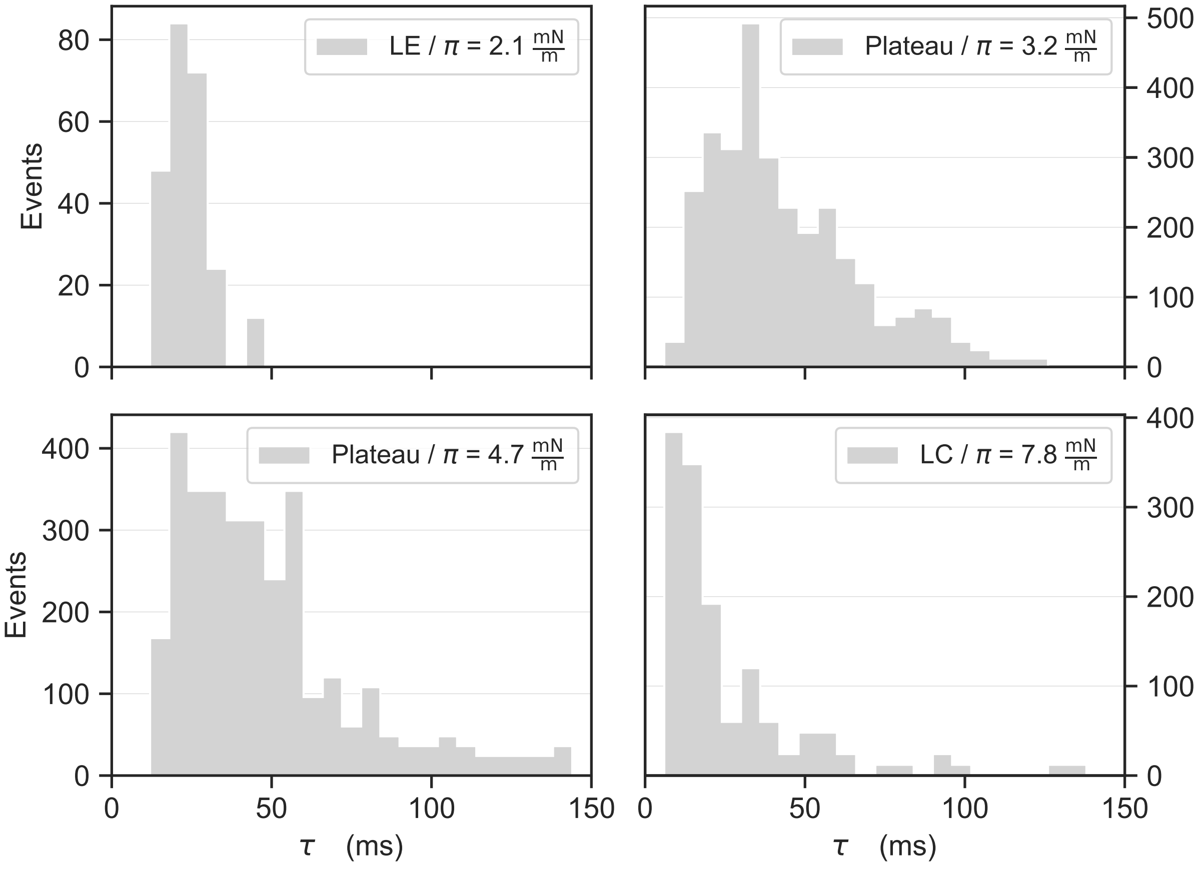

Fig. 3.24.: Histograms of the opening times τ extracted from the full length intensity traces which excerpts are shown in **Fig. 3.23**. Bin size is 6 ms and each intensity trace is 30 s long.

Interestingly, phenomenologically these histograms resemble results from state dependent permeability measurements on lipid bilayers [4]. There, current fluctuations and their timescales were classified in histograms as well. Within the transition regime the timescales got significantly longer (from 3 ms to 20 ms in average) and the histograms reveal a broader distribution. Outside of the transition regime rather short bursts were detected. These results are based on state dependent defects in the lipid bilayer upon which a current flow is detected. The formation of pores happens due to thermal area fluctuations.

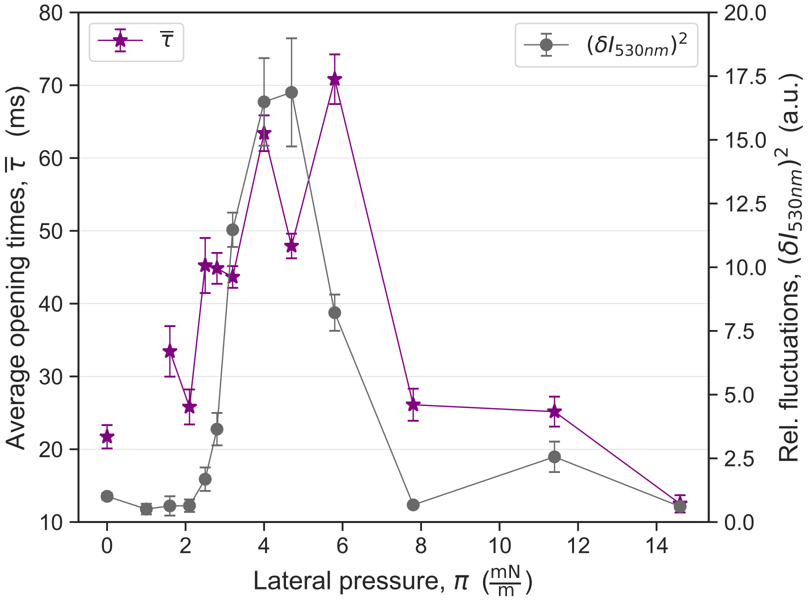

FIG. 3.25.: Overview of the intensity fluctuation related parameters gained from the systematical analysis of the single intensity traces. The timescales of the fluctuations are represented by the average opening times $\overline{\tau}$ upon variation of the lateral pressure π. Additionally, the measure for the amplitude fluctuations $(\delta I_{530\mathrm{nm}})^2$ calculated from the same curves is shown. Both parameters reveal a correlated behavior which, in turn, is correlated to the phase transition in the monolayer. At $\pi = 1\,\frac{\mathrm{mN}}{\mathrm{m}}$ no events with a significant timescale were detected.

It has been discussed and proven in theory that the fluctuations lifetime τ, represented by the *pore opening time*, is proportional to the heat capacity c_p and thereby to the isothermal compressibility κ_T [63, 4]:

$$\tau \sim c_p \sim \kappa_T \tag{3.13}$$

Though, this was discussed for lipid bilayers similar relations were found on monolayers e.g. for the relaxation times of pulses. According to Onsager, relaxation times and fluctuation lifetime are similar [64].

For the monolayer here, the average opening times $\overline{\tau}$ derived from the analysis of the timescales of the single intensity traces are presented in **Fig. 3.25**. A correlation of the fluctuation amplitudes $(\delta I_{530\text{nm}})^2$ and the average opening times $\overline{\tau}$ is clearly visible. They reveal a maximum in the transition regime ($\overline{\tau} \approx 60\,\text{ms}$). Thus, the extracted timescales feature characteristics of fluctuation lifetimes. Additionally, they are indeed coupled to the susceptibilities of the system as it has been shown already for $(\delta I_{530\text{nm}})^2$ before:

$$\kappa_T \sim \frac{\partial \frac{I_{520\text{nm}}}{I_{530\text{nm}}}}{\partial \pi} \sim (\delta I_{530\text{nm}})^2 \sim \overline{\tau} \tag{3.14}$$

DISCUSSION

For the emission signal to drop there are either photophysical effects of the dye responsible, happening on a molecular level, or the layer itself has to *escape* from the focus volume. With that, the embedded dye would not be excited anymore. Surface undulations to that extent that the layer leaves the z-axis of the volume or area-density fluctuations, pore formation etc. such that the layer has a defect within the xy plane would be conceivable.
Thermodynamically, pore formation within the membrane is possible. Lipid ion channels or pores within lipid layers as a consequence of area fluctuations have been proposed and investigated [39]. Indeed, a relation concerning the pore size states:

$$(\Delta A)^2 \propto \kappa_T \tag{3.15}$$

Hence, the area of the pore ΔA is proportional to the compressibility of the layer which fits the observations of the timescales. While the pressure sensor measures the macroscopic behavior of the monolayer, the objective measures a localized spot of $\sim 0.5\,\mu\text{m}^2$. Thus, within the optical signal it is in principle possible to detect localized phenomena such as pore formation. However, the typical pore radius is given by 1 nm [39, 4]. Considering this, it does not seem likely that pores are responsible for these fluctuations. One pore could not replace the whole layer within the detection volume. Though several pores could produce a measurable effect.

The role of the domains remains unclear. They appear during the transition and represent the phase separation or rather the phase coexistence of the system. On the one hand, domains appear darker due to the photoselection effect but it may be doubted that the intensity drops completely to zero when a domain enters the focus volume. Especially, since there is a pronounced intensity signal measurable when the transition to the LC phase is completed. **Figure 3.23** shows that the intensity trace in the LC phase is free of defects and the signal strength of the LE phase is nearly restored. Thus, the dye must embed quite homogeneously in both phases. It has been reported for a DPPC monolayer and the dye DiI-C_{18} that the dye concentration is crucial whether it embeds into the LC phase [65]. A separation of the dye from the DPPC monolayer was observed for 10^{-4} mol%. At higher concentrations this effect vanished. Thus, it is highly unlikely that a similar separation is present here at 0.05 mol%.

An analysis of the temporally resolved ratio parameter (point by point division of the intensity traces) is not fruitful as the ratio during the gaps cannot be analyzed due to several entries with $I = 0$. Thus, a conclusive statement about the phase state within these gaps cannot be made.

If domains would be responsible for the modulation of the signal they need to cross the focus quite fast. Calculations of the velocity of the domains by means of video recordings via the ocular of the microscope do not fit the required velocity extracted from the time traces of the emission intensity. However, the transition is directly coupled to the domains as the largest thermodynamical fluctuations are located at their interfaces [24]. Both aspects cannot be approached independently.

In general, reasons for the intensity dropping to zero are manifold. The most simple explanation would be the blinking of the dye molecule which is usually in the ns timescale. As stated before, during the phase transition relaxation times get longer. But it would require a synchronized blinking if more than one molecule is in the focus. Mostly, there is no stepwise behavior visible but rather an all or none behavior. Effects such as thermal undulations of the surface have been reported for measurements on monolayers before [66]. To what extent they are involved in these measurements cannot be stated.

Considering this phenomenon from a thermodynamic point of view it features every characteristic of a fluctuating variable including its timescales featuring fluctuation lifetimes. It is coupled to the systems thermodynamics and is sensitive to its state and the transition. Although, the origin remains unclear and cannot be assigned to a certain parameter in the system, it is possible to detect the thermodynamic fluctuations of the system directly. While the pressure sensor monitors the macroscopic state due to the cooperativity of the layer the optical signal measures locally. It seems likely that local fluctuations can be resolved.

3.3. KINETICS IN BIOLOGICAL SYSTEMS

Living systems are not merely structures, in contrary, they stand out due to ongoing processes everywhere. In section 2.3.1 the coupling of the physical state of membranes to biological functions has been indicated. Fluorescence correlation spectroscopy is a powerful tool for measuring dynamics within a system and extracting characteristic timescales. This is an essential step towards approaching a potential interplay between state and function. After an introduction to the principles of this method, exemplary processes of the membrane such as diffusion and protonation will be discussed and investigated on artificial, lipid interfaces.

3.3.1. PRINCIPLES OF FLUORESCENCE CORRELATION SPECTROSCOPY

The underlying principle of the **F**luorescence **C**orrelation **S**pectroscopy (FCS) is based on the analysis of fluctuations $\delta I(t)$ in the fluorescence intensity signal $I(t)$:

$$\delta I(t) = I(t) - \left\langle I(t) \right\rangle \tag{3.16}$$

The temporal average is denoted by $\left\langle I(t) \right\rangle$. If the fluctuations are not randomly distributed but rather follow a pattern and appear systematically in time, an autocorrelation function of the intensity trace will give rise to the according characteristic timescales [67]:

$$G(\tau) = \frac{\left\langle \delta I(t) \cdot \delta I(t+\tau) \right\rangle}{\left\langle I(t) \right\rangle^2} + 1 \tag{3.17}$$

Mathematically, it describes a convolution of the signal with itself. By that, similarities within the intensity signal are revealed upon varying lag times τ. For a schematic overview refer to **Fig. 3.26**

Fluctuations within the fluorescence signal either emerge due to dye molecules entering and respectively leaving the focus volume or due to blinking processes of the dye molecule itself. The most basic blinking mechanism which is subordinated by every dye is given due to the lifetime of the dye in the excited state. After relaxation (~ ns) it follows a cycle of reexcitation. Depending on the temporal resolution this process is resolvable in the correlated curve. In principle, the used setup (as introduced in section 3.2.2) contains a working mode where the temporal resolution can be enhanced up to nanoseconds. For that, the excitation laser is switched to the continuous mode as the pulsed excitation limits the temporal resolution up to the time interval between two laser pulses ($1/f_{Laser}$).

However, for the here presented measurements, the simultaneous recording of TCSPC curves is preferred and, for that, the pulsed laser mode is necessary.

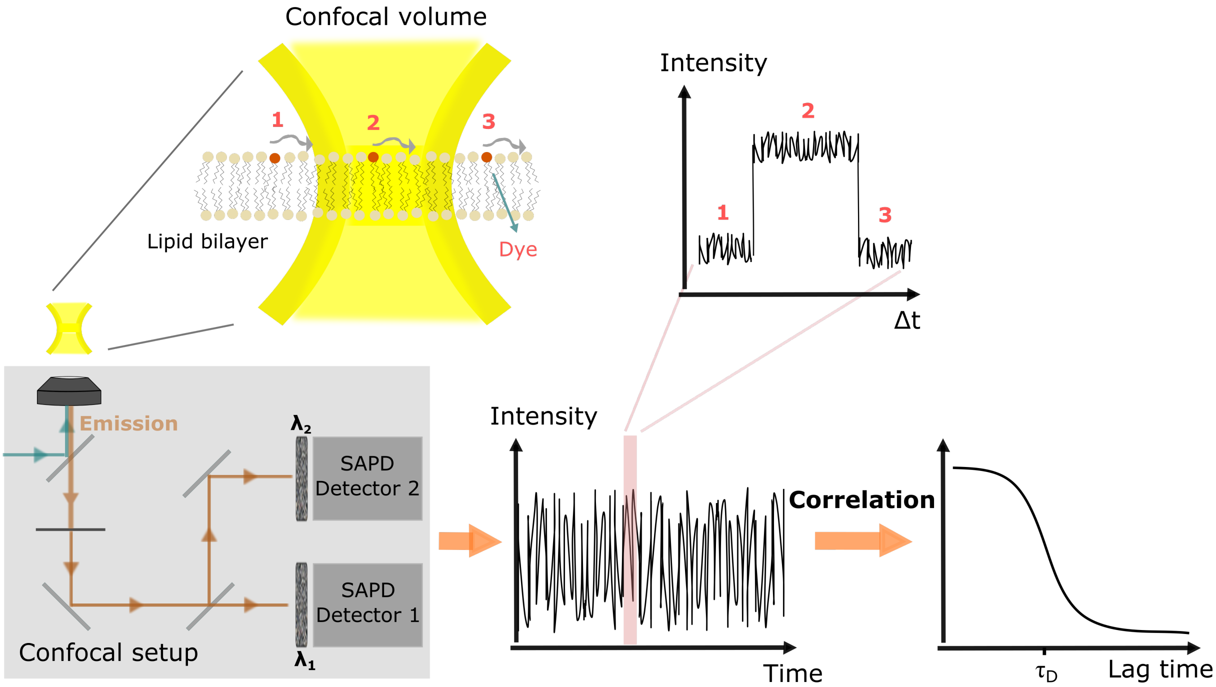

Fig. 3.26.: Principle of **F**luorescence **C**orrelation **S**pectroscopy: The basis is built on a confocal setup (lower left; introduced in more detail in section 3.2.2). The fluorescence emission intensity traces contain the optical response of, ideally, one dye molecule at the time. This is illustrated and simplified exemplary for diffusion in the upper row: Two-dimensional diffusion of a dye molecule in a lipid bilayer trough the confocal volume (upper left) and its associated emission intensity trace $I(t)$ (upper right) for different points in time (**1**,**2**,**3**). While it resides in the confocal volume the emission signal of the dye is detected. Upon leaving the detection volume the intensity drops. The recorded intensity traces are than correlated or in simplified terms, *compared* with themselves for different lag times τ. The **correlation** is executed directly in the software *SymPhoTime 64* (PicoQuant) that is acquiring the data as well. The diffusion time τ_D appears as the lag time where the signal shows a high level of resemblance with itself. Consequently, the correlation function rises (lower right). Considering diffusion as the only monitored process, τ_D can be identified as the lag time where the signal of the normalized correlation function has dropped to $\frac{1}{2}$.

There are other photophysical processes originating in the dye itself such as excitation of the molecule into the triplet state, which is typically located in the microseconds range [68]. Nevertheless, the most basic process is the diffusion. All other processes are limited by the time the molecule is located within the focus volume, which is mainly determined by its diffusion coefficient D. Although describing a **random** walk, diffusion or the means square displacement of the molecule for the time t

$$\left\langle r^2(t) \right\rangle = \left\langle (r(t) - r(0))^2 \right\rangle \tag{3.18}$$

can be quantified with the characteristic diffusion coefficient D.
This is described via the Einstein relation for two-dimensional diffusion:

$$\left\langle r^2(t) \right\rangle = 4Dt \tag{3.19}$$

Hence, the passage through the focus (intensity *on*) for the diffusion time τ_D until the dye leaves the volume (intensity *off*) causes a blinking in the emission intensity trace (refer to **Fig. 3.26**). It becomes obvious that low dye concentrations are necessary to detect processes of individual molecules. Otherwise, there would be a huge overlay of processes in the intensity trace increasing the level of noise.
The diffusion coefficient D is related to the diffusion time τ_D in the way that

$$D = \frac{\omega_1^2}{4\tau_D} \tag{3.20}$$

where ω_1 is the radius of the confocal volume. The diffusion time τ_D in turn, can be derived from the correlation curve.

The correlation curve contains *all* processes that are present over the range of the applied lag times τ merely limited by the temporal resolution of the detection mode. To distinguish the individual processes and extract their according parameters from the calculated curve, model functions are applied. Theoretically derived, they can be assembled according to the (expected) apparent processes in the measured system. Note, this requires prior knowledge about the present processes involved in the system, though.

If one species with three-dimensional diffusion is present, and no further processes, the model function can be written as [69]:

$$G_D(\tau) = \frac{1}{N} \frac{1}{\left(1 + \frac{\tau}{\tau_D}\right)} \frac{1}{\sqrt{1 + \beta^2 \frac{\tau}{\tau_D}}} \tag{3.21}$$

Here, N denotes the number of fluorescent particles in the focus and β is a structural parameter concerning the focus size. It is typically estimated by $\beta \approx 5$ and refers to the ratio of focus length in z direction and the focus width ω_1 in x-y direction.
In terms of a lateral diffusion e.g. in a two-dimensional membrane equation 3.21 is simplified to:

$$G_D(\tau) = \frac{1}{N}\frac{1}{\left(1+\frac{\tau}{\tau_D}\right)} \tag{3.22}$$

Some parameters can be estimated without analysis. For $\tau = 0$ follows $G_D(0) = \frac{1}{N}$. Thus, the y axis intercept of G_D indicates the inverse concentration of the dye molecules. Since $G_D(\tau_D) = \frac{1}{N}\frac{1}{2}$ the diffusion time τ_D equals the lag time τ where the y intercept has dropped to its half value (refer to **Fig. 3.26**). Shifts in the diffusion time are visible upon associated changes in position of the whole correlation curve on the x axis. For $N \uparrow$ the y intercept decreases to lower values: $G(0) \downarrow$.
If the shape of the curve is altered and cannot be aligned with the model function anymore the nature of the diffusion has most likely changed. For example, an underlying active transport would increase the slope of the curve. A hindered diffusion as to a rather heterogenous media would impact the shape as well. These processes have been described in [69].
In terms of two diffusing species the equation is expanded to [70]:

$$G_D(\tau) = \frac{F}{N}\frac{1}{\left(1+\frac{\tau}{\tau_{D1}}\right)} + \frac{1-F}{N}\frac{1}{\left(1+\frac{\tau}{\tau_{D2}}\right)} \tag{3.23}$$

The diffusion times are τ_{D1} and τ_{D2} and F denotes the according fraction belonging to species one of all molecules N. Analogously, $(1-F)$ denotes the fraction associated to the second species.

Other processes, which can be characterized by a blinking behavior feature two apparent states, bright B and dark D. In the dark state, no photons are emitted. The switching between these states is associated with on respectively off rates k_B and k_D

$$\mathrm{B} \underset{\mathrm{k_B}}{\overset{\mathrm{k_D}}{\rightleftharpoons}} \mathrm{D} \tag{3.24}$$

and a relaxation time τ_T:

$$\tau_T = \frac{1}{\mathrm{k}_D + \mathrm{k}_B} \tag{3.25}$$

These kind of processes or rather reactions can be described with exponential decays as to [67]:

$$G_T(\tau) = \frac{1}{1-T}\left(1 - T + Te^{-\frac{\tau}{\tau_T}}\right) \tag{3.26}$$

The fraction of molecules in the dark state is denoted by T. A process featuring this category is the triplet state. While the dye molecule is in its triplet state it does not emit fluorescence photons. By equation 3.25 it is apparent that the blinking rate is coupled to the relaxation time of this process. As the triplet state is quantum mechanically forbidden it is less likely to excite than the singlet state (fluorescence). Hence, this process is located on longer (relaxation) timescales compared to the fluorescence lifetimes.

This model can be applied to processes involving blinking rates in general. This requires that one state is in good approximation completely dark and a two-state model applicable. To build a model that includes more than one process a combination of the above presented, individual models is possible. In general, this can be formulated as:

$$G(\tau) = G_D(\tau)G_T(\tau) + 1 \tag{3.27}$$

This model would describe a diffusion $G_D(\tau)$ combined with a potential triplet population $G_T(\tau)$. Note, this factorization is applicable for independent processes.

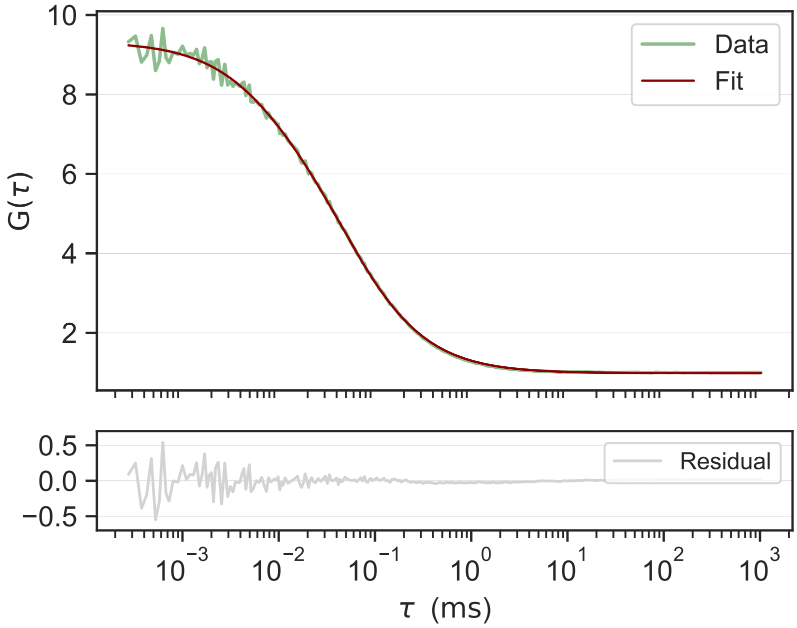

FIG. 3.27.: Exemplary correlation curve: Measurement on freely diffusing *Atto 488* dye in water. According to the included timescales (diffusion and triplet blinking) a model function is chosen and fitted to the data. From that, the timescales can be extracted as fit parameters. Bottom: Residuals of the fit describing the deviation of the fit from the measured data (Residuals = Data - Fit).

An exemplary correlation curve is shown in **Fig. 3.27**. In general, according to (expected) included processes a model function is assembled and fitted to the data. From this analysis, the timescales of the processes can be extracted as the fit parameters.

REFERENCE MEASUREMENT

While it is sufficient to estimate the structure parameter β ($= \frac{\omega_2}{\omega_1}$) in the fitting model, the radius of the focus volume ω_1 (at its narrowest point) is calculated by means of a reference measurement. Here, ω_1 is the distance between the central point with maximal intensity of the gaussian beam profile and the point where the intensity has dropped to 1/e of the maximum value.

The measured diffusion times τ_D are dependent on the focus volume and are not comparable with other setups. Thus, in general, a conversion to the universal diffusion constant D is aimed for.
An established dye of known diffusion coefficient D is measured in water. The correlation curve is fitted with a one-diffusion model and the diffusion time τ_D is extracted. From that, the known formula

$$\tau_D = \frac{\omega_1^2}{4D} \tag{3.28}$$

is consulted and ω_1 calculated. The free *Atto488* dye has the diffusion coefficient $D = 400\,\frac{\mu\text{m}^2}{\text{s}}$ in water at $T = 25\,°\text{C}$ [71] and a typical diffusion time of $\tau_D = 0.045\,\text{ms}$ is measured in this setup with the 60X water immersion objective. From that, $\omega_1 \sim 270\,\text{nm}$ follows. Note, that as to

$$D = \frac{\text{k}_\text{B} T}{6\pi\eta(T)r} \tag{3.29}$$

the diffusion coefficient itself is dependent on temperature T and viscosity $\eta(T)$ while the viscosity is itself temperature dependent. Typically, the reference measurement was conducted around 20 °C. Hence, the value of the diffusion coefficient is corrected to $T = 20\,°\text{C}$ with the method in [71] and $D = 350\,\frac{\mu\text{m}^2}{\text{s}}$ respectively $\omega_1 \sim 250\,\text{nm}$ is derived. With that the determination of ω_1, it is possible to convert each diffusion time into its associated diffusion constant. Note, this varies for each objective.

For approaching FCS measurements with more than one timescale each time constants must be characterized carefully. As the models contain several fit parameters each timescale has to be evaluated beforehand ideally. A direct fit of all variables will most likely lead to various possible solutions as many local minimums are possible for a fit function with several fit variables.

By identifying parameters in separate measurements it is possible to limit the degree of freedom during the fitting. This could include a power series, in which the excitation strength is gradually increased to identify and characterize processes that are dependent on the laser intensity, similar to the series conducted for the TCSPC curves (Appendix A.5.2). For example, the occurrence of the triplet state has a low probability in general, but, with increasing laser intensity it gets more likely to observe. Increasing the intensity ensures more potential excitations of the molecule in a given time interval. Thus, by increasing the excitation strength, while everything else remains unchanged, this process would appear more often. This behavior could be identified in a power series and associated to the triplet state. The associated timescale could be extracted and, by that, distinguished from other processes.
A power series is not presented here as the triplet state is well characterized [68]. For the excitation intensities applied, τ_T is estimated with 1.5 μs. It is a parameter independent of the focus size and can be fixed during the analysis to limit the number of unknown parameters.
With increasing excitation intensity the chance to bleach the dye rises. It is a statistical process and defined by an average amount of lifecycles of the dye molecule after which it is not excitable anymore. It becomes an issue once the chance to bleach the dye during its traversing through the confocal volume gets significant. This would lead to an underestimation of the diffusion time as the *switching off* of the intensity would be mistakenly correlated and assigned to the leaving of the dye from the focus. Thus, the excitation strength has to be chosen carefully and for other (rather unknown) processes this effect must be investigated beforehand.

In general, diffusion of the fluorescent molecule is the most basic timescale for characterization as it exhibits the longest timescale. The observation of the triplet state or other blinking processes is merely possible while diffusion of the dye trough the focus. Timescales longer than the diffusion time cannot be analyzed properly.

3.3.2. STATE-DEPENDENT DIFFUSION IN ARTIFICIAL LIPID SYSTEMS

The fluorescence correlation spectroscopy is applied to artificial membranes in the following. The goal is to gather information of the Brownian movement of the dye-lipid complex within the membrane in general. Firstly, the method shall be established and tested and secondly this behavior shall be observed phase-dependently. Additionally, these measurements shall prepare for the transfer of the method to living cells.
Note, it will be mostly referred to *diffusion of lipids* although technically the diffusion of the dye-lipid complex is monitored and not an individual lipid of the ensemble. As the dye embeds itself into the lipid matrix via its lipid anchor and is coupled to the hydrophilic headgroup the movement of the complex resembles the movement of the anchored lipid itself. A homogenous distribution of the dye within the lipid interfaces is expected since very small concentrations most likely avoid a phase separation between the dye-lipid complex and the pure lipids.

DIFFUSION IN GIANT UNILAMELLAR VESICLES

The first system at hand are lipid giant unilamellar vesicles (GUVs). Due to their size ($d \approx 10\,\mu$m - $100\,\mu$m) which partially exceeded the 80 x 80 μm^2 scanning area, they are the closest model for a cell one can get from pure lipids. The GUVs are produced via electroformation following a standard protocol (refer to Appendix A.3). The production has to take place at least $\approx$ 10 °C above the transition temperature of the used lipid and is not possible for charged lipids. To this, DOPC is a convenient choice of lipid ($T_m = -17$ °C [72]) and forms large and smooth vesicles at room temperature. In **Fig. 3.28** (A) a typical GUV of DOPC at room temperature is presented in a cross sectional scan. It contains 0.005 % of embedded *Atto488 DPPE* which is the standard dye concentration for GUVs throughout this section. The vesicle features a pronounced round shape. The vesicles are *glued* to the glass surface of a coverslip via a neutravidin-biotin binding protocol. Before that, different sugar solutions facilitate the sinking of the individual GUVs to the ground. The protocols are listed in the Appendix A.3. In **Fig. 3.28** (B) a cross sectional scan in z direction shows the indicated glass at the bottom of the GUV. Note, the thickness of the membrane at the top and the bottom of the vesicle appears wider due to the shape of the confocal volume: It is roughly five times longer in z-direction than in x or y direction, which is reflected in the β parameter as well. Thus, the distribution of the intensity appears broader in z direction. The anchor is distinct visible in **Fig. 3.28** (C) although this particular vesicle is an exception as they are predominantly unilamellar. In **Fig. 3.28** (C) and (D) free dye respectively dye accumulations are visible inside of the GUVs. The measurements were conducted in the same chamber as already employed for SUV measurements that is connectable to a heating bath (section 3.2.3).

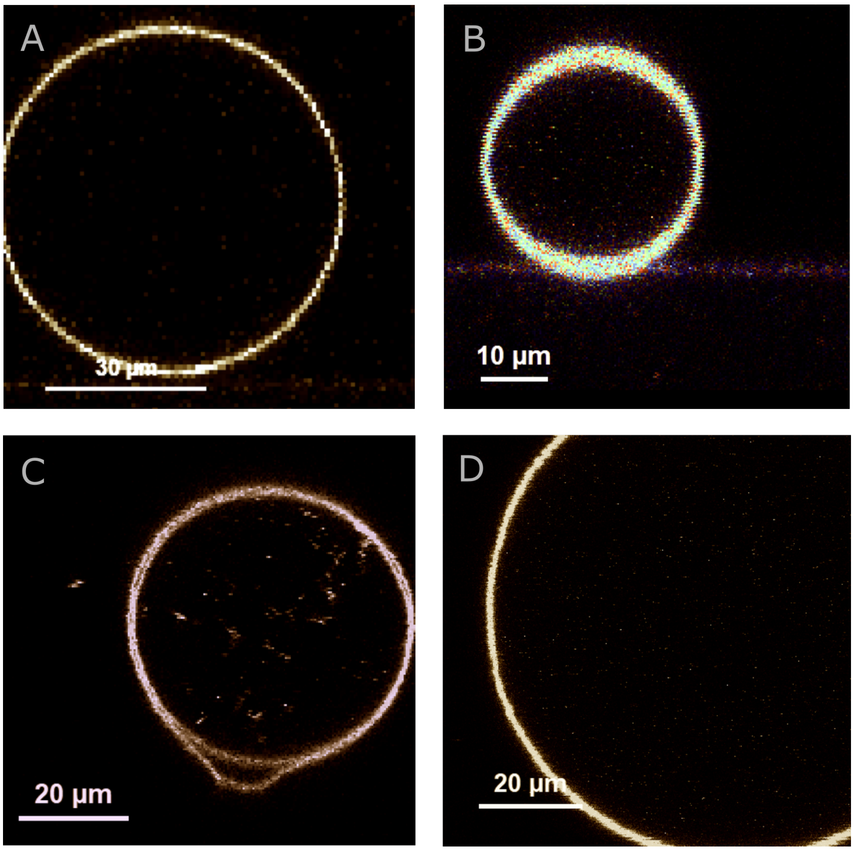

FIG. 3.28.: Cross sectional fluorescence scans of different DOPC GUVs with 0.005 % *Atto488 DPPE*: A - Scan of a DOPC GUV with average appearance. B - Scan in z direction shows the glass of the cover slide at the bottom. Note, the thickness of the membrane at the top and the bottom of the vesicle appears wider due to the shape of the confocal volume. C - Anchor of a double layered GUV is visible. D - Example of an extraordinary huge GUV exceeding the maximal scanning range of 80 μm in each direction ($d > 80\,\mu$m).

Spots for local point measurements in the membrane are chosen upon prior performed cross sectional scans as depicted in **Fig. 3.29**. Due to the comparably large size of the vesicles ($d \approx 10\,\mu$m - 100 μm) the membrane curvature is low and within the focus ($V \approx 1$ fl) the membrane is almost planar. To assure that the membrane is located in the xy plane of the confocal volume a spot at the top of the vesicle is picked for a measurement (*a* in **Fig. 3.29**). The spot is chosen according to a cross-sectional scan of the GUV. The resulting correlation curve is analyzed by means of the two-dimensional fit model for one diffusing species with an included triplet population.
An exemplary FCS curve is shown in **Fig. 3.29** as well, where a point measurement from the inside of the vesicle (*b*) is compared to a point measurement within the membrane at the top of the DOPC vesicle (*a*).

Typically, a measurement was conducted for 120 s to give rise to an enhanced statistic. This supports to get smooth curves upon correlation of the intensity curves. In the normalized representation in **Fig. 3.29** the curves are normalized to their diffusion share highlighting the pronounced differences in the diffusion timescales. Within the membrane the diffusion time is more than an order of magnitude longer than inside the vesicle where most likely small accumulations of dye are present. Due to the logarithmic scale on the x-axis the difference is distinct visible even without a quantitative analysis.

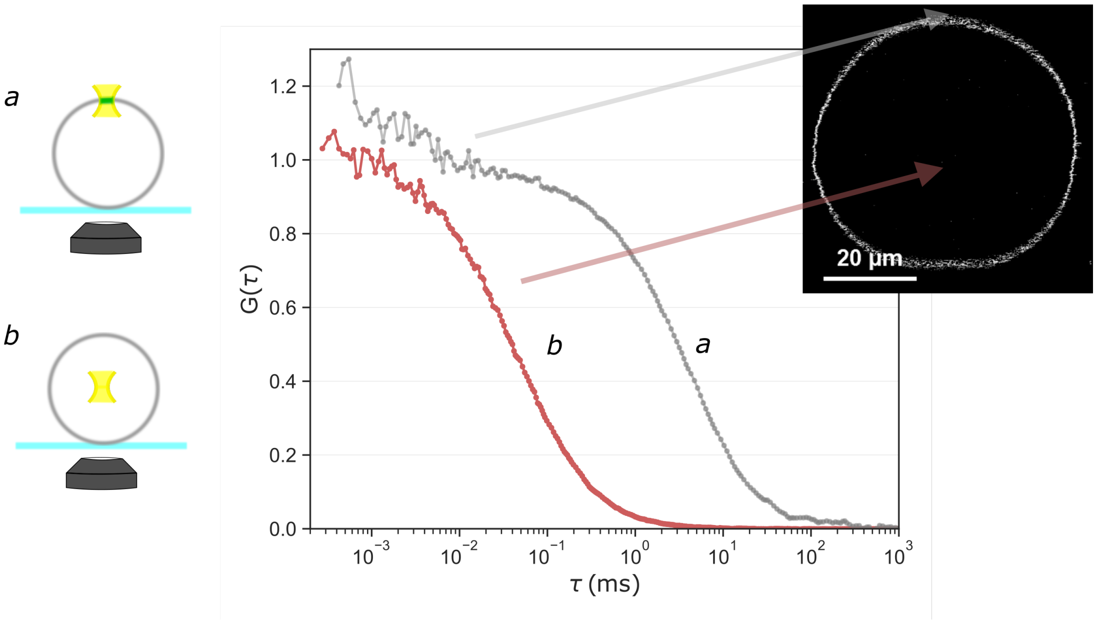

Fig. 3.29.: Comparison of normalized FCS curves from the membrane of a DOPC GUV (*a*) and from the inside of the GUV where dye accumulations are present (*b*).

Upon analyzing the correlation curve of dye inside the vesicle (*b*) with a three-dimensional model of one diffusing species and the curve from the membrane (*a*) with a two-dimensional model for one lateral diffusing species and a triplet share, this results in:

$$(a) \quad D_{\mathrm{memb}} = (5.4 \pm 0.8)\,\frac{\mu\mathrm{m}^2}{\mathrm{s}}$$

$$(b) \quad D_{\mathrm{inside}} = (285 \pm 1)\,\frac{\mu\mathrm{m}^2}{\mathrm{s}}$$

The diffusion coefficients differ between two orders of magnitudes. This behavior is expected and simultaneously underlines the plausibility of this method. The timescale of the dye inside the GUV resembles the order of magnitude of *free* dye and the diffusion coefficient of the DOPC membrane is close to results on GUVs in their fluid phase presented in the literature ($D \sim 3\,\frac{\mu\mathrm{m}^2}{\mathrm{s}}$[DLPC]) [73]. Additionally, the number of molecules N is close to 1 in all measurements on the membrane. Thus, in average, there is one dye molecule in the focus which is the desired concentration for these type of measurements and allows the tracking of a single lipid-dye complex.

From that, the method is expanded to temperature dependent measurements with the lipid DMPC since DOPC ($T_m = -17\,°\mathrm{C}$) is not suited for inducing a phase transition by temperature. DMPC GUVs ($T_m = 24\,°\mathrm{C}$ [55]) are formed, bound to the glass via the biotin-neutravidin binding and measured upon temperature variation. Not more than four temperatures are compared as to difficulties in the handling of the GUVs during the temperature variations.

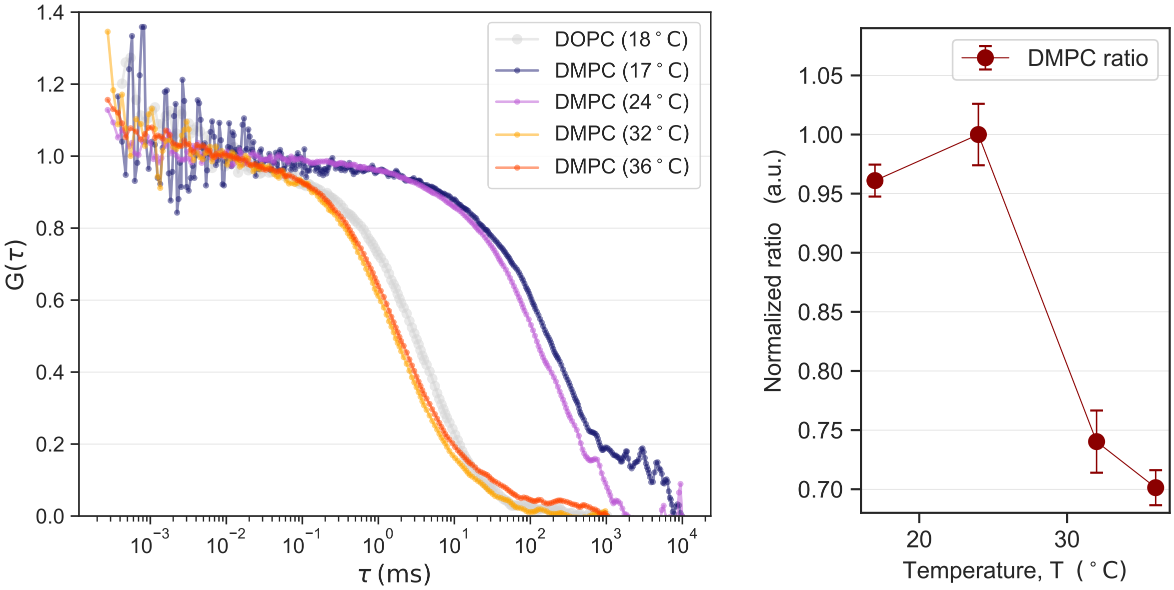

FIG. 3.30.: Results on DMPC GUVs upon temperature variation: *Left* - Exemplary correlation curves measured on DMPC GUVs at different temperatures compared to DOPC GUVs at room temperature. The DOPC curve aligns with curves measured in DMPC GUVs at $T \geq 32\,°\mathrm{C}$. For $T \leq 24\,°\mathrm{C}$ the timescales are drastically increased. *Right*: Temperature dependent, normalized ratio parameter of the dye emission embedded in DMPC GUVs. The shift between 24 °C and 32 °C demonstrates the occurring phase transition between these temperatures. Note, the ratios are normalized as a different combination of bandpass filters was used compared to the SUV measurements presented in section 3.2.3.

The ratio parameter in **Fig. 3.30** reveals the transition between the phase states. The ordered phase is induced for $T \leq 24\,°\mathrm{C}$ as a significant increase in the ratio happens between $T = 32\,°\mathrm{C}$ and $T = 24\,°\mathrm{C}$. This conclusion is based on the characterization of the ratio parameter as state variable in section 3.2.3 and aligns with the expected transition temperature of DMPC lipids around 24 °C.

The normalized correlation curves for the individual temperatures in **Fig. 3.30** reveal a pronounced shift in their timescales between $T \leq 24\,°\mathrm{C}$ and $T \geq 32\,°\mathrm{C}$ accordingly. For comparison reasons a DOPC correlation curve - recorded at $T = 18\,°\mathrm{C}$, where the DOPC membrane is in a liquid disordered phase - is added as well (grey dots). The DOPC curve aligns with the DMPC curves in the disordered phase ($T \geq 32\,°\mathrm{C}$) demonstrating that the shift in the curves is solely caused by a variation in phase state and **not** by temperature. Note, the correlation curves in **Fig. 3.30** are representative examples. At all temperatures points, curves were measured repeatedly ($n > 10$).

Upon fitting the curves derived on DMPC GUVs, diffusion times in the order of $\tau_D \approx 200\,\mathrm{ms}$ for the disordered and $\tau_D \approx 2\,\mathrm{ms}$ for the ordered phase are extracted. This results to following diffusion coefficients:

$$T \leq 24\,°\mathrm{C}: \quad D_{\mathrm{ordered}} \approx 0.08\,\frac{\mu\mathrm{m}^2}{\mathrm{s}}$$

$$T \geq 32\,°\mathrm{C}: \quad D_{\mathrm{disordered}} \approx 8\,\frac{\mu\mathrm{m}^2}{\mathrm{s}}$$

In conclusion, the diffusion coefficients differ by two orders of magnitude between the ordered and disordered phase state. The absolute values for the different phase states, as well as the dimension of the shift in between the phases, align quite well with results from literature [73]. So far, state diagrams of GUVS have been mainly investigated by changing the lipid composition at a constant temperature, though.

Fluorescence scans in **Fig. 3.31** show the deformation of DMPC GUVs upon cooling. Most GUVs do not survive the cooling/heating process as they burst. By that, it is not possible to keep track of one vesicle over the whole measurement series. To compensate for that and gain statistic, several curves ($n > 10$) were recorded at one temperature.
To underline the results, pure DPPC GUVs ($T_m = 41\,°\mathrm{C}$ [74]) were produced as well and measured at room temperature where they are in the ordered phase state. As the vesicles are rather deformed and small (at room temperature), measurements were challenging. However, the derived timescales were similar to the diffusion coefficients in DMPC GUVs at room temperature (data not shown).

In general, the diffusion constant within GUVs of one lipid type reveals a pronounced phase dependency as D strongly follows the phase state and the effect of the temperature is negligible. That becomes apparent upon comparing:

$$D_{\mathrm{DMPC}}(17\,^{\circ}\mathrm{C}) \ll D_{\mathrm{DOPC}}(18\,^{\circ}\mathrm{C}) \approx D_{\mathrm{DMPC}}(32\,^{\circ}\mathrm{C})$$

In summary, similar results are yielded, whether the phase transition is induced by temperature or upon comparing different lipid types at room temperature, that are in distinguished phase states. A further discussion of the results follows after the presentation of the results on the monolayer.

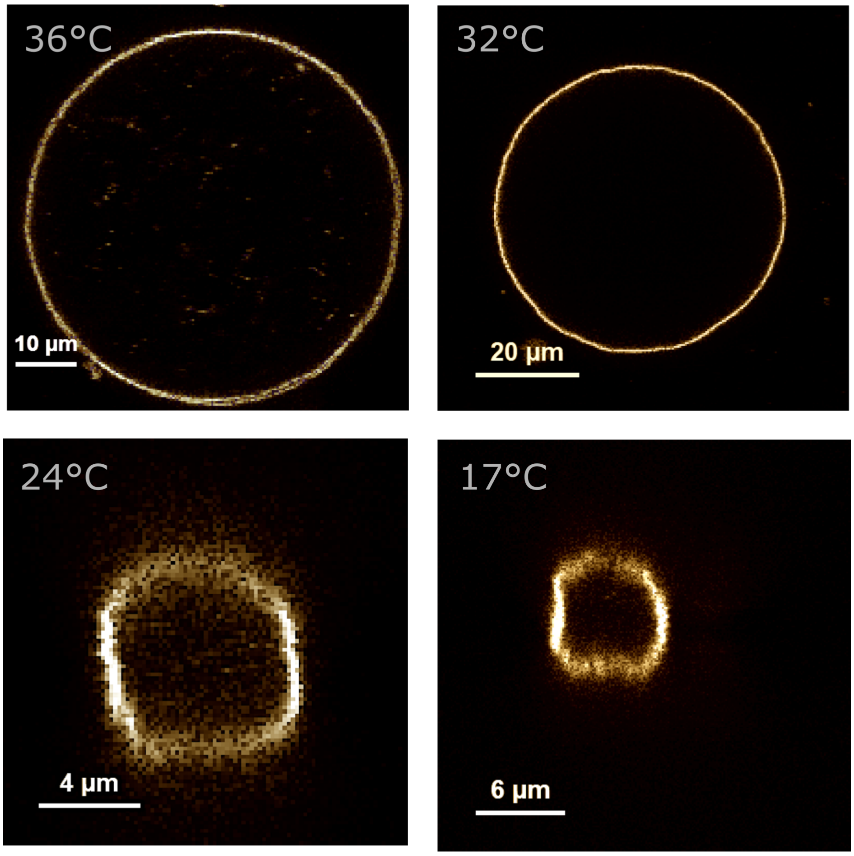

FIG. 3.31.: Fluorescence scans of DMPC GUVs at different temperatures. Usually, starting at $T = 36\,^{\circ}\mathrm{C}$ the GUVs are cooled and reveal deformation effects as they get smaller and a more coarse surface.

DIFFUSION IN LIPID MONOLAYER

Measurements are conducted similar as described before in section 3.2.4 for the thermodynamical characterization of the monolayer system in the fluorescence setup. The here presented results are extracted from point measurements at different lateral pressures. The pressures were set via stopping an isotherm at a given pressure level and measure the emission intensity for up to 120 s.

The specialty here concerning the method of correlation spectroscopy, is the detection of correlation curves via air. In the literature, the approach takes place exclusively via the aqueous subphase. By that, immersion objectives can be used, but the working distance of the objectives are very small compared to the dimensions of the subphase or rather the trough. Challenging setups or modified chambers are required in order to reduce the height level of the monolayer. A reduction of the amount of subphase would be needed such that the monolayer has an intersection plane with the confocal volume.

The here presented approach using the objective converter is not less challenging but the original and unmodified setup including the Langmuir trough can be used by that. As mentioned before, an air objective is required (40X, NA = 0.65, WD = 0.6 mm, PLCN40X, Olympus) which has not as advanced optical parameters as the otherwise applied immersion objective. It has a larger focus volume and a lower numerical aperture. For measurements of ratio and lifetime the impacts are negligible but there is an influence on the quality of the correlation measurements expected.

Exemplary FCS curves are recorded on a DPPC monolayer at four different lateral pressures (**Fig. 3.32**). From the associated isotherm (not shown) it can be estimated that the layer is in its LE phase at $\pi = 4\,\frac{\mathrm{mN}}{\mathrm{m}}$ and in its LC phase at at $\pi = 16\,\frac{\mathrm{mN}}{\mathrm{m}}$. In between, ($\pi = 6\,\frac{\mathrm{mN}}{\mathrm{m}}$ and $\pi = 10\,\frac{\mathrm{mN}}{\mathrm{m}}$) the transition regime is present. In the LE and the LC phase correlations can be successfully measured, but with slightly distorted shapes. However, a difference between both curves is apparent concerning their timescale. During the transition regime the curves are strongly distorted compared to *normal* correlation curves where diffusion is the dominating process.

For analysis, a two-dimensional model is chosen considering one diffusing species and a triplet state. Upon analysis of the curves outside the transition regime a difference in τ_D of about a factor 2 is derived. The times increase from $\tau_D \approx 12\,\mathrm{ms}$ (LE) to $\tau_D \approx 25\,\mathrm{ms}$ (LC) which is a reasonable result due to the structural changes in the phase states. A reference measurement of the 40X objective coupled to the objective converter yields the new focus parameter $\omega_1 = 0.502\,\mu\mathrm{m}$.

With that, following diffusion coefficients are obtained:

$$D_{\mathrm{LE}} = (5.2 \pm 2.2)\,\frac{\mu\mathrm{m}^2}{\mathrm{s}}$$
$$D_{\mathrm{LC}} = (2.5 \pm 0.4)\,\frac{\mu\mathrm{m}^2}{\mathrm{s}}$$

Relative errors up to 40 % are most likely a consequence of the slopes of the correlation curves. They rather resembling correlation curves with underlying active transport [69]. This occurs if the whole layer is moving influencing the measured dynamics. Additionally, a periodicity towards longer lag times is apparent and most likely originates in surface effects such as undulations or capillary waves, which are expected to occur around 10 Hz. Nevertheless, the overall shift between the phase states is apparent as it is already visible, prior to the analysis, in the position of the correlation curves.

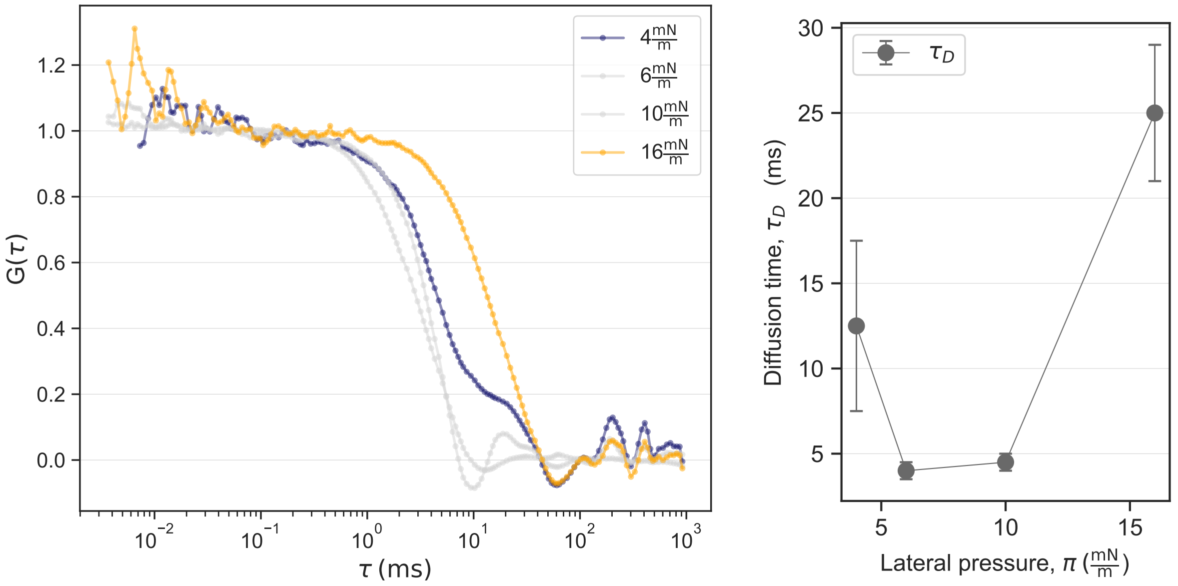

FIG. 3.32.: Left: Correlation curves on the DPPC monolayer at the air-water interface. At $\pi = 4\,\frac{\mathrm{mN}}{\mathrm{m}}$ (blue) the LE phase is represented and at $\pi = 16\,\frac{\mathrm{mN}}{\mathrm{m}}$ (yellow) the LC phase. Due to strong, state-dependent fluctuations in the underlying intensity traces (refer to section 3.2.4 or **Fig. 3.33**), the curves at $\pi = 6\,\frac{\mathrm{mN}}{\mathrm{m}}$ and $\pi = 10\,\frac{\mathrm{mN}}{\mathrm{m}}$ cannot be properly analyzed according to the diffusion times. At these pressures points the DPPC monolayer is in its transition regime and the intensities are dominated by these fluctuations. The curves are both shown in grey as to their reduced informative value. Right: Extracted diffusion times from the FCS curves on the left. Reasonable values are derived for the LE and LC state. In the transition regime ($\pi = 6\,\frac{\mathrm{mN}}{\mathrm{m}}$ and $\pi = 10\,\frac{\mathrm{mN}}{\mathrm{m}}$) the times are decreased as the diffusion times are most likely not correctly identified within the model. The times rather resemble timescales of the fluctuations.

At $\pi = 6\,\frac{\mathrm{mN}}{\mathrm{m}}$ and $\pi = 10\,\frac{\mathrm{mN}}{\mathrm{m}}$, within the transition regime, the curves cannot be analyzed by the known models as the shapes do not fit an ordinary model anymore (grey curves in **Fig. 3.32**). If a fit is forced onto the curve to estimate the timescales they are smaller compared to τ_D at $\pi = 4\,\frac{\mathrm{mN}}{\mathrm{m}}$ and $\pi = 16\,\frac{\mathrm{mN}}{\mathrm{m}}$. This is already visible without calculation in **Fig. 3.32** for the comparison of all curves.

The reason becomes apparent in the intensity traces of the individual measurements in **Fig. 3.33**. As already discussed in section 3.2.4 intensity fluctuations appear during the transition regime. The single *dips* or *bursts* dominate the signal and their width is most likely the basis for the autocorrelation signal. This leads to *diffusion* times around 5 ms rather describing *opening times*. Hence, an analysis of the curves recorded in the plateau region is not fruitful. Similar results are known from literature as there has no successful measurement of diffusion directly in the transition regime of a monolayer been reported yet [65].

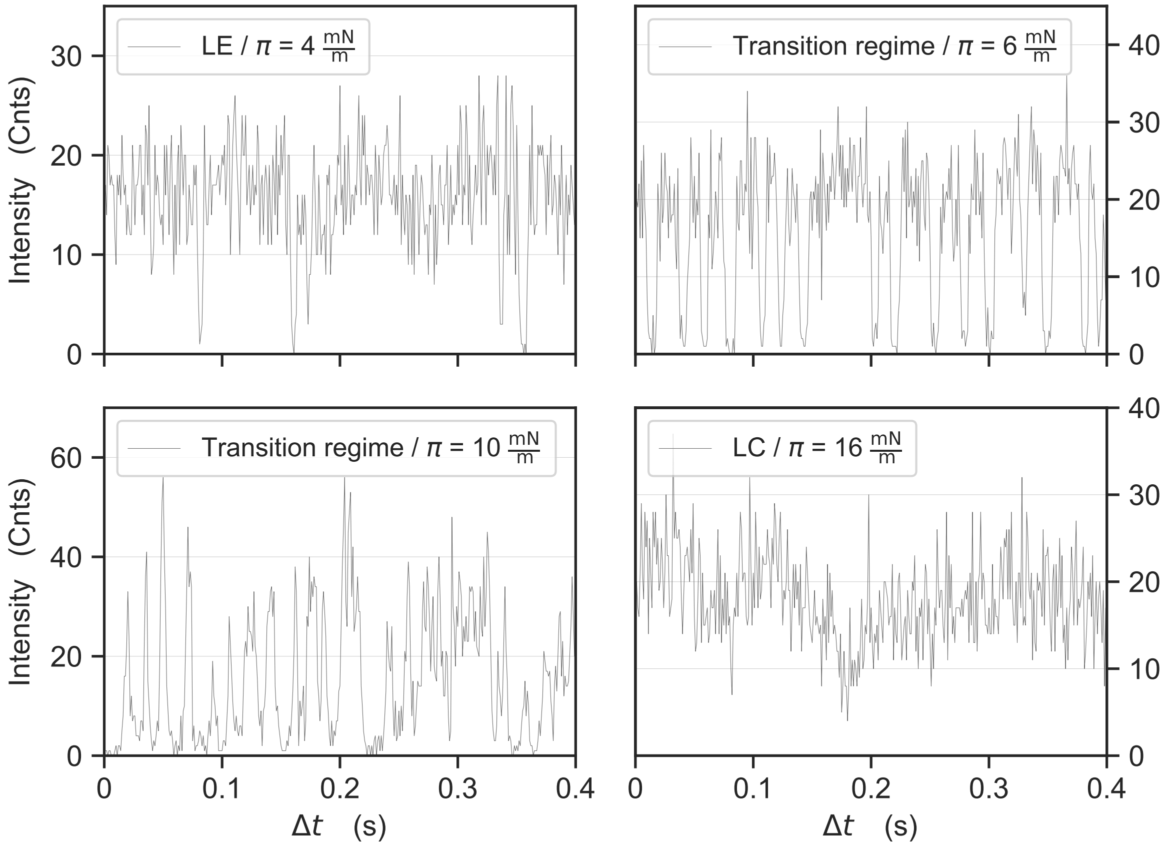

FIG. 3.33.: Excerpts of the intensity traces on which the calculation of the correlation curves is based. The fluorescence intensity represents signal in the $\lambda = 520\,\mathrm{nm}$ channel.

Consistent results were obtained with another dye (*abberior STAR 635 DOPE*) in similar monolayer measurements conducted in the lab of Prof. Dr. Widengren at KTH Stockholm (see **Fig. 3.34**). There, the measurement principle was similar to that extent that correlation curves were measured via air at a DPPC monolayer. An upright microscope setting was used and no objective converter needed. The monolayer was measured in a petri dish with a different dye as to the excitation at 595 nm. Nevertheless, correlation curves for the LE ($\pi = 2.4\,\frac{\mathrm{mN}}{\mathrm{m}}$) and LC ($\pi = 15.5\,\frac{\mathrm{mN}}{\mathrm{m}}$) state could be measured and analyzed. In between the phase states, in the transition regime, the curves were dominated by intensity fluctuations as well. Overall, the detected shift confirms the results displayed in **Fig. 3.32**.
Note, the curves contain an increased level of noise. Due to the given conditions of evaporation and present instabilities of the layer (movement, perturbation etc.) the measurement times must kept short. To reduce the noise it is a sound approach to average over several correlated curves derived from short intensity traces (10 s). By that the noise can be reduced, which has been done in the presented curves in **Fig. 3.34**.

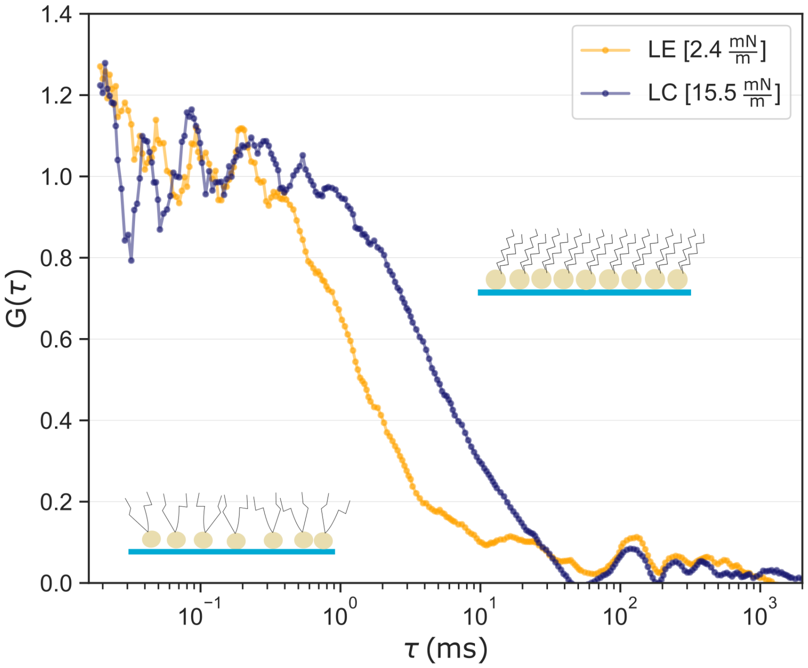

FIG. 3.34.: Correlation curves measured on a DPPC monolayer prepared in a petri dish. A curve recorded in the LE phase ($\pi = 2.4\,\frac{\mathrm{mN}}{\mathrm{m}}$) is set against an exemplary curve recorded in the LC phase ($\pi = 15.5\,\frac{\mathrm{mN}}{\mathrm{m}}$). The according experiment was conducted in the lab of Prof. Dr. Widengren at KTH Stockholm during a research stay.

SUMMARY AND DISCUSSION

Diffusion times could be successfully identified state-dependently within different lipid systems. In giant unilamellar vesicles (GUVs) of DMPC lipids diffusion coefficients vary up to two orders of magnitude between phase states. The phase shift was induced by temperature variation. Additionally, a comparison between lipid types residing in distinguished phase states at room temperature (DOPC, DMPC, DPPC) yields similar variations in the diffusion coefficients. By that, a temperature effect can be excluded. As already stated, these timescales and their shift between phase states are in agreement with other reported findings on GUVs [73].

In the DPPC monolayer a significant shift between liquid expanded (LE) and liquid condensed (LC) phase could be visualized accordingly. The overall change in timescales in the monolayer is not as pronounced as the phase dependency revealed in GUV measurements. However, it cannot be entirely ruled out, that the autocorrelation curves contain an additional small portion of a longer timescale as it is not resolvable due to an inconvenient signal to noise ratio.

In principle, difficulties for measuring diffusion coefficients in the LC phase or in the transition regime of a DPPC monolayer via FCS has been reported before as the measurement is experimentally challenging and correlation curves reveal altered shapes [65]. As a possible cause the state-dependent fluctuations in the intensity trace dominating the correlation curves could be identified here.

Studies on lipid monolayers measured above their critical temperature reveal a linear relation of τ_D and A with a factor 2-3 between the minimal and maximal τ_D [65, 75]. These isotherms do not have a plateau as there is no phase transition inducible. In the study of Kinnunen et.al. ([75]) a phase transition is induced by mixing cholesterol, sphingomyelin and POPC on a monolayer. A nonlinear, sigmoidal shaped course of the extracted diffusion times around the transition was found. The diffusion times increased by less than an order of magnitude (factor ≈ 5) in the LC phase compared to the LE phase.

A direct comparison between the results on lipid monolayers and GUVs is not straightforwardly possible. This seems to apply in general as there exists a great variety of diffusion coefficients reported for lipids within the disordered phase alone. Results clearly depend on the system at hand (GUV, monolayer, supported bilayer) and the detection method [65, 76, 77].

In fluorescence measurements dyes might favor a certain phase state for embedding and thus not represent both phase states properly leading to inconsistent results [65]. It has been found that different types of lipid anchors lead to altered diffusion times as well [70].

Thus, the question whether the diffusion coefficient changes in order of magnitudes or less upon crossing the main phase transition remains unclear and cannot be answered unambiguously by consulting the literature.

Another point of view is introduced by a study using NMR instead of fluorescence on DPPC vesicles [76]. There, it is indicated, that - beside a comparably small shift of τ_D at the main transition - the more prominent shift happens within the ordered phase alone. The origin might be the existence of another, higher ordered phase.
In lipid monolayers, there exists a higher ordered phase as well, the solid phase. Additionally, it is well known that the viscosity of -PC monolayers rises for relatively high lateral pressures above the main transition pressure. A general coupling between diffusion and viscosity is reasonable as to the general definition of the diffusion coefficient (equation 3.29). This hypothesis was stated and measured on lipid bilayers before [78].
Interestingly, for DPPC monolayers a significant increase in viscosity is measurable for lateral pressures $> 30\,\frac{\mathrm{mN}}{\mathrm{m}}$ whereas the main transition happens at $\approx 8\,\frac{\mathrm{mN}}{\mathrm{m}}$ (depending on the temperature) [79]. Transferring this line of arguments to the here measured DPPC monolayer, a stronger variation of diffusion times would have been expected merely for pressures above $\approx 30\,\frac{\mathrm{mN}}{\mathrm{m}}$.

In summary, diffusion times could be state-dependently measured on different lipid systems. The diffusion coefficients are consistently slower in the ordered phase states than in the disordered states which is reasonable considering the associated structural variations. The influence of temperature variations, that are expected due to equation 3.29 is negligible compared to the significant phase-associated shift. However, the effect of viscosity alterations cannot be determined on the basis of the measurements.

3.3.3. LOCAL PROTONATION DYNAMICS ON THE MEMBRANE SURFACE

Protonation kinetics are investigated in the following. They are exemplary for processes inflicting blinking rates in the fluorescence emission signal. The *proton collecting antenna* effect is investigated and compared for two phase states of lipids.

The protonation of molecules, membranes and interfaces in general is modulated via the ionization constant (pK) of a chemical bond. It determines whether it is protonated or deprotonated at a given pH. The pK is similar to a phase transition point between these two forms. Protonation is an omnipresent process happening at lipid interfaces and cellular membranes.

In living systems, enzymes are present that produce free protons during reactions and induce local pH changes within the cell [33]. In turn, they can affect the protonation state of molecules which can introduce a perturbation or even a local phase transition depending on the local pK. Impacts of pH changes are manifold and have been discussed in section 2.2.4.Potential protonation pathways in the cell include either direct protonation from the bulk or along the membrane. The transfer along the membrane is faster than the proton exchange via the bulk [80]. In general, a more efficient diffusion of protons along the membrane is proposed as there are no dissipations into the bulk.

PROTON COLLECTING ANTENNA

The proton collecting antenna effect demonstrates that the pK of a molecule is dependent on its environment as the protonation pathways vary [81, 82, 83]. It tells that the pK of molecules increases when embedded into a lipid membrane, compared to the freely dissolved molecule. This has been demonstrated for pH-sensitive fluorophores such as *fluorescein*. The underlying effect is a change in protonation pathways. When the molecule is located in the membrane the proton uptake happens via transfer along the membrane at low proton concentrations. By that, the proton uptake is accelerated compared to the uptake from the bulk (respectively a molecule in the bulk). The protonation along the membrane is dominating for low proton concentrations. For increasing proton concentrations the dynamics change and at some pH the molecule in the layer is protonated directly from the bulk similar to a molecule dissolved in the bulk.

This effect is exemplary for a process in the cell dependent on the membrane. It is a nearby assumption that also the membrane state will influence the protonation kinetics.

This phenomenon should be mirrored in protonation rates. They are measurable with the FCS setup and can be extracted from the correlation curves. This requires a protonation sensitive dye such as *fluorescein*.

FLUORESCEIN DHPE

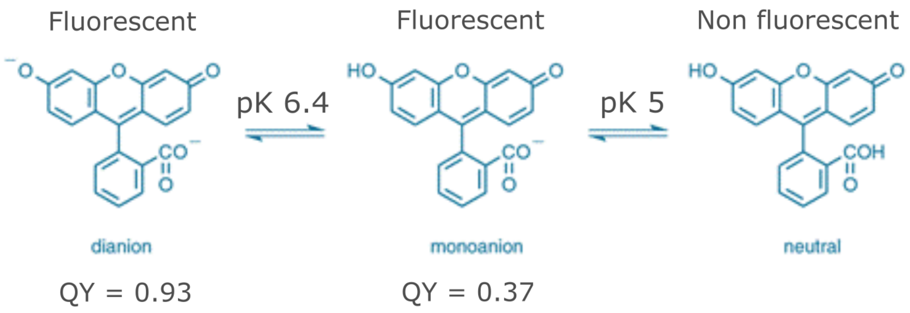

FIG. 3.35.: Overview of the most common protonation forms of the *fluorescein* molecule. The free dye as well as the conjugated form (*Fl -DHPE*) have pKs at ≈ pH 6.4 for the transition from the dianion to the anion and ≈ pH 5 for the subsequent transition into the neutral state. Figure edited and taken from [84].

The neutral form of *fluorescein* is nonfluorescent but upon increasing the pH (> 5) a proton is emitted from the carboxylic acid (**Fig. 3.35**). This intermediate monoanion form is weakly fluorescent (quantum yield 0.37) and the dianion (pK ≈ 6.4) is highly fluorescent (quantum yield 0.93) [84]. This given characteristic makes the dye well suited for protonation kinetic measurements in the FCS as it changes between a fluorescent *on* and *off* state (with rates k_{-1} and k_{+1}) correlating with its protonated state

$$\textbf{not protonated} \underset{k_{-1}}{\overset{k_{+1}[\mathrm{H}^+]}{\rightleftharpoons}} \textbf{protonated}$$

with the overall protonation rate:

$$k_{\text{prot}} = k_{-1} + [H^+]k_{+1}$$

The effect originates in a shift of the excitation spectrum such that the dye is not (likely) excitable anymore. This *blinking* mechanism is resolvable in rates within the correlation curves similar to the already introduced triplet state. The rate is the inverse of the measurable relaxation time $\tau_P = \frac{1}{k_{\text{prot}}}$.This holds for non-buffered aqueous solutions. Otherwise a more complex model for the kinetics must be applied.

From the proton collecting antenna effect it is expected that the protonation rate of the dye is not proportional to the proton concentration [H$^+$] over the whole pH range. Consequently, the pK is shifted [82]:

$$\mathrm{pK} = -\log\left(\frac{k_{-1}}{k_{+1}}\right) \tag{3.30}$$

For *fluorescein* a shift of approximately 2 pH units in the membrane compared to pK ≈ 6.4 in bulk when embedded in a DOPC bilayer is expected [83].

MEASUREMENT DETAILS

The dye is embedded into lipid bilayers (SUVs) via the lipid anchor DHPE. The anchor has no effect on the protonation dynamics of *fluorescein* [83]. The concentration is chosen as to that one SUV contains in average one dye molecule (vesicle solution: 0.001 mol% dye for 2 mM lipids). Measurements take place in water and the pH is adjusted directly beforehand by adding NaOH or respectively HCl. Since the pH solution is not buffered it is necessary to use it directly after preparation. For each point measurement a new solution is prepared in chambered coverslips with 8 wells (μ-Slide; Ibidi). Directly before, 2 μl of the vesicle solution are diluted in a well filled with 400 μl of the adjusted pH solution. At each set pH value 3-4 wells are prepared and measured. As to the low emission intensity for low pH values where the protonated ($\widehat{=}$ nonfluorescent) form dominates the intensity traces are recorded for 240 s each.

The previously introduced general model considering triplet and diffusion within the system is expanded taking the protonation rate into account. The protonation reflects a *blinking* rate and a combined term including protonation and triplet is added [85]:

$$G(\tau) = \frac{1}{(1-P-T)} G_D(\tau) \left(1 - P - T + P\mathrm{e}^{-\frac{\tau}{\tau_P}} + T\mathrm{e}^{-\frac{\tau}{\tau_T}}\right) + 1 \tag{3.31}$$

For diffusion the three-dimensional model of $G(\tau)$ is applied as the diffusion of SUVs ($d < 70\,\mathrm{nm}$) in the focus volume ($V \approx 1\,\mathrm{fl}$) is detected. The diffusion of the lipids within the SUV membrane is not resolvable.

RESULTS

Correlation curves recorded during a protonation series of DOPC ($T_m = -17\,°\mathrm{C}$ and pK ≈ 2 [72]) are presented in **Fig. 3.36**. For comparison reasons they are normalized to 1 μs. By that, the triplet timescale ($\tau_T \approx 1.5\,\mu$s) is practically excluded and changes in the protonation timescale ($\tau_p > 10\,\mu$s) become directly visible.

The protonation is typically in the range of $\tau_P = 10 - 60\,\mu$s which is an order of magnitude slower than τ_T and faster than τ_D of a SUV. The protonation rate k_{prot} decreases with increasing pH which is mirrored in an increase of τ_P. The shift appears in the width of the curves and is rather distinct than continuous (**Fig. 3.36**). During the measurement between pH 5.5 and pH 10, the pK of the dye is crossed and a nonlinear behavior of the protonation rate apparent. For low pH values the curves get noisier as the emission intensity decreases.

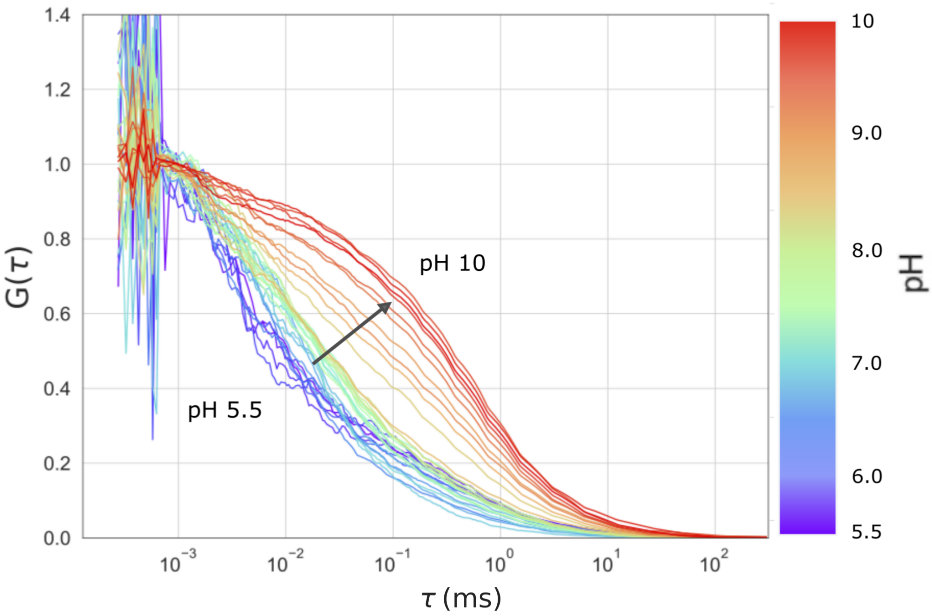

FIG. 3.36.: Normalized correlation curves of DOPC SUV suspensions under variation of the pH. Protonation takes place at timescales around $10 - 60\,\mu$s. In that region a shift in the width of the curves is apparent. At low pH values the protonation rates increase which leads to a decrease in the protonation time τ_P.

In **Fig. 3.37** the protonation rates k_{prot} derived from the analysis of the correlation curves are depicted. As the model function contains 6 fit parameter variables such as τ_T and τ_D can be fixed during the fitting process. By that, the degree of freedom is reduced and changes in τ_P are identified more efficiently. The diffusion time is independent of pH and can be determined with a high precision in a measurement yielding a good emission signal (pH 10). The triplet state is independent of pH as well and a similar approach is applied. The protonation kinetics over the pH range from 5.5 to 10 are quantified by the analysis of the correlation curves. In **Fig. 3.37** k_{prot} is presented as a function of [H$^+$]. With

$$k_{\text{prot}} = k_{-1} + [H^+]k_{+1}$$

k_{-1} and k_{+1} can be calculated by a linear regression. But, it is apparent and predicted that k_{prot} and [H$^+$] are not linearly coupled over the whole pH range due to the proton collecting antenna effect. At pH $\approx$ 8 there is a break in the linearity and the accelerating effect of the membrane becomes visible as k_{+1} is increased for pH > 8.

The crucial range for the observation of the proton collection antenna effect is between pH 8 and 10 and the new pK can be derived by:

$$\mathrm{p}K = -\log\left(\frac{k_{-1}}{k_{+1}}\right)$$

With that, pK = 7.8 ± 0.2 is determined for *Fl DHPE* in DOPC SUVs and the antenna effect could be proven here. This shift in pK is in the order of magnitude that is expected from the literature.

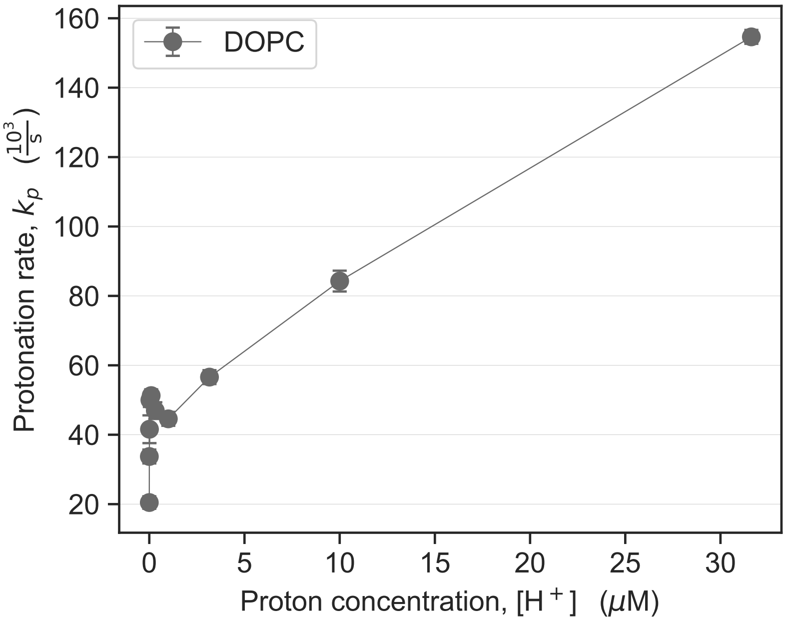

FIG. 3.37.: Protonation rates k_{prot} of *Fl DHPE* in DOPC SUVs under variation of the proton concentration. Linear representation of the proton concentration $[\mathrm{H}^+]$ revealing the nonlinear coupling of τ_P. More precisely, two linear sections are apparent each with a constant, but different slope k_{+1} accordingly to the proton collecting antenna effect.

A similar measurement series with DMPC yields a shift in the pK as well but with $\mathrm{p}K = 7.0 \pm 0.2$ it is smaller than for DOPC. A significant difference between DMPC and DOPC lies in their transition temperature. In contrast to DOPC, the transition temperature of DMPC is above the room temperature and consequently the lipids are in their ordered state during the measurement. The pK demonstrates that the effect is more pronounced for DOPC as:

$$\mathrm{pK}_{\mathrm{DOPC}} = 7.8 > \mathrm{pK}_{\mathrm{DMPC}} = 7.0$$

The accelerating effect of the membrane is more pronounced within DOPC SUVs which is mirrored in the increased k_{+1} compared to DMPC (refer to **Fig. 3.38**). From these results it is implied, that the transport of the protons along the membrane is more efficient when the membrane is in its fluid phase.

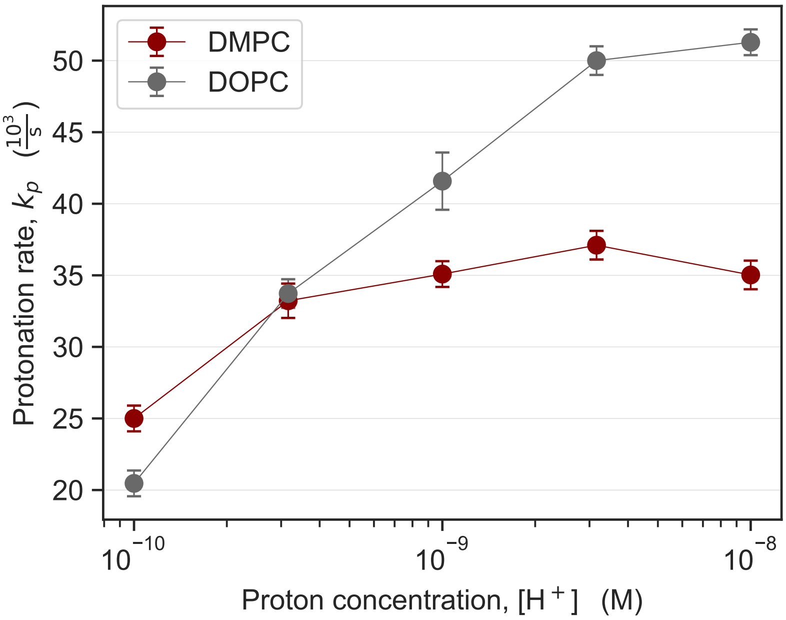

FIG. 3.38.: Comparison of protonation rates k_{prot} for *Fl DHPE* in DOPC and DMPC SUVs. Range of pH 8-10 is shown where the proton collecting antenna effect dominates. The effect is more pronounced for the DOPC SUVs as the slope k_{+1} is increased compared to DMPC SUVs.

The observed behavior describes on one side purely the phase behavior of the dye as its state of protonation is directly monitored. But, on the other hand the membrane has clearly an effect on the incorporated dye by shifting its pK. The dye itself can stand for practically every protonable bound of a molecule or protein embedded within a lipid bilayer. So far, it has been reported that ion concentrations additionally influence the point of the pK and for charged (DOPG) or zwitterionic (DOPC) lipids the absolute protonation rates differ strongly. On the other hand, they shift the pK in a similar manner in their fluid phase [83]. Here, the comparison between two zwitterionic lipids (both -PC) in different phase states yields that the absolute protonation rates are in a similar order of magnitudes but they act differently on the pK of the dye.

4. DETECTION OF PHASE TRANSITIONS IN NEURONAL CELLS

In the following the transfer from model systems, pure lipid membranes, to living systems, cellular membranes, is administered. Artificial, lipid membranes are advantageous in terms of their relatively simple handling and accessibility for measurements. On the other hand, the validity of the results measured on lipid interfaces is limited regarding to *real* living cells where not only lipids are present within the membrane but proteins and carbohydrates as well. Additionally, the lipid compositions are mixtures of lipid types including zwitterionic and negatively charged phospholipids at physiological conditions and cholesterol.

The fact that lipids undergo phase transitions is commonly interpreted as an indicator for the existence of transitions in lipid-based cellular membranes. On the other hand, the presence of a relatively high amount of cholesterol (25 % - 35 % in neuronal membranes [refer to table 2.1]) has often been put forward to reject this hypothesis as this can lead to a disappearance of the phase transition in lipid membranes [21, 27]. Further, the presence of various lipid types with individual transition points/melting temperatures is believed to prevent a cooperative transition in a cellular membrane. Nevertheless, hints of cooperative and nonlinear material behavior of cells, interpreted as phase transitions, haven been detected in different cellular systems already [11, 14, 15].

In general, predictions of the behavior of the complex system - the cellular membrane - is not reliably possible as it cannot be mimicked easily and measurements on living systems themselves are necessary. The previously introduced methodology is straightforwardly applied to neuronal cells in the following. These excitable cells have not been investigated regarding their physical states so far.

4.1. DESIGN OF CELL EXPERIMENTS

The cell measurements are conducted on the cell line *SH-SY5Y*. It is an established neuronal cell line of human origin. For fluorescence measurements the cells are stained with the previously introduced dye *Atto488 DPPE* due to its phase sensitive properties. For further details concerning culturing and staining of the cells refer to A.1 in the Appendix.

Within the confocal system (introduced in section 3.2.2) it is not only possible to measure on a single cell level but to also to determine the location within the cell since a single cell is spatially resolvable. The dimension of a typical cell is $\sim 100\,\mu\mathrm{m}^2$ in the xy plane whereas the focus area is $\sim 1\,\mu\mathrm{m}^2$ in that plane.

Figure 4.1 demonstrates the distribution of the dye (brightness relates to intensity of the fluorescence emission signal) when integrated into different systems. In **Fig. 4.1** (**C**) a cross-sectional scan of a single *SH-SY5Y* cell stained with *Atto488 DPPE* demonstrates the predominant accumulation of dye within the outer cell membrane. Analogous to experiments on pure lipid systems the lipid-coupled dye embeds itself within the lipid framework of the membrane due to its lipid anchor. This is also visible in **Fig. 4.1** (**A**) and (**C**) where cross-sectional scans of a giant unilamellar vesicle (GUV) and a single cell are compared upon staining with *Atto488 DPPE*.

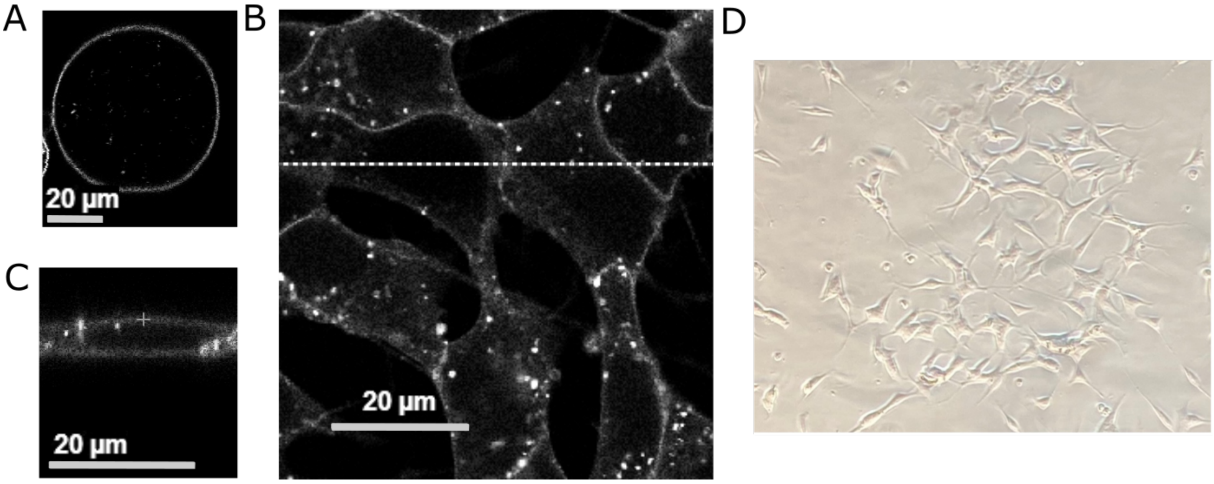

FIG. 4.1.: Confocal scans of systems stained with *Atto488 DPPE*. In the fluorescence images (A-C) the brightness relates to the emission intensity. Direct comparison of staining with the lipid-anchored dye: (A) giant unilamellar vesicle (GUV) of DOPC lipids at room temperature, (B) (mono-)layer of single cells in the xy plane (top view) and (C) cross section of a single cell recorded along the dotted line in B. The cross within the upper membrane in (C) marks an exemplary measurement spot of the optical signal. (D) shows a cell layer of *SH-S5Y5* cells in a light microscope.

Bright dots of accumulated dye within the cells appear most likely due to endocytosis. As the *living* cell has an ongoing metabolism endocytosis, the constriction of membrane vesicles into the cell, proceeds over time and will lower the amount of dye in the membrane [86, 87, 88]. Naturally, this effect increases as time goes on.

The cells are grown on a round cover glass (thickness: $\sim 150\,\mu\text{m}$). After staining of the cells, it is installed into the closable measurement chamber which has been already used for vesicle suspensions in section 3.2.3. With a 60X water immersion objective the focus area is $\sim 1\,\mu\text{m}^2$ within a $\sim 1\,\mu\text{m}$ thick plane. Inside a cross section of a single cell a point in the membrane, where the confocal volume will be located during the measurement, can be selected according to the maximized intensity in the membrane area. This principle is illustrated in **Fig. 4.2**. An exemplary selected point is visible in **Fig. 4.1** (**C**) where it is tagged with a cross. By that, the localized signal of one membrane patch can be recorded over time.

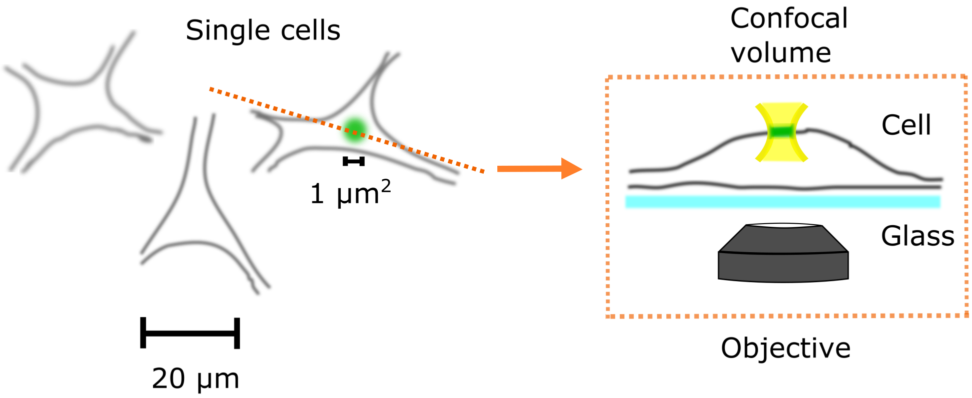

FIG. 4.2.: Scheme of the experimental design of cell measurements in the confocal system. Within a cross-sectional scan of a cell a spot for the localized measurement is identified and chosen. Additionally, the cross section yields the opportunity to check the shape of the cell regarding its fitness. A more spherical shape indicates a loss of fitness of the cell. [Fedosejevs et. al., [89]]

The underlying principle is based on the results in section 3.2.3 where a shift in the emission spectrum of *Atto488 DPPE* could be associated with a cooperative phase transition in its surrounding lipid interface. **Figure 4.3** summarizes the state-dependent positions of spectra in DMPC SUVs and shows an exemplary spectrum of a *SH-SY5Y* cell layer stained with *Atto488 DPPE* at 34 °C. This spectrum is quite similar in shape and position to the spectrum measured in DMPC in the fluid disordered phase. Especially, the maximum wavelength is nearly identical. Hence, the wavelengths for the ratio parameter (indicated with light grey hatched areas in the **Fig. 4.3**) are chosen identically to the measurements in pure lipid systems.

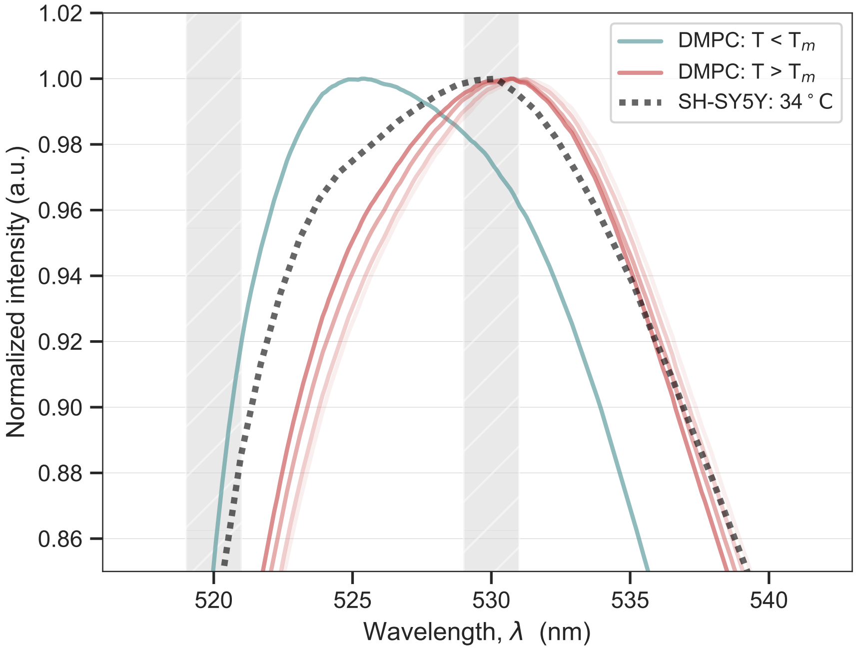

FIG. 4.3.: Emission spectrum of *Atto488 DPPE* within a *SH-SY5Y* cell layer at 37 °C compared to emission spectra in DMPC vesicles below and above T_m of DPPC. [Fedosejevs et. al., [89]]

MEASUREMENT PROCEDURE

At first, a cross-sectional scan is recorded to determine the position of the cell membrane (maximum of intensity) of a single cell. A heating bath is coupled to the measurement chamber and is programmed to vary the temperature continuously between two fixed temperatures, with a gradient of ~ 0.3 °C/min. A measurement spot is chosen in the membrane and every 1-2 minutes a data point is measured over 15 s. In between, cross-sectional scans were repeatedly recorded to assure the location of the measurement spot. To ensure the viability of the cells low laser intensities (~ 10 μW) are chosen for the excitation [67, 90, 91]. Throughout the measurements the viability of the cells was controlled by checking for morphological changes such as dislocation from the support.

4.2. SHARP TRANSITIONS WITHIN THE MEMBRANE OF NEURONAL CELLS

4.2.1. LOCALIZATION IN THE MEMBRANE

By the use of different methods the origin of the optical response can be allocated to the membrane. The location for the point measurement is chosen by a cross-sectional scan of the cell. The intensity maxima are the membranes and a point in the top membrane is set as it was described in 4.1. The length of the confocal volume is approximately 0.8 μm in z direction which is over an order of magnitude longer compared to the thickness of the membrane ($\sim$ 10 nm). Hence, in theory a signal outside of the membrane could contribute to the measured signal as well.

LIFETIMES

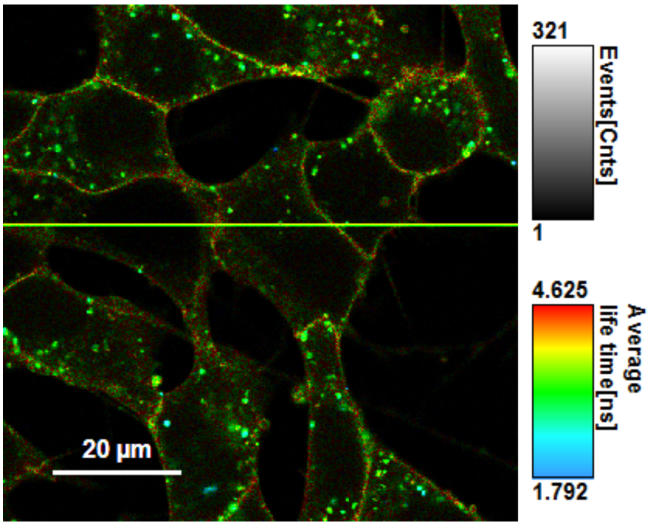

FIG. 4.4.: Fluorescence lifetime image of cells. This top view reflects lifetimes of every pixel within a color scale. Lifetimes vary from 1.8 ns (blue) to 4.6 ns (red) on a rainbow color scale. Brightness correlates to intensity. Within this range the cellular membrane appears red-yellowish whereas the endocytosed vesicles appear blue-green. The yellow, horizontal line refers to a selection of a potential cross-sectional scan.

The **F**luorescence **L**ifetime **Im**aging (FLIM) produces pixel by pixel scans within a range of 80 μm x 80 μm. Each pixel is assigned with a intensity value *and* a lifetime value. The lifetime is calculated by a TCSPC histogram containing all entries from one pixel.

Lifetimes are presented with a color scale and the intensities correlate to the brightness.

Figure 4.4 is an example of a FLIM image of cells. It becomes visible that the bright dots (green) within the cells have a different color than the stained cellular membrane (yellowish). Additionally, point measurements in the buffer solution outside the cell reveal a varied lifetime of the dye. It has been indicated before that the fluorescence lifetime of the dye can depend on its environment. Thus, by the lifetime the origin of the signal can be distinguished regarding cell, buffer and dye accumulations in the cell. Measuring inside the cell - apart from the bright accumulations - reveals a similar lifetime as the dye associated with the membrane.

DIFFUSION TIMES

The investigation of diffusion times helps with the discrimination between signal originating in and outside of the membrane. Measurement spots are exclusively chosen at the top of the cells where the membrane appears rather flat. By that, it shall be ensured that the membrane intersects the confocal volume in the xy plane allowing two-dimensional diffusion measurements.

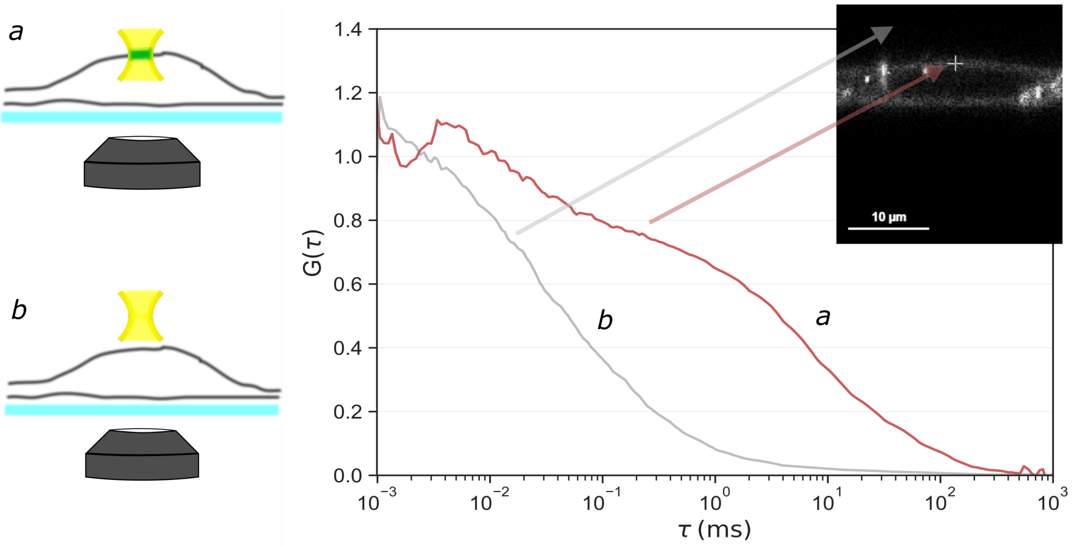

FIG. 4.5.: Comparison of normalized correlation curves for measurement spots in the buffer solution outside of the cell (*b*) and in the membrane area (*a*). Both curves reveal different order of magnitudes in their diffusion times. While the curve in *b* has a similar timescale as free, three-dimensional diffusion of the dye [$\tau_D \approx 0.1\,\mathrm{ms}$], the curve in (*a*) is in good agreement with membrane associated diffusion [$\tau_D \approx 7\,\mathrm{ms}$] [92]. [Fedosejevs et. al., [89]]

A comparison of correlation curves from measurement spots in the membrane area (maximal intensity) and outside in the buffer reveals significant differences in the diffusion timescales (refer to **Fig. 4.5**). Similar results are derived for point measurement within the cell. There, the diffusion times are significantly shorter than within the membrane area.

Hence, membrane-bound dye ($\tau_D \approx 7\,\mathrm{ms}$) and freely diffusing dye ($\tau_D \approx 0.1\,\mathrm{ms}$) can be distinguished according to their diffusion times. The derived timescales align well with membrane associated diffusion as it has been investigated in this study on pure lipid membranes and in [92] on cells. Note, *free* dye is a paraphrase here for dye that is not embedded into a membrane environment. It is not literally *free* since the lipid-dye complex is not soluble in an aqueous solution and forms most likely small micelles. An estimation of the hydrophobic radius according to the calculated diffusion coefficient ($D \approx 200\,\frac{\mu\mathrm{m}^2}{\mathrm{s}}$) and the Stokes-Einstein equation (equation 3.29) yields $R_0 \approx 1\,\mathrm{nm}$ which is in good agreement with a micelle.

Due to the dimensions of the confocal volume the signal is most likely a superposition of membrane bound and free dye signal even when the point is set into the membrane regime. However, within the analysis of the correlation curves shares of each species can be determined. By choosing a model considering two diffusing species, each can be associated with an average number of participating molecules within the measurement. An according model was already introduced in section 3.3.1. By that, it can be determined whether the signal is dominated by membrane-bound dye or not. During one point measurement TCSPC and FCS curves are recorded simultaneously and the FCS curve can directly be evaluated. Data derived from measurements where free dye dominates the signal is not considered for the analysis of the ratio parameter. Nevertheless, usually, the signal of the buffer is negligibly small.

DISTINCTION OF DYE LOCATION ACCORDING TO ITS EMISSION PROPERTIES

Combining the characteristics of both parameters, lifetime and diffusion times, a conclusive evaluation of the signals origin can be done.
The confocal volume can either overlap into the inside of the cell or into the buffer outside the cell or both. Characteristic values for τ_D (diffusion time) and $\tau_{I_{av}}$ (lifetime) in each regime are compared in **Fig. 4.6**. A clear discrimination is possible by means of these values. Note, dye accumulations within the cell are actively avoided as they would appear already in the cross-sectional scan where the location is selected. Thus, they are not considered for the analysis. If a vesicle forms during the measurement the series is aborted.

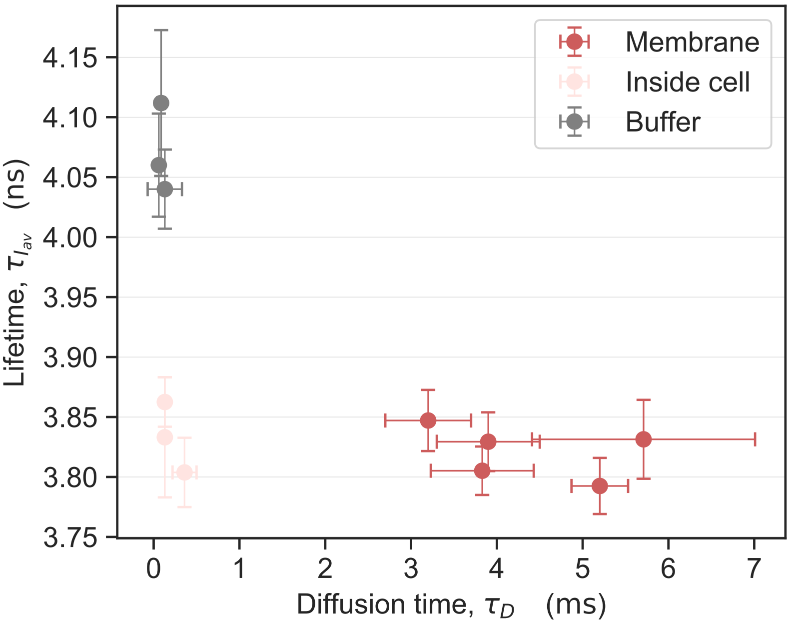

FIG. 4.6.: Comparison of lifetimes $\tau_{I_{av}}$ and diffusion times τ_D extracted from exemplary measurements. The confocal volume was either placed inside the cell, in the buffer or in the membrane area. Accordingly, three accumulations of data points become visible characteristically for each location.

DYE IN BUFFER

The optical response of pure *Atto488 DPPE* dye in cell buffer solution was checked as well. For that, a similar measurement compared to the aspired procedure of single cell measurements was conducted, without cells. *Atto488 DPPE* from a DMSO stock solution is used and diluted into the pure cell buffer solution. No significant changes over a temperature range between 15 °C and 52 °C are detected in the ratio parameter. Consequently, from the dye in buffer there is no disturbing contribution to the optical response expected.

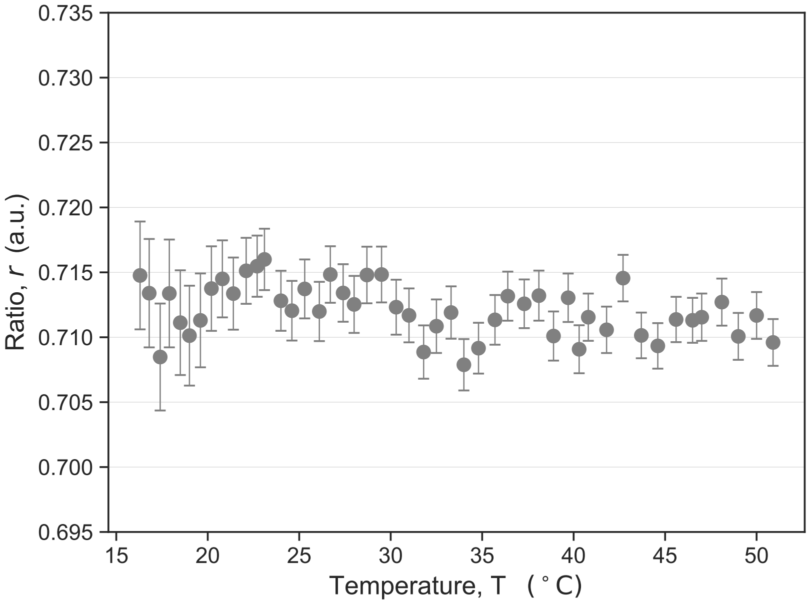

FIG. 4.7.: Reference measurement with *Atto488 DPPE* in pure buffer. [Fedosejevs et. al., [89]]

In summary, these results provide evidence that the optical signal can be clearly associated to a patch of the cellular membrane when certain values of parameters are complied. The emission from the dye in buffer has been demonstrated here to be independent of temperature variations over a wide range of temperatures. Hence, it is possible to monitor the cellular membrane and allocate potential changes in the ratiometric signal directly to membrane behavior.

4.2.2. RATIOMETRIC MEASUREMENTS ON SINGLE CELLS

Figure 4.8 displays the behavior of the ratio parameter r measured in a spot within the lipid-based cellular membrane under variation of the temperature. There is a nonlinearity present around 17 °C reflecting a shift in the position of the emission spectrum of the dye. During this nonlinearity the ratio parameter is increased towards lower temperatures by $\approx \frac{0.035}{^\circ\mathrm{C}}$. Outside of this regime there is no significant shift detected. This behavior resembles the order of magnitude and direction of the shift in the ratio which for its part indicated a transition between two phase states in pure lipid interfaces ($\frac{0.04}{^\circ\mathrm{C}}$ - $\frac{0.1}{^\circ\mathrm{C}}$ as it has been characterized in section 3.2.3).

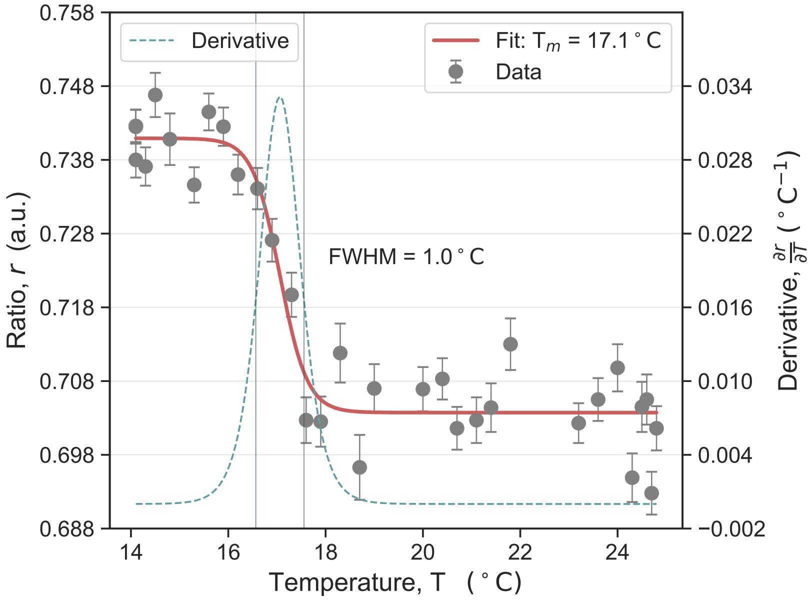

FIG. 4.8.: Optical state diagram measured on a single cell: Ratio parameter r is monitored as a function of temperature T within a cellular membrane patch of an intact single cell of the *SH-SY5Y* cell line. At approximately 17 °C the ratio undergoes a nonlinear shift similar to observations during phase transitions in lipid interfaces. [Fedosejevs et. al., [89]]

Hence, analogous to the lipid vesicle measurements in section 3.2.3, an optical state diagram of the system can be derived via this method. More precisely, the optical state diagram of a $\sim 1\,\mu\mathrm{m}^2$ cell membrane spot is measurable allowing access to its thermodynamics. The identified transition temperature T_m lies within a range where transition temperatures in mammalian cells are commonly found underpinning the interpretation as a phase transition [14, 11, 93]. Based on these data, the cell is in a liquid disordered phase in its living conditions (T = 37 °C).

The derivative of the optical parameter r is a quantity similar to a thermodynamic susceptibility such as heat capacity c_p as it was already discussed in section 3.2.1. By that, it is possible to characterize the transition and compare it to transitions observed via other methods (e.g. calorimetry). Similar to measurements in vesicles the full width at half maximum (FWHM) of the derivative of r is used to characterize the width of the transition. It is striking how sharp the transition appears (FWHM = 1.0 °C), especially compared to what is known so far for phase transitions in cells. A fundamental difference in this approach, however, is the investigation of single cells. As already stated, previously studied transitions were rather broad (~ 15 °C). However, the results were derived from ensembles which might be the reason for the broadening. This hypothesis will be discussed in more detail in section 4.4.

For these measurements the principle correlation between absolute emission intensity and ratio parameter has been observed as well and is approached similarly as for the vesicle suspensions (Appendix A.6). Intensity variations during the measurements in cellular membranes occur, for instance, due to undulations of the membrane. By that, it seems plausible that the membrane covers the confocal volume to a varying degree throughout the measurement [94].

The nonlinearity in the optical response identified as phase transition could be observed repeatedly for several ($n > 12$), individual single cells. It appears that the sharp nature of the transitions is consistently visible throughout the measurements merely the transition temperatures T_m vary. The distribution of the transition temperatures and the transition widths of 12 measurements is given in **Fig. 4.9**. The widths are mainly smaller than 1.6 °C with an average of (1.01 ± 0.17) °C. The transition temperatures vary between 15 °C and 22 °C. Further, there is an accumulation of T_m between 17 °C and 20 °C.
This observation agrees with Eigen's theory of quasispecies as no two individuals (cells) are expected to be identical copies but reveal small deviations. According to Eigens theory of evolution small defects in the copy of DNA are necessary for evolutionary processes to start [95]. The system is more flexible to react to environmental changes if not all individuals have similar properties. The individual with the most suitable properties to given conditions will most likely survive. Similar to that prediction a distribution of individual transition temperatures around one central value is observed.

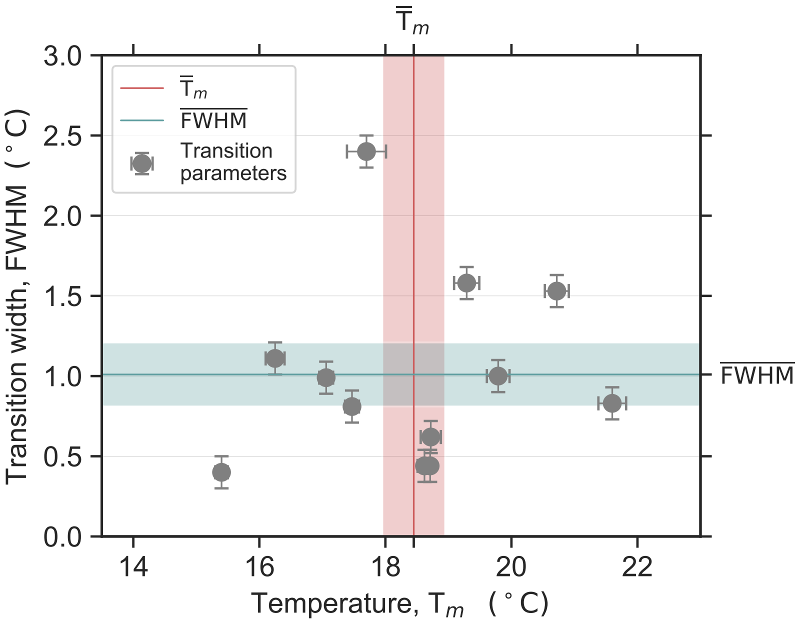

FIG. 4.9.: Overview of the single cell measurements: Transition parameters of 12 different measurements. Transition temperatures T_m vary between 15 °C and 22 °C and the widths mostly between 0.4 °C and 1.6 °C with an outlier at FWHM = 2.4 °C. Mean values and their standard error are indicated with the red ($\overline{T}_m$) and blue ($\overline{\text{FWHM}}$) line and their associated translucent areas.

These results strongly indicate the existence of phase transitions in the lipid-based membranes of excitable cells. The utilization of the *Atto488 DPPE* dye as local state reporter is well suited for this cellular application as it couples universally to the thermodynamics. A highly nonlinear behavior in the cellular membrane is the basis of excitability as it has been predicted, for instance, for nerve pulse conduction. By that, an important missing link is provided to couple theoretical predictions with phenomena in real, living systems. The sharpness of the transition means that it is excitable upon a relatively small variation in external parameters (here: $\approx$ 1 °C) when the state is close to the transition regime. Referring to action potentials this can be interpreted as a sharp excitation threshold modulating the all-or-none behavior of these signals.

4.2.3. REVERSIBILITY OF THE TRANSITION

A fundamental principle in the nature of phase transitions is the reversibility. Even though the path between to phase states may vary within a phase diagram start and end point must be similar.

However, there are phenomena in cells which are not reversible such as the denaturation of proteins. It means an unfolding of the protein as the quaternary/tertiary structure dissolves and the amino chain unfolds itself. The spatial structure of the folded amino acid sequence determines the function of the protein as two proteins with similar amino acid chains can have fundamentally different (tertiary/quaternary) spatial structures and with that different functions. Thus, the loss of structure equals the loss of function and which is mostly irreversible within a living system. This has been demonstrated by calorimetric measurements of (bacterial) cells, as well, where a reversible heat capacity peak originating from the lipids phase transition is visible. Additionally, a mainly irreversible heat capacity peak caused by the denaturation of proteins is resent [11]. Denaturation of proteins is suggested to be a cause of cell death as it happens for instance within high fever and hyperthermia ($T > 40\,°\mathrm{C}$) [96, 97].

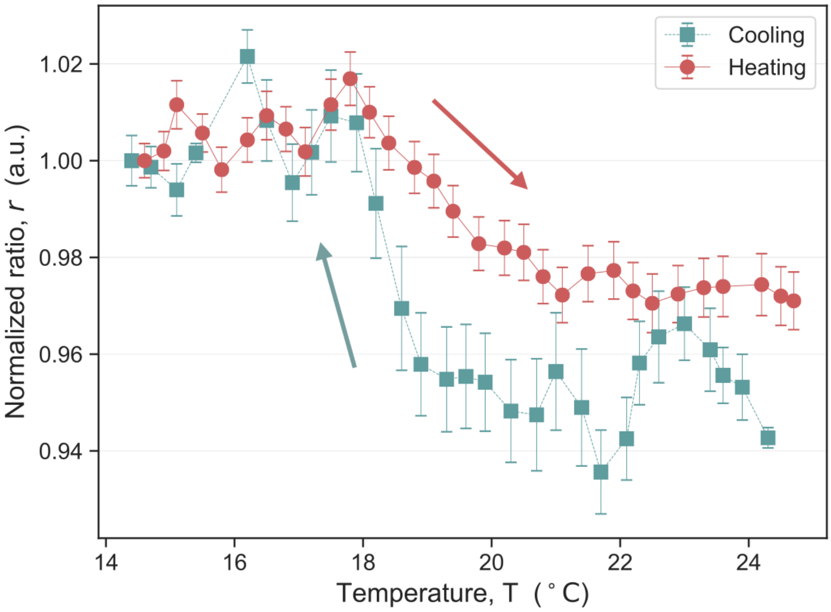

FIG. 4.10.: Direct comparison of heating (red) and cooling (blue) within one spot in the cellular membrane. Upon heating the transition is smoother [FWHM = 1.6 °C] than during cooling [FWHM = 0.4 °C] while the transition temperatures differ by 0.6 °C. [Fedosejevs et. al., [89]]

Indeed, there is not only denaturation at warm temperatures but a *cold* denaturation has also been reported [98]. By checking for reversibility (**Fig. 4.10**) of the nonlinearity in the ratio parameter r a major characteristic and necessary criteria of a phase transition is investigated. At the same time, the effect can be distinguished from protein denaturation as an origin of this observation.

Figure 4.10 displays two subsequent measurements conducted on the same spot within the cellular membrane. In blues squares the ratio parameter r is shown upon cooling from 25 °C and in red dots upon following heating. In both directions the beforehand described nonlinearity in r along with the maximum in the optical susceptibility is reflected.

The combination of both measurement directions in **Fig. 4.10** allows a direct comparison of the pathways of r and differences are prominent. During cooling the transition tends to be sharper than during heating of the cell which is referred to as hysteresis. Upon heating the system takes more time to accommodate to the temperature changes in order to break up the higher ordered structure of the gel-like phase. Additionally, a less pronounced “step” is present in the heating process which follows the cooling process. This is most likely because a smaller amount of dye participates in the process. Metabolization effects (endocytosis) progress over time and constantly lower the amount of dye in the membrane. By that, the background signal increases and the signal to noise ratio gets worse over time. However, the demonstration of the principle reversibility of this nonlinear behavior in the membrane further underlines its interpretation as a phase transition.

4.2.4. DETECTION OF TRANSITIONS IN MORE PARAMETERS

As consistently stated throughout this study a phase transition is an overall phenomenon for the system and is most likely reflected in more than one parameter. In the following, there will be a short outline concerning further parameters of interest in which a phase transition might be detected.

MORPHOLOGY

Due to a highly increased softness of a lipid interface during a phase transition - reflected in maxima in the compressibility and bending elasticity - morphological effects are expected. These changes haven been studied already for lipid vesicles which reveal fission upon the crossing phase states [34]. During cell measurements qualitative changes could be detected in the morphology of the cells as well.

By comparing cells in top view scans before and after a measurement cycle (respectively before and after a phase transition) differences can be identified. It stood out that the conjunctions between the cells are altered, shifted their position or vanished. During a phase transition the material softens about one order of magnitude which allows conformational changes during the transition [31]. An example is depicted in **Fig. 4.11**. Top scans are recorded 2 μm above the glass surface which is set on the basis of a cross sectional scan.

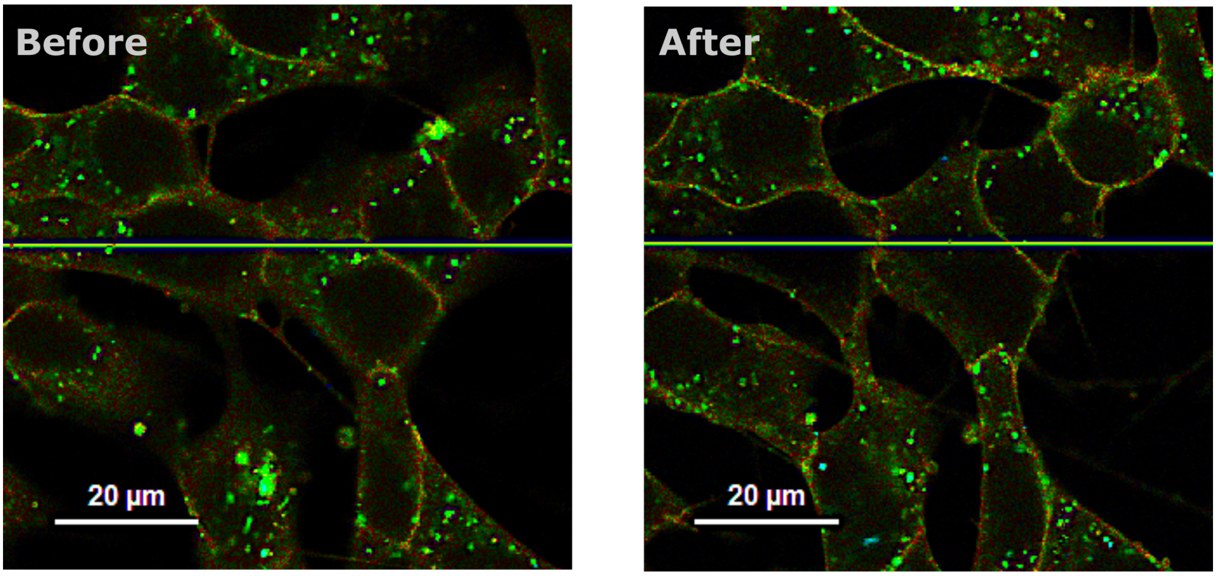

FIG. 4.11.: Direct comparison of top view scans recorded before and after a temperature variation between 25 °C and 15 °C. The horizontal yellow line indicates the position of the layer of the cross sectional scan.

DIFFUSION TIMES

The diffusion time was already consulted for localizing the origin of the optical response within the cellular membrane. The timescales for diffusion differ between membrane-bound dye and *free* dye by around one order of magnitude. During the measurement series the correlation curves were recorded to monitor this parameter simultaneously and assure the localization. However, the question arises whether the transition is reflected in the diffusion time of the membrane-bound dye as well.

A comparison of all fluorescence correlation curves during one measurement series is presented in **Fig. 4.12**. The curves are normalized to their value at ~ 1 ms. By that, the differences in the longest timescale of the curve, the diffusion time, are more emphasized as to $\tau_D > \tau = 1\,\text{ms}$ reflecting the part right of the normalization point.

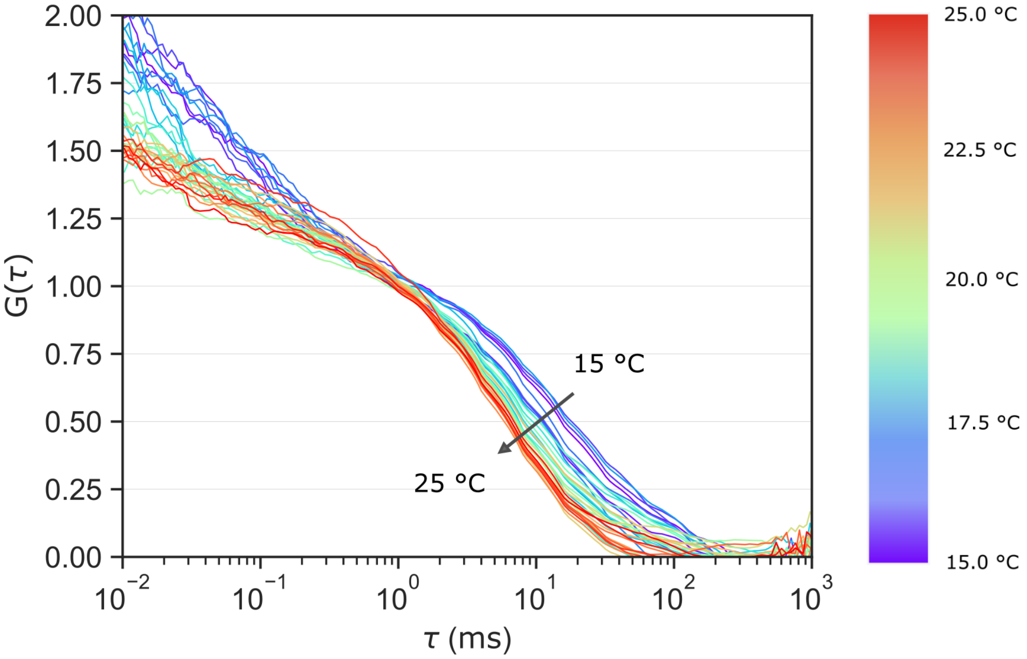

FIG. 4.12.: Normalized fluorescence correlation curves of *Atto488 DPPE* in the cellular membrane of SH-SY5Y cells upon temperature variation. The curves are normalized to their diffusion share at ~ 1 ms to highlight the variations in that timescale ($\tau_D > \tau = 1\,\text{ms}$).

Without further analysis a shift in the position of that timescale, identified as diffusion, is visible upon this comparison (indicated by an arrow in **Fig. 4.12**). It seems that the shift is more pronounced between 15 °C and 20 °C than between 20 °C and 25 °C. The associated ratio parameter of this series indicates the phase transition around 18 °C.

The analysis of these curves and the derivation of quantitative reliably results proves difficult. It appears that additional timescales seem to be present as a *normal* fit model containing one diffusion time and a triplet state does not fit the data properly. This has been found by others as well where the origins are not clear [99]. Membrane undulations have been suggested as the origin of intensity fluctuations as the cellular membranes is not steady in the detection volume [94].

It is rather the shape of the curves that does not comply the applied models. This indicates a hindered diffusion due to the heterogenous environment the dye experiences in the cellular membrane. According to [99] a model for hindered diffusion can in turn be replaced by two diffusion times. There, a phenomenologically derived, additional timescale was introduced into the model. Here, freely diffusing dye is considered but taking that timescale into account does not improve the fit.

Nevertheless, an attempt to derive quantitative timescales is presented in **Fig. 4.13**.

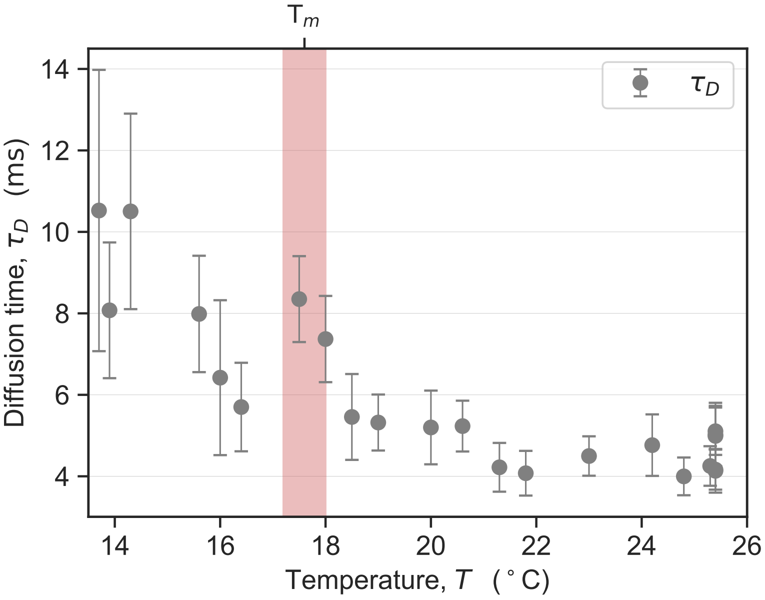

FIG. 4.13.: Diffusion times of membrane-bound dye in the cellular membrane of a SH-SY5Y cell upon variation of the temperature. Between 26 °C and 19 °C the diffusion remains rather constant. Below 19 °C the times are increased.

Due to the limitations of the models the diffusion times exhibit relatively high uncertainties. However, while the diffusion time remains on a constant level between 26 °C and 19 °C the time overall increases below 19 °C. Although the errors are relatively high the shift appears overall significant and aligns with the melting temperature derived from the ratio parameter. Based on these results the diffusion times are doubling between the phases.

Below the melting temperature the diffusion time and hence the diffusion coefficient is increased as it would be expected for a more ordered phase state. These results are similar to the results obtained on lipid monolayers according to the order of magnitude of the shift between the main phase states.

Compared to pure lipid systems the nature of diffusion is most likely altered in a heterogenous environment such as a plasma membrane. The composition contains zwitterionic and charged lipids, proteins etc. Due to the general lack of knowledge there are no predictions about the impact of phase states on the diffusion time within the cellular membrane possible. Also, whether a phase separation is present in the membrane is not clarified beyond doubt yet.
Diffusion times in cellular membranes are usually not investigated according to different phase states and there are not many data on that subject. In contrast, there are contradictory results as a study of diffusion times in cellular membranes has been even used to reject the existence of a phase transition: There were no sufficient changes in the diffusion time measurable as a difference over an order of magnitude was expected [100]. However, in that study a doubling in time would have not been accepted as sufficient as a simulation predicted a change by order of magnitudes. On the other hand, there are studies based on measuring the mixing behavior of two membrane sets from different cells. They reveal a pronounced nonlinearity in the mixing/diffusing behavior around 20 °C [101].

4.3. COUPLING OF MELTING POINT AND PH

As it was highlighted earlier, physiologically, the pH is an important quantity. The pK of a molecule (or chemical bond) defines in which *state* that molecule is present at a given pH, protonated or not. This affects massively the behavior of the molecule in the interplay with surrounding molecules. For example, within a lipid interface surface charges contribute to repulsive forces in between the interface molecules. In turn, this correlates with the resulting area per molecule and consequently the lateral pressure π within the layer.

In theory, at otherwise constant conditions (temperature, pressure, electrical field etc.) a shift in pH can induce significant structural changes in the membrane which can result in a phase transition. For that, it is required that the lipid headgroups are receptive to protons which is in the vicinity of their pK. This principle was demonstrated with measurements on lipid vesicle suspensions in section 3.2.3. Negatively charged lipids at pH 7.4 (pK 5.5) react towards a pH shift (to pH 5) with a correlated shift in T_m. On the other hand, neutral lipids with a pK at 2 are not influenced at all in their transition parameters and consequently in their structure during a similar shift (from pH 7.4 to pH 5.5).

Thus, the pH is a thermodynamically important parameter within organisms as it is able to act on the structure of membranes.

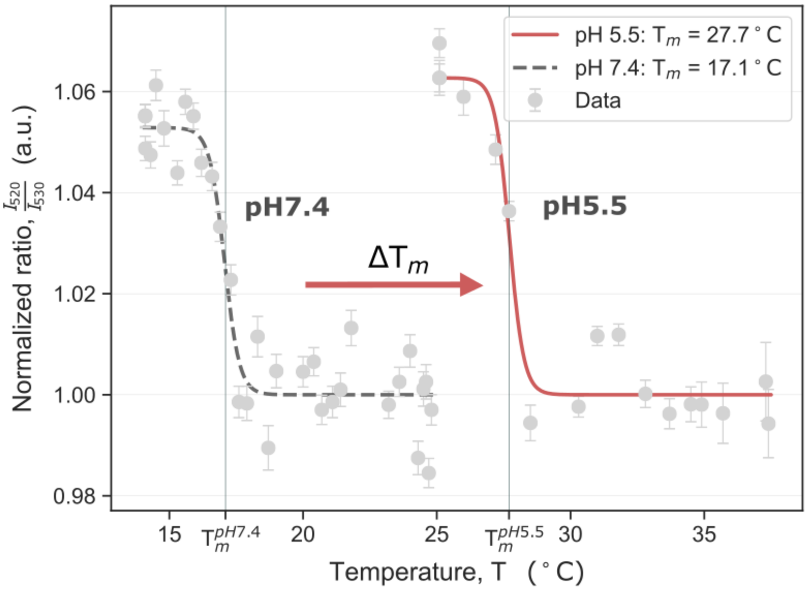

FIG. 4.14.: Direct comparison of the optical signal (ratio parameter r) in the cellular membrane of the neuronal cell at pH 7.4 and pH 5.5 derived from the similar measurement principle as introduced in 4.2.2. The lowering in pH, at otherwise similar conditions, results in a shift of T_m of roughly 11 °C towards higher temperatures.

As cellular membranes are negatively charged at a physiological pH (~ 7.4) a potential coupling of melting point and pH is investigated. A coupling would underline the biological relevance of the detected transition as local acidifications are omnipresent within the cell.

Similar measurements are conducted according to the prior introduced principle for single cells under variation of the extracellular pH. The results in section 3.2.3 have been demonstrated successfully that the lipid-dye complex does not react to bulk pH variations and purely to the physical state of the membrane.
The direct comparison of two exemplary measurement series recorded at pH 7.4 and pH 5.5 reveals that the nonlinearity is detected in both series but with a significant shift in the transition temperature (refer to **Fig. 4.14**). For these explicit measurements the transition temperature at pH 5.5 (T_m(pH 5.5) = (27.7 ± 0.4) °C) is increased by approximately 10 °C compared to pH 7.4 (T_m(pH 7.4) = (17.1 ± 0.3) °C) at otherwise similar conditions. This qualitative relationship has indeed been predicted by the equation that was presented in the theory section (equation 2.20 in section 2.2.4) concerning the effects of surface charges on the transition temperature. Upon an acidification (negative) surface charges of the lipid-based cellular membrane become neutralized and, consequently, the repulsive forces are reduced. This results in an increased transition temperature.

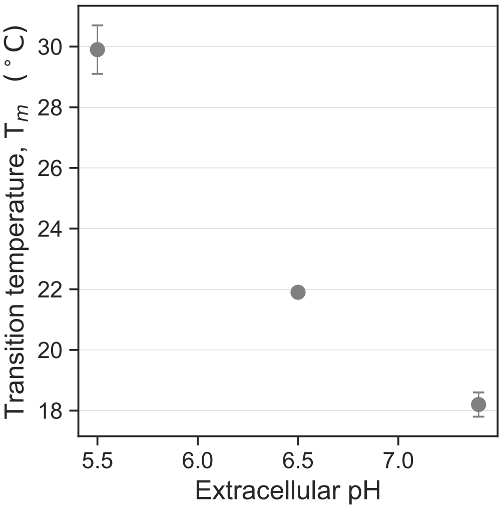

Fig. 4.15.: Overview of mean transition values of T_m at different pH values. From this data a shift of ∽ 5.5 °C per pH unit can be estimated. Note, in general, this factor is not expected to hold for a large range of pH units. The membrane is most receptive to protons around its pK.

This effect is confirmed in several measurements which are summarized in **Fig. 4.15**. The results verify that the cellular membrane of these neuronal cells is receptive to protons as this is a requirement for the mechanism and the associated equation 2.20 to apply. The cellular membrane reacts strongly to an acidification which is relevant from a physiological point of view as local pH shifts are present in cells/organisms. The coupling of pH and melting temperature is not expected to be linear since the membrane is most sensitive to pH changes in the vicinity of its pK, where a strong condensation is expected upon rather small changes in pH. A less pronounced response is expected further away from the pK. This is indicated in **Fig. 4.15** as well as the difference in T_m between pH 7.4 and pH 6.5 ($\Delta T_m \approx 4\,°C$) is smaller than the difference between pH 6.5 and pH 5.5 ($\Delta T_m \approx 8\,°C$) indicating the pK of the membrane below pH 6.5. According to the literature, a decrease of one pH unit is expected to result in an increase in T_m between 2°C and 35°C (table 2 in [102]) depending on the system and its state.

The pK of the membrane is defined by the individual composition of lipids and especially their headgroups. The membrane of these excitable, neuronal cells is apparently composed in that way, that pH variations are a powerful tool for acting on the membrane state within a physiological range of pH values. Further, at a constant temperature a pH shift is indeed able to induce a phase transition in the membrane. This is illustrated in **Fig. 4.16**. It is obvious that a transition can merely be triggered by pH alone if the other parameters are chosen accordingly.

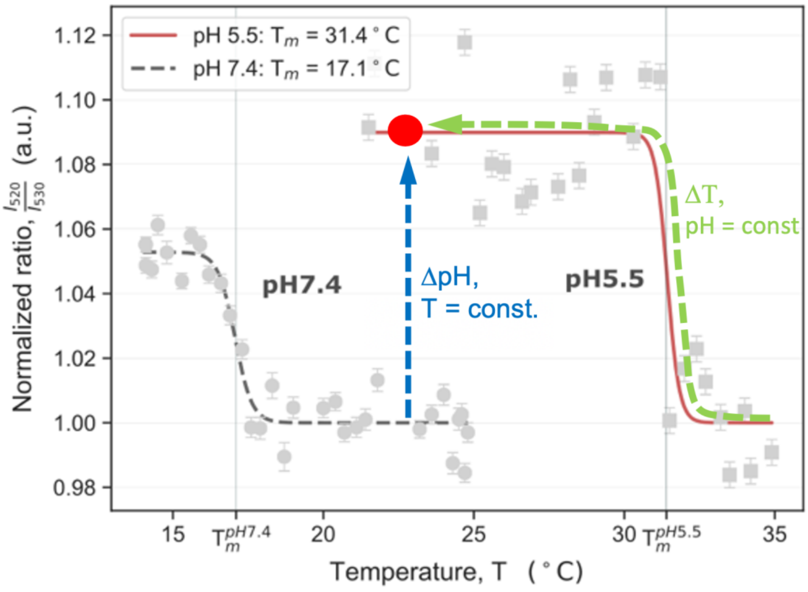

FIG. 4.16.: Optical illustration of an alternative path through the phase state diagram (dashed blue line). Based on the available data, in principle, a phase transition can be induced by a shift alone in pH at a constant temperature. [Fedosejevs et. al., [89]]

From these results it can be concluded, that the pH is indeed a potent state regulator within cellular systems. Consequently, the pH is able to control functions and the excitability of the membrane. In principle, local pH changes are able to induce a local phase transition and hence, an action potential could be triggered. This opens up a vast amount of possibilities/mechanisms of a cellular system to communicate.

4.4. SYNCHRONIZATION OF CELLS

4.4.1. SHARPNESS OF THE TRANSITION

Compared to all that is known about phase transitions in living systems the transitions measured here in single cells are extraordinarily sharp. The question arises whether these are contradictory results. From the single cell measurements alone, it seems that the cellular membrane undergoes a cooperative transition - similar to a monocomponent lipid monolayer - despite its diversity. The role of the heterogeneous composition of the cellular membrane remains unclear. However, cooperativity and heterogenous composition must not exclude each other: Processes such as the conduction of nerve pulses along cells are highly cooperative phenomena over a macroscopic range but are based on a heterogenous environment on the molecular level.

The transition width is defined by the extent of its cooperativity. Strictly speaking one can merely make statements about the membrane spot that is monitored during the measurement which is a patch of $\sim 1\,\mu\text{m}^2$. In a pure lipid layer this would approximately equal $\sim 10^6$ lipids but within cellular membranes there are also proteins and carbohydrates present. The composition of lipid types in living cell membranes varies across different cell types, but overall -PC (neutral at pH 7.4) lipids dominate and -PS and -PE (negatively charged at pH 7.4) lipids account for 10% of all lipids. Additionally, cholesterol is present up to 35 % in neuronal, excitable membranes (refer to table 2.1).

Figure 4.17 illustrates the superimposition of an increasing number of individual signals. The transition parameters of the individual signals were already presented in **Fig. 4.9**. The average of the sigmoidal fits reveals a broadened course between the two ratio levels of the different phase states. Thus, by measuring the signal of several cells simultaneously the transition would be expected to loose its sharpness. This is one important fact when comparing the sharpness measured here to the width measured in conventional methods (e.g. calorimetry) where samples consist of cell ensembles of rather millions of cells.

As already indicated in the theory of Eigenspecies, the distribution of the transition parameters of individual cells might be an evolutionary favored concept. An ensemble with distributed individual properties has enhanced capabilities to react towards environmental changes compared to an ensemble with assimilated properties. Within the distribution, the individual best adjusted towards the new conditions will survive and procreate. But, does that apply to cells within a functionalized network or within a unit of cells as well?

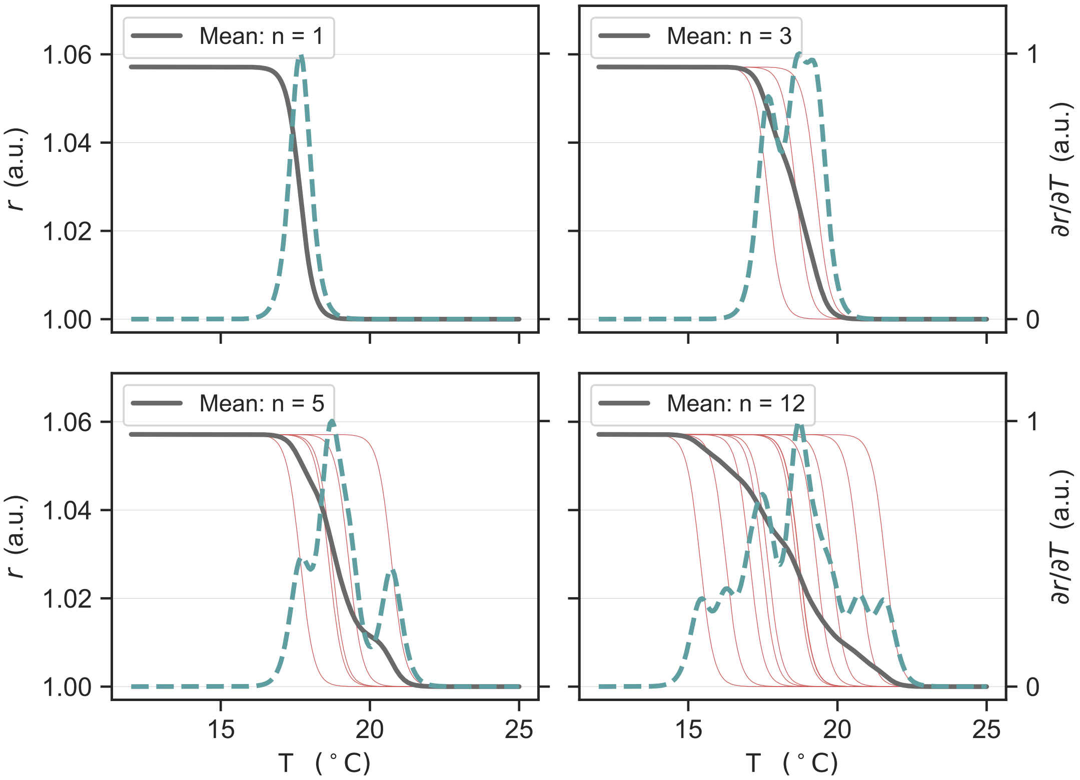

FIG. 4.17.: Qualitative overlay of the signals of different measurements. The melting temperatures of the individual measurements are rather distributed. Hence, upon averaging over an increasing number of measurements the sigmoidal shape broadens. For simplification all curves are simulated with the average *step size* and width extracted from all measured curves.

In contrary, for cells that shall *cooperate* an assimilation of properties would yield advantages concerning functionality. Rather aligned material properties would mirror a synchronization of the cells and would allow a rather efficient way of communication for instance. Communication within an organ requires a certain degree of cooperativity and the assimilation of cell parameters would assure that a signal propagates through all cells and is not hindered by an individual cell with deviating behavior.

For that, within the limitations of the setup, the behavior of connected cells will be shortly explored in the following. However, the setup and the measurement principle are not suited for tracking the optical signals from more than one spot at the time. Hence, the following results bare a lack of statistics as they are not easily reproducible. They can only offer an idea until these experiments can be conducted more thoroughly in the future.

4.4.2. MEASUREMENTS ON CONNECTED CELLS

Before investigating whether the transition points of neighboring cells are closer to each other than two distinct cells, the deviations in T_m within one cell are estimated.

SIGNAL FROM TWO SPOTS WITHIN ONE CELL

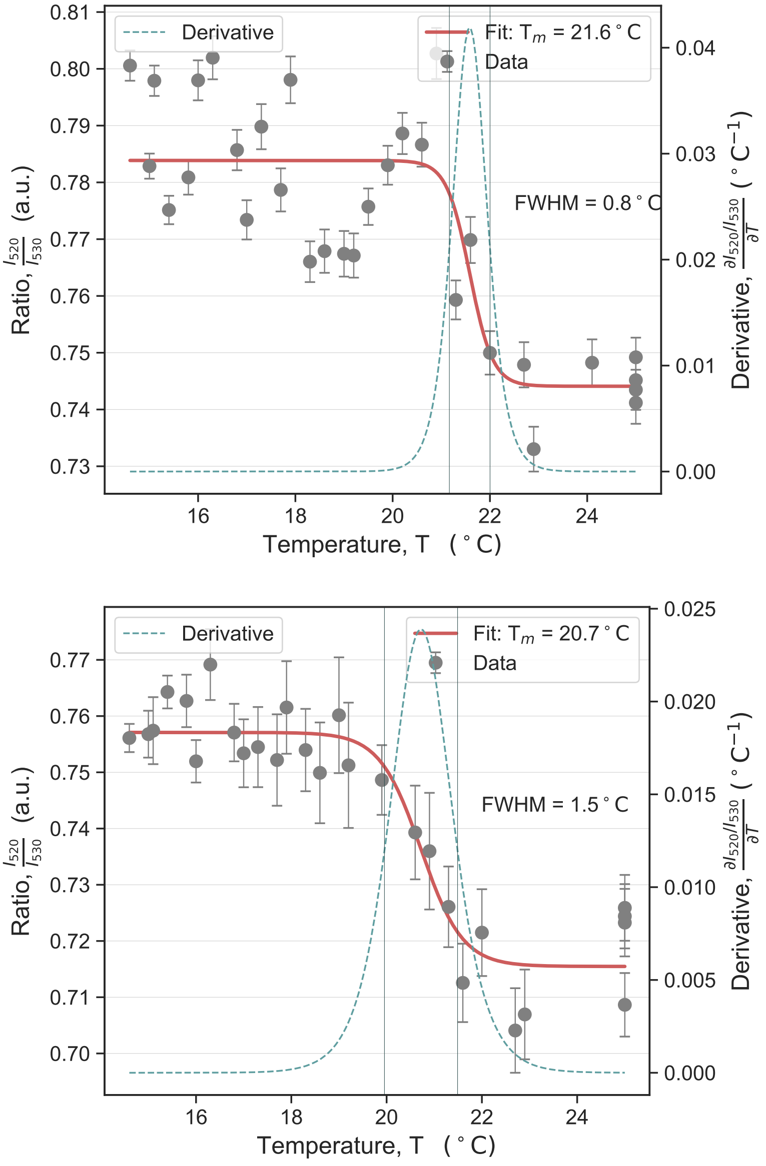

FIG. 4.18.: Two individual recordings of the optical response from two membrane spots in the same cell (cellular membrane) but at different locations. In both spots a typical profile of a phase transition is derived. The transition temperatures vary by 0.9 °C.

An impression of the variance in transition temperature within one cell shall be derived by measuring at two points of *one* cellular membrane simultaneously. In **Fig. 4.18** the individual traces of the ratio parameter r of both points are presented upon temperature variation between 25 °C and 15 °C. A phase transition around 21 °C is reflected in both measurement spots. The individual transition temperatures vary by $\Delta T_m = 0.9$ °C.

In general, the resolution of the temperature itself is limited to approximately 0.3 °C as it corresponds to the step size between two consecutive measurements. This uncertainty is exceeded by the difference in the single transition temperatures.
The direct comparison of the curves in **Fig. 4.19** reveals that the increase of the ratio parameter starts around 22 °C in *both* curves. Thus, both transitions happen in a similar temperature range. Merely due to the difference in the transition widths (0.8 °C and 1.5 °C) the absolute transition temperature is identified with a small offset. In summary, no significant deviation between the transition characteristics of these two points can be identified from this result. According to this data the absolute transition temperature would be indeed a constant parameter within one cell.

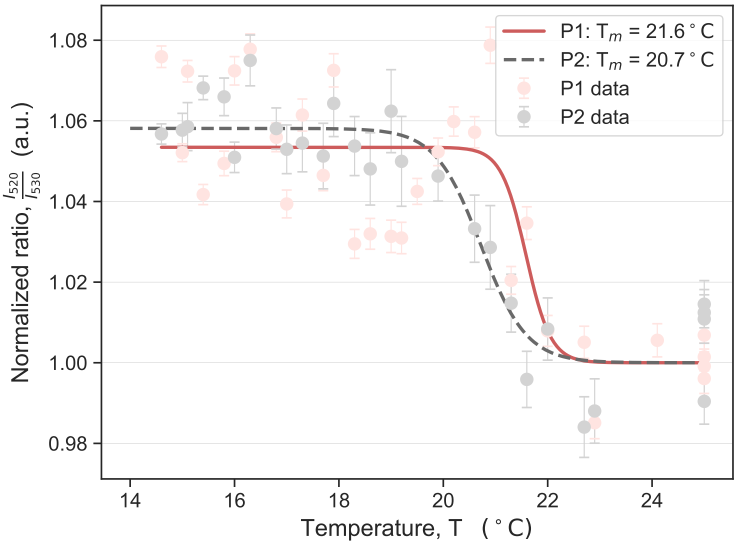

FIG. 4.19.: Direct comparison of both state diagrams measured in distinguished locations of one cell.

SIGNAL FROM TWO NEIGHBOURING CELLS

Further, the transition parameters of two adjacent cells are investigated. In **Fig. 4.20** the results of the individual measurements which are conducted simultaneously are presented. A difference of $\Delta T_m = 1.2$ °C in the individual transition temperatures is detected.

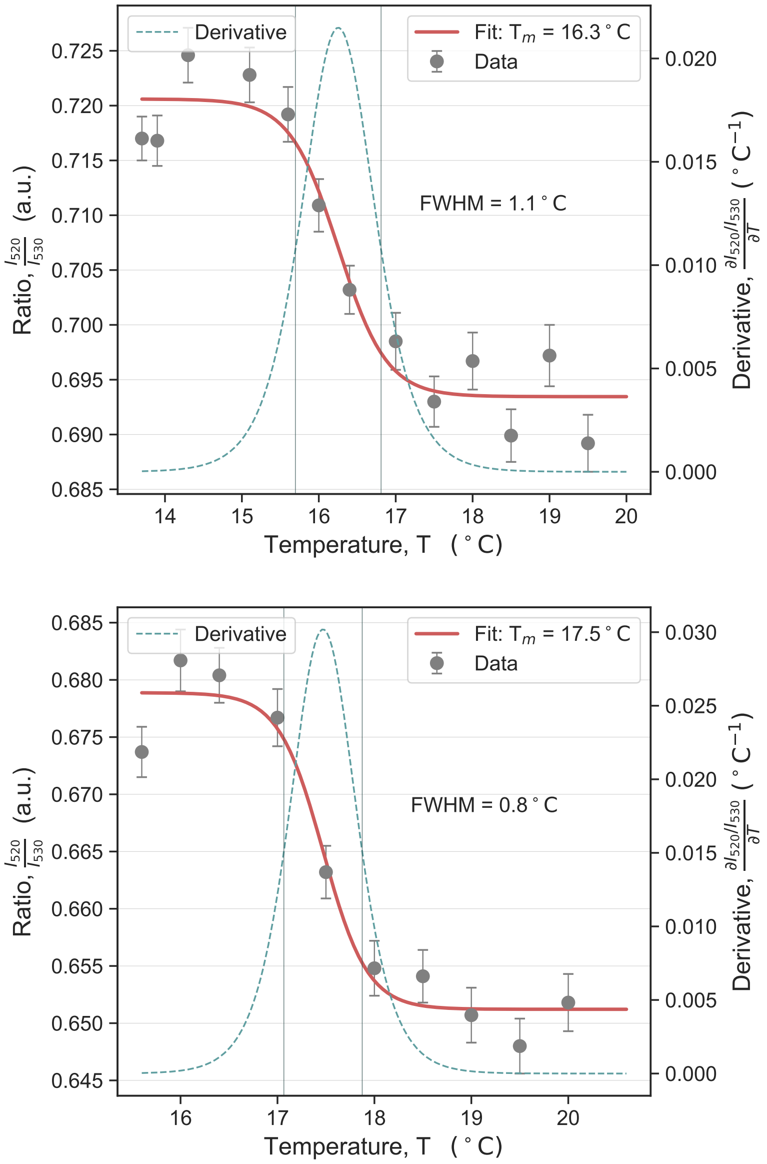

FIG. 4.20.: Profiles of the optical response within two cellular spots of two adjacent cells. The transition temperatures are at $T_m = 16.3\,°\mathrm{C}$ and $T_m = 17.5\,°\mathrm{C}$.

The conclusions of this measurement are limited. Here, the difference in both transition temperatures is more pronounced than compared to the results derived within one cell. However, the temperatures vary less than what would be expected from the overall distribution of (random) transition temperatures which were detected between 15 °C and 22 °C. A hint towards an assimilation between adjacent cells is given.

SIGNAL FROM A CELLULAR MONOLAYER

Measurements recording the whole optical response of a SH-SY5Y monolayer during temperature variation support this hypotheses. They reveal a sharp shift (FWHM = 1.8 °C) that can be associated with a phase transition at similar temperatures. These measurements are conducted within a spectrometer and the cells are stained with the dye Laurdan which has an established use for the characterization of order states within lipid systems.

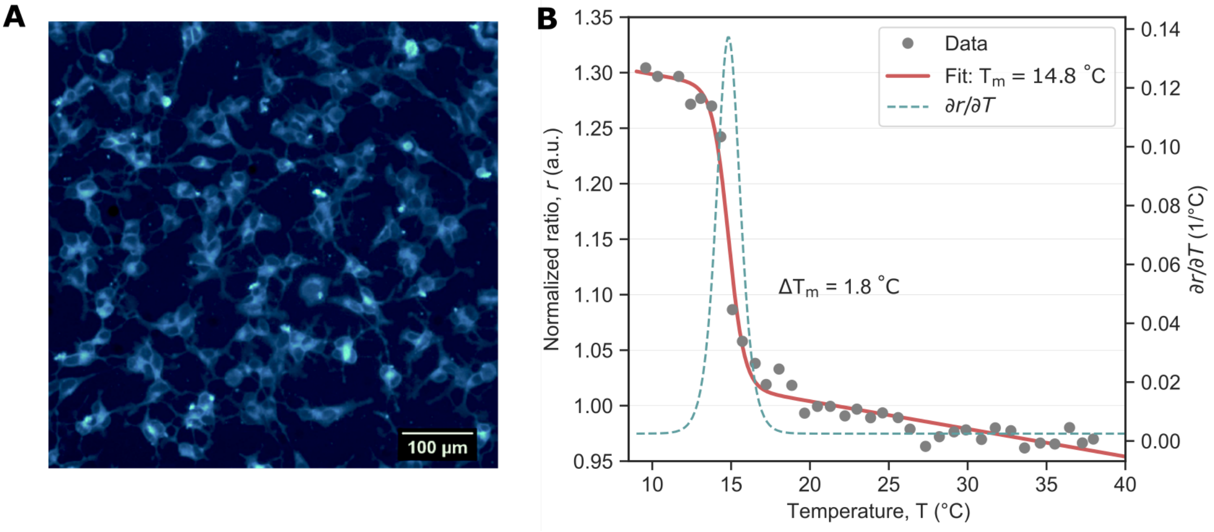

FIG. 4.21.: Left: Fluorescence image of SH-SY5Y cells stained with Laurdan. Right: State diagram of the cell monolayer. Data measured by Lukas Windgasse [103].

This result is remarkable as here the optical response of a few thousands of cells in the focus of the spectrometer is aligned such that the overall transition appears sharp. The monolayer consists of adjacent cells forming a network of neuronal cells. As already stated, within a network the signal transduction is a crucial element and the propagation would be most likely enhanced upon aligned material properties. The results are summarized in A.8 in the Appendix as well.

The transition point determines in which state the membrane is under given conditions. Excitability is not only controlled by the phase state but also by the state within the phase state as to the distance to the transition point. An aligned transition point within a unit of cells would lead to similar states and similar conditions for excitability. This synchronization could be a potential mechanism for a system to evolve into a network or how functionalized units such as tissue or organs develop. Upon network formation an adaption of the physical states seems evident which equals a self-organization within a biological system.

5. CONCLUSION

Within this thesis the concept of approaching biological, lipid-based membranes and getting access to their thermodynamic states via optical methods has been developed further. The use of (photostable) fluorescent dyes in combination with a confocal setup allows insights on a single cell level. Dyes such as *Atto488 DPPE* can work as *reporters of states* due to their unique response in emission properties to state changes. The entering of a thermodynamical coupling between the dye and the lipid interface where it is embedded has been characterized and verified in several lipid systems (SUVs, MLVs, monolayers..) and for different lipid types (charged, zwitterionic..) within this study.

Further, by establishing and applying the method of fluorescence correlation spectroscopy the characterization could be expanded to another level. Observations on a single molecule level are possible and dynamics (diffusion, protonation rates) are identified simultaneously to the phase state characterization. This builds the basis for approaching direct and localized state-to-function couplings in the future.

Thermodynamically, optical state variables such as the ratio parameter r, extracted from the emission spectrum of the dye, could be defined. It represents a function of state as the position of the emission spectrum of *Atto488 DPPE* shifts phase-dependently. By that, optical analogies to state diagrams and thermodynamical susceptibilities were derived for lipid systems.

The consequent and straightforward application of these findings to living cells revealed sharp phase transitions that can be located directly in the membrane of neuronal cells. The average transition temperature is found at $\overline{T}_m = 18.5\,°C$ and the average width of the transition is 1.0 °C.
These results turn the common knowledge of phase transitions in cells upside down as their existence and biological relevance has been often disputed. It is the first time that transitions have been identified in excitable cells and on a single cell level. Additionally, they are much sharper than known so far.

Sharpness means that the transition takes place over a relatively small variation of one variable, here temperature. This proves that it is possible to trigger a highly nonlinear transition in the membrane bearing a quite sharp threshold. The pure existence of these localized transitions in combination with their pronounced sharpness strengthens the thermodynamic approach to nerve pulse conduction. Describing the propagation of perturbations as localized phase transitions needs a threshold *excitation* in order to fulfill the requirements resulting from the phenomenology of nerve pulse propagation.
Further, the crucial role of phase transitions in living systems in general, as it has been proposed before, is underlined. Due to its sharpness a coupling of state and function, similar to known couplings in pure lipid systems, seems possible and a *switch-like* function evident.

The transitions are sensitive to pH as the average transition temperature was shifted to $\overline{T}_m = 29.9\,°C$ at pH 5.5 in the extracellular buffer. The proof of sensitivity of the system to protons is necessary for considering the observed nonlinear effect (phase transition) physiologically relevant. In order to be cholinergically excitable the cell must react to pH changes. The aforementioned small shift as a trigger could be a pH shift as local acidifications are present in cellular environments. Additionally, these data provide evidence that the transition could be induced by a pH shift alone at constant temperature.
The significance of the physical state of the membranes for functions is underlined. Excitation can be controlled via the physical state as the excitation strength needed for triggering a nonlinear pulse is determined by the distance of the state to the phase transition. Hence, local pH shifts can either bring the membrane closer to its transition and make it more easily excitable or suppress an excitation by shifting the membrane away from its transition point. However, a local shift in pH can also serve as the actual trigger depending on its strength and direction (acidification or alkalization). Importantly, from a thermodynamic point of view all variables are coupled and also other parameters such as mechanical stress or calcium would be able to induce a transitions.

It is indicated that the physical state is even a property subject to synchronization between adjacent cells. From the results, it seems that the physical state between two adjacent cells is more similar than between two randomly picked, individual cells. Cell monolayer in which the cells are connected and form a network-like entity again show a cooperative, sharp transition. This indicates that a synchronized state is present within the network. Assimilated material properties would enhance an efficient conduction of signals along the cells respectively the cellular membrane. Taking this thought further, this would result in an adapted threshold for triggering action potentials for all cells participating in the network. This might be a crucial mechanism for the formation of organs.

In summary, this thesis forms a basis for the utilization of fluorescence correlation spectroscopy for investigations of processes within membranes on a molecular level in combination with the characterization of thermodynamical states in these membranes. Furthermore, evidence is provided for the existence of localized phase transitions in excitable cellular membranes. The results underline the idea that the membrane state is crucial for excitability of action potentials. Further, it is able to modify cell functionality as it is itself subject to modulation by physiologically important parameters such as pH.

A. APPENDIX

A.1. CELLS

The SH-SY5Y cell line are neuroblastoma cells. It is a female cell line with neuron characteristics. SH-SY5Y cells (DSMZ, ACC 209) were cultured at 37 °C and 5 % CO_2 in medium containing Dulbecco MEM (PAN-Biotech) with 11 % Fetal Bovine Serum (FBS) (PAN-Biotech) and 1 % Penicillin-Streptomycin solution (PAN-Biotech). For sample preparation cells were transferred and grown on a cleaned coverslip.
Buffer for cell measurements and staining:

potassium chloride	2.70 mM	MW: 74.55 $\frac{\mathrm{g}}{\mathrm{mol}}$
sodium chloride	147 mM	MW: 58.44 $\frac{\mathrm{g}}{\mathrm{mol}}$
calcium chloride	2.00 mM	MW: 147.02 $\frac{\mathrm{g}}{\mathrm{mol}}$
HEPES	5.00 mM	MW: 238.31 $\frac{\mathrm{g}}{\mathrm{mol}}$

Osmolarity is adjusted to physiological conditions.

A.1.1. STAINING PROTOCOL

Prior to staining, cells were washed three times with buffer solution (5 mM HEPES, 2 mM CaCl2, 3 mM KCl, and 147 mM NaCl, pH 7.4). For staining 2 μL of a 0.5 mM stock solution of *Atto488 DPPE* (ATTO-TEC) in dimethyl sulfoxide (99.8 %; Acros Organics) was diluted in 2 mL of the buffer solution with a final concentration of 0.5 μM. Cells were incubated in the staining solution for 15 min at 37 °C and afterward rinsed again three times. For measurements with altered pH values the buffer was replaced (during staining and measurement) with a similar buffer which was acidificated by titration to the according pH with HCl.

A.2. PREPARATION OF VESICLE SUSPENSIONS

For lipid vesicle production, first, lipids along with 0.1 mol% Atto488 DPPE were dried by evaporation of the storage solution (DMPC: chloroform, DMPS: 65/35/8 chloroform/methanol/water and Atto488 DPPE: 80/20 chloroform/methanol) under a flow of nitrogen and subsequent incubation in a desiccator for ≈ 12 hours. Ultrapure water (arium pro, Satorius) is added to adjust a concentration of 2 mM lipids in the final suspension. The latter is heated 10 °C above the respective T_m (melting temperature) of the specific lipid type and repeatedly vortexed to form vesicles. By that, multilamellar vesicles (MLVs) are created. If needed, for a further downsizing to small unilamellar vesicles (SUVs), the suspension is sonicated with an ultrasonic rod and finally centrifugated.

A.3. PROTOCOLS FOR GUV PRODUCTION AND BIOTIN-NEUTRAVIDIN BINDING

A.3.1. SOLUTIONS

LIPID SOLUTION

For the biotin-neutravidin binding protocol, besides lipids and dye, 1 % biotin-DPPE is needed for incorporation into the GUVs. For FCS measurements a dye concentration of 0.001 mol% is chosen.

GLUCOSE SOLUTION

100 mosmol in total: 10 mM PB, 2 mM KCl, and glucose is added such that the solution becomes a 100 mosmol solution. This depends on the aspired pH and consequently, the ratio of the two phosphate buffers for adjusting the pH, as they have different osmolarities (2 resp. 3).

SUCROSE SOLUTION

100 mM sucrose in water.

A.3.2. PROTOCOL FOR PREPARING GUVS

CLEANING OF INDIUM TIN OXIDE (ITO) COATED GLASS SUBSTRATES

- Two ITOs and one teflon spacer are placed in 1 % mucasol solution and cleaned in ultra sonic (US) bath for 30 minutes
- ... for 30 minutes in isopropanol in US bath
- .... for 30 minutes in MiliQ water in US bath
- Dried under nitrogren stream
- Placed in petri dish and tested where the conductive side of the ITO slide points to
- 25 μl of lipid solution are put on the conductive side of each ITO slide and spreaded until chloroform/solvent is evaporated
- Minimum of 30 minutes in desiccator for complete removal of solvent

- ITOs are incorporated into a special copper chamber designed for this pupose and vaseline/vacuum grease is put between teflon spacer and ITO slide to prevent water leakage [for DPPC swelling: high quality vacuum grease is needed, otherwise vaseline melts during high temperatures]
- 100 mosmol sucrose solution is injected through holes in teflon spacer into the chamber until it is completely filled with solution
- Grease is put on top of holes to prevent water leakage

SWELLING

For swelling the copper chamber is heated above the phase transition temperature of the used lipid (DOPC: room temperature is sufficient; DMPC: ≈ 35 °C; DPPC: ≈ 50 °C). For heating, a peltier element is used with ≈ 2.5 V and placed on top of the copper chamber. For appropriate cooling another copper block is assembled onto the cooling side of the peltier element. Note, in case of DPPC GUV preparation: high temperatures are necessary and a PC radiator is used for additional cooling and an increased voltage at the peltier element applied in order to achieve the temperature. When the desired temperature is reached, a voltage generator with alternating voltage is clipped to both ITOs. Following protocol is applied:

- Start at 10 Hz and 100 mV
- Every 2 minutes voltage is raised in 100 mV steps towards 1.1 V
- At 1.1 V, hold for 1.5 hours (10 Hz)
- At last, 1.3 V at 4 Hz to support the detachment of the vesicles from the surface

Afterwards, the chamber is opened and the upper ITO is slided to one side such that the GUV solutions stays in the chamber. The solution is collected with an Eppendorf pipette and stored it in a tube.

A.3.3. BINDING PROTOCOL

In principle, the GUV solution is diluted 50 to 100 times with the glucose solution. The different sugar solutions promote the sinking of the GUVs, but to *fix* the to the substrate, further steps are required.

BINDING PROTOCOL IN THE CELL CHAMBER

- Cleaning of cover slides similar to the previously described cleaning of the ITO slides in the US bath
- Assembling of the chamber with the cleaned cover slide
- Injection of BSA-biotin solution ($0.1\,\frac{\mathrm{mg}}{\mathrm{ml}}$ Bovine serum albumin (BSA) labeled biotin) with an Eppendorf pipette directly into the chamber ($\approx 1.4\,\mathrm{ml}$)
- Incubation for 30 minutes
- Rinsing with water
- Injecting the neutravidin solution ($0.025\,\frac{\mathrm{mg}}{\mathrm{ml}}$)
- Incubation for 30 minutes
- Rinsing with water
- Injection of 1 ml glucose solution, and $50\,\mu$l GUV solution, than $600\,\mu$l glucose solution (alternatively: Mixing of both solutions beforehand and collecting solution with a tube and plastic syringe, than inject via tube into chamber. It needs to happen fast, before GUVs are settling on glass bottom of container)

A.4. MEASUREMENT CHAMBER

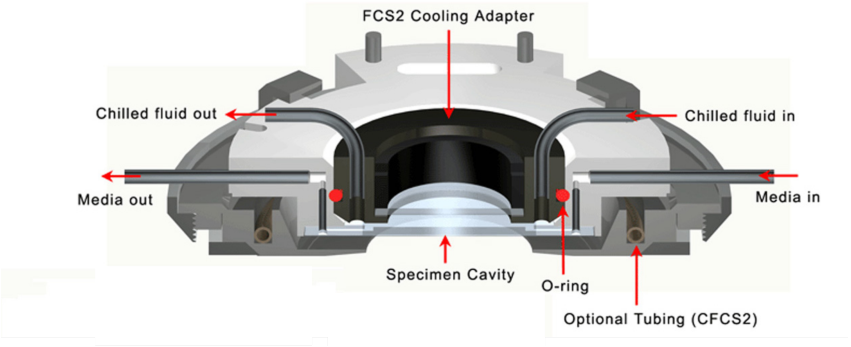

FIG. A.1.: FCS2 chamber system with a specimen cavity closed by a cover slide. [104]

A.5. ANALYSIS OF TCSPC HISTOGRAMS

A.5.1. ERROR ANALYSIS OF WEIGHTED LIFETIMES

INTENSITY WEIGHTED LIFETIME $\tau_{I_a v}$

$$\begin{aligned}
\tau_{I_{av}} &= \frac{I_1}{I_1 + I_2}\tau_1 + \frac{I_2}{I_1 + I_2}\tau_2 \\
\sigma_{\tau_{I_\mathrm{av}}} &= \sqrt{\sum_i \left(\frac{\partial \tau_{I_\mathrm{av}}}{\partial x_i}\right)^2 \sigma_{x_i}^2} \\
&= \frac{1}{I_1 + I_2}\sqrt{\left(\tau_1 - \tau_{I_\mathrm{av}}\right)^2 \sigma_{I_1}^2 + \left(\tau_2 - \tau_{I_\mathrm{av}}\right)^2 \sigma_{I_2}^2 + I_1^2 \sigma_{\tau_1}^2 + I_2^2 \sigma_{\tau_2}^2}
\end{aligned}$$

Error calculation of I_1 (σ_{I_2} is calculated analogously):

$$\begin{aligned}
\sigma_{I_1} &= \sqrt{\sum_i \left(\frac{\partial I_1}{\partial x_i}\right)^2 \sigma_{x_i}^2} \\
&= \sqrt{\left(A_1 \left(1 - \left(1 - \frac{(t_0 - t_\mathrm{max})}{\tau_1}\right) \mathrm{e}^{\frac{(t_0 - t_\mathrm{max})}{\tau_1}}\right)\right)^2 \sigma_{\tau_1}^2 + \tau_1^2 \left(1 - \mathrm{e}^{\frac{(t_0 - t_\mathrm{max})}{\tau_1}}\right)^2 \sigma_{A_1}^2 \frac{1}{\Delta t}}
\end{aligned}$$

AMPLITUDE WEIGHTED LIFETIME τ_{av}

$$\begin{aligned}
\tau_{av} &= \frac{A_1}{A_1 + A_2}\tau_1 + \frac{A_2}{A_1 + A_2}\tau_2 \\
\sigma_{\tau_{av}} &= \sqrt{\sum_i \left(\frac{\partial \tau_{av}}{\partial x_i}\right)^2 \sigma_{x_i}^2} \\
&= \frac{1}{A_1 + A_2}\sqrt{(\tau_1 - \tau_{av})^2 \sigma_{A_1}^2 + (\tau_2 - \tau_{av})^2 \sigma_{A_2}^2 + A_1^2 \sigma_{\tau_1}^2 + A_2^2 \sigma_{\tau_2}^2}
\end{aligned}$$

A.5.2. EXEMPLARY POWER SERIES FOR TCSPC HISTOGRAMS

To verify that the lifetime is indeed an intensity independent parameter a power series can be conducted. By that, the excitation strength of the laser is successively increased. As a consequence, the emission intensity is increased as well. To compare the shapes of the histograms the TCSPC curves are normalized.

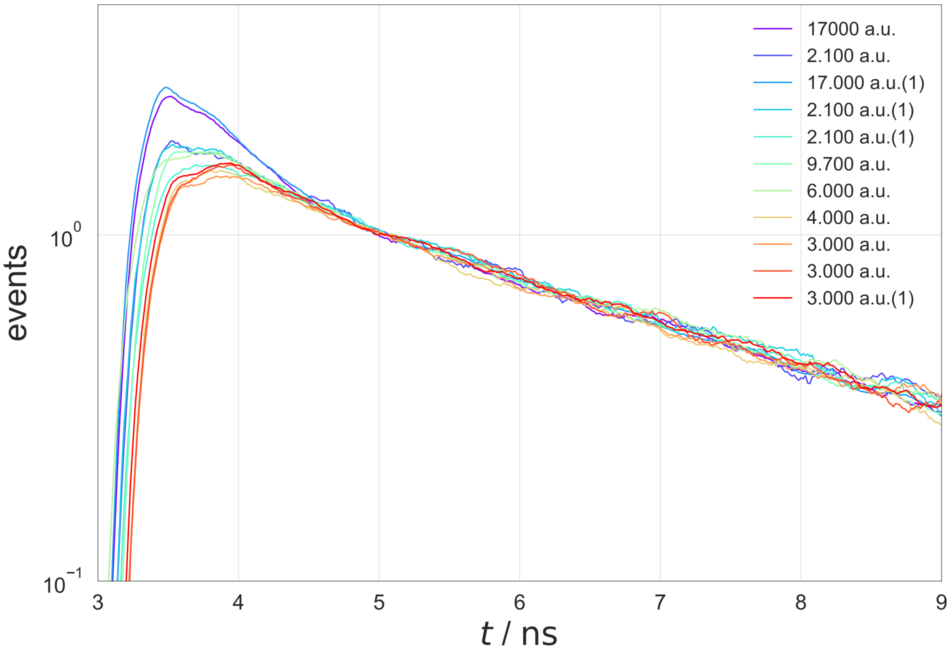

FIG. A.2.: Comparison of TCSPC histograms under variation of the laser excitation intensity. A normalization to $\tau = 5\,\text{ns}$ highlights that the changes associated with intensity variations occur at the maximum of the histogram. The fluorescence lifetimes are determined by the slope of the histogram as to the time constant of the exponential decay. The slopes of the histograms align for all excitations strength.

While the region with the maximum of the TCSPC histogram is altered, the slope remains constant which is decisive for the lifetime. The shape around the maximum itself varies for different excitation strengths as the instrument response function - calculated and extracted by the software of the device itself - has different shares of the signal. However, an important consequence from this measurement is concerning the analysis: The starting point for the fit should not be picked directly at the maximum as its position can shift due to emission intensity variations. Upon this (visual) comparison it becomes clear, that the lifetime is not influenced by the variation in the intensity. A similar result is gained from the calculation of the intensity weighted lifetime directly.

A.5.3. TCSPC HISTOGRAM ANALYZED BY WIDTH

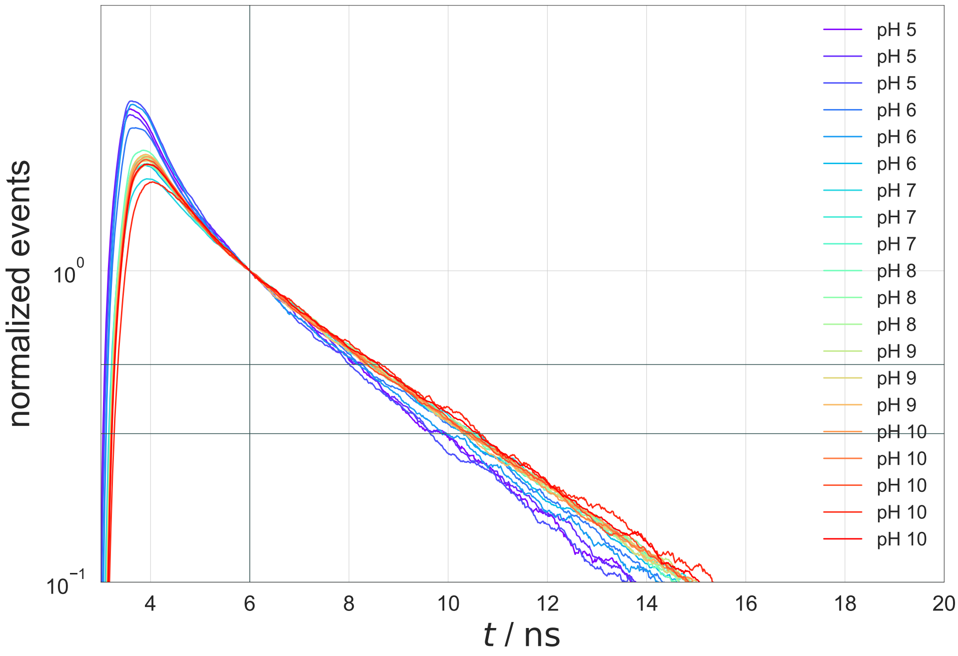

FIG. A.3.: Comparison of TCSPC histograms of *Fluorescein DHPE* in DMPC SUVs at different pH values. Histograms are normalized (indicated by the vertical line)and effects of intensity variations (modulation of the shape of the maximum) can be distinguished from changes in fluorescence lifetimes. The horizontal lines indicate potential levels at which the width of the histograms can be compared.

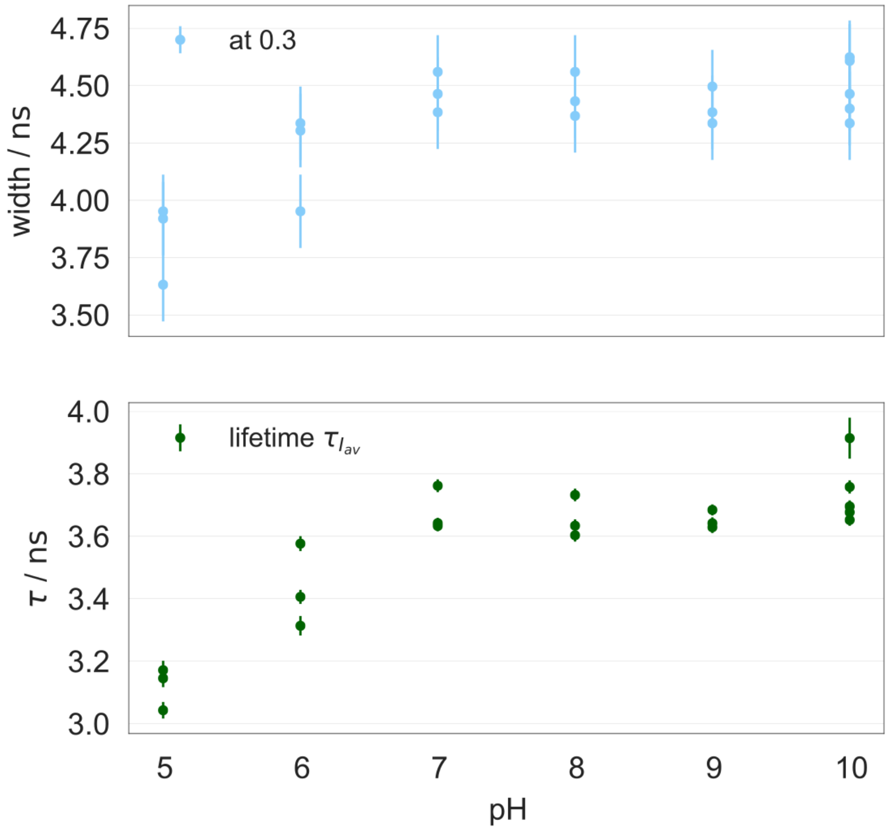

FIG. A.4.: Comparison of fluorescence lifetime and width of the normalized TCSPC histogram of DMPC SUVs with *Fluorescein DHPE* under variation of the pH. (1): Width of the normalized histograms at level $y = 0.3$; (2): Intensity weighted lifetime $\tau_{I_{av}}$. Both parameters exhibit similar results. The width is a parameter that is phenomenologically derived.

A.6. CORRELATION BETWEEN INTENSITY AND RATIO PARAMETER

Based on the mostly linear correlation between ratio r and intensity I a linear regression is performed on the measured values. The slope of this fit a is then used to calculate a *new* ratio value that is corrected with respect to the intensity variations along one measurement. By that, changes accounting to these intensity instabilities shall be compensated.

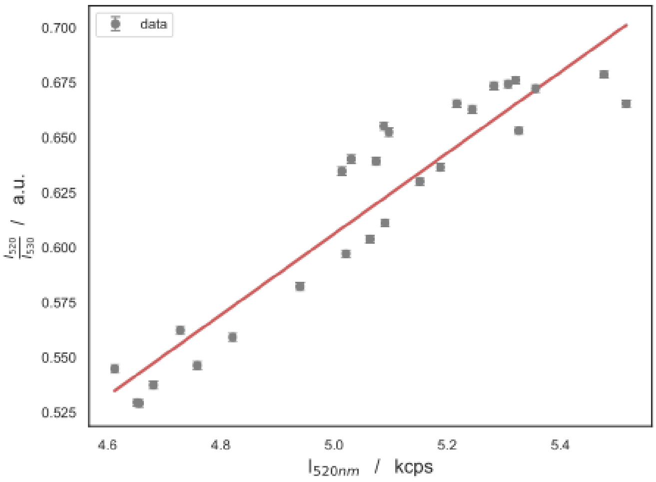

FIG. A.5.: Correlation between ratio parameter r and absolute intensity I including a linear regression of these values.

The ratio r is corrected by the following relation:

$$r_{\text{corr}} = r - (I - I_0)a$$

$$\sigma_{r_{\text{corr}}} = \sqrt{\sigma_r^2 + a^2(\sigma_I^2 + \sigma_{I_0}^2) + (I - I_0)^2\sigma_a^2}$$

One reference value I_0 is chosen to which the changes are calculated. The value is not significant for the outcome as it merely defines absolute values. Here, the detection of relative changes is aimed for.

Note, the correlation between r and I cannot be characterized by a universal factor a. It has to be determined in each measurement series again for example by a reference measurement at a constant temperature prior to the measurement.

A.7. MONOLAYER - POINT MEASUREMENTS

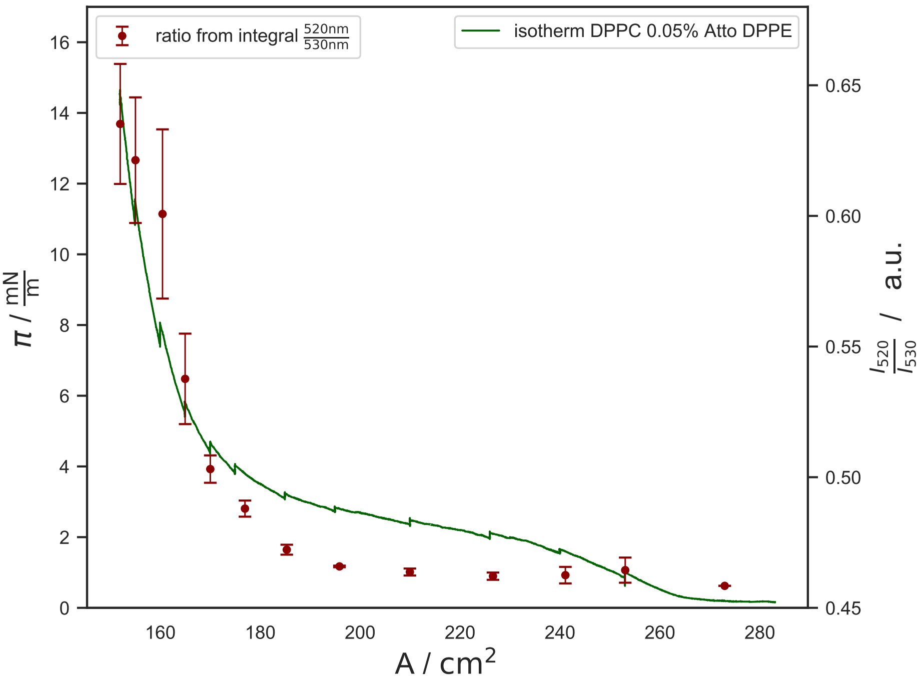

FIG. A.6.: Stepwise driven isotherm with associated point measurements recorded between the compression *steps*.

A.8. GRAPHICAL SUMMARY OF SINGLE CELL AND CELL LAYER MEASUREMENTS

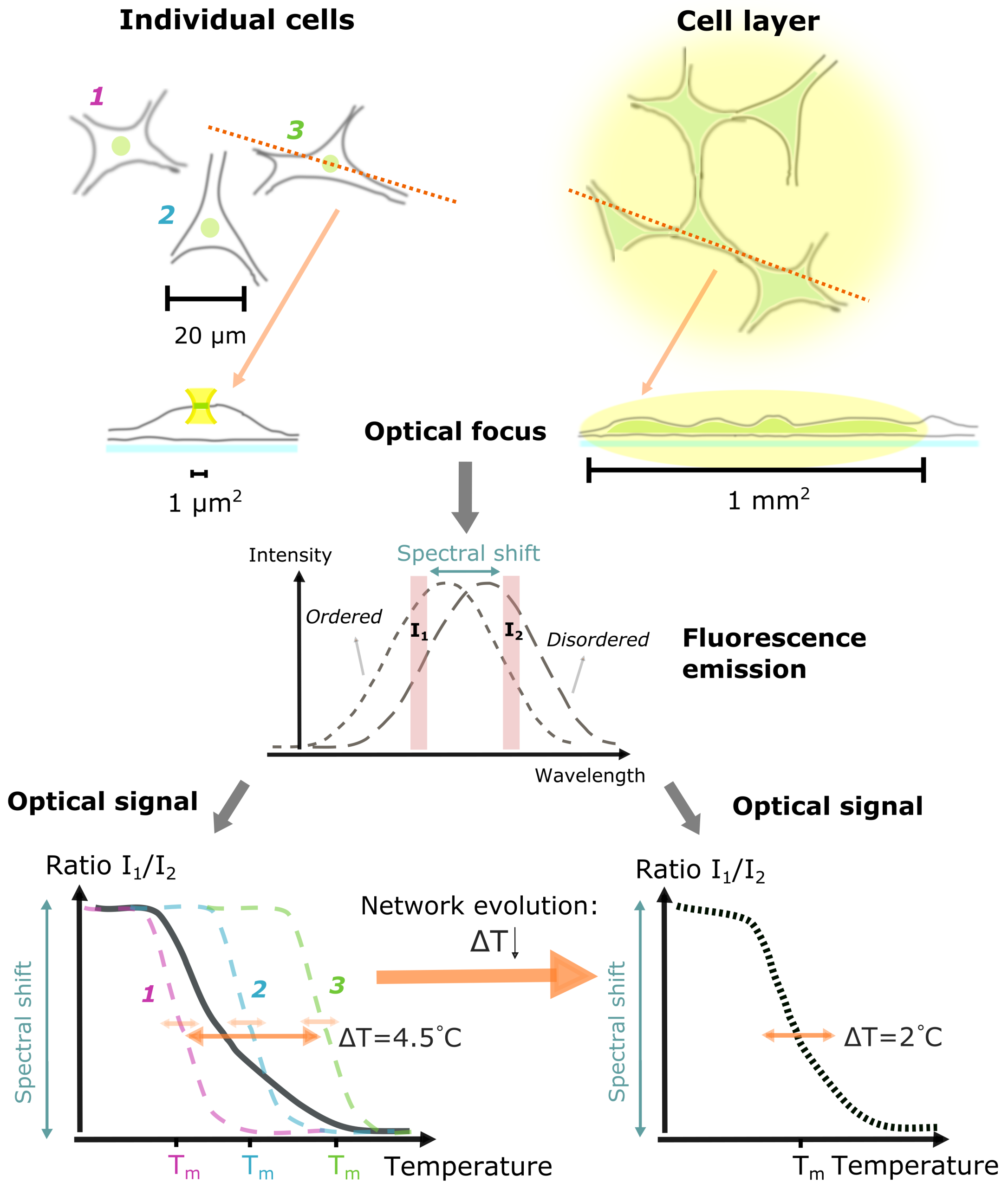

FIG. A.7.: Comparison of measurements on single cells and connected cells within a cell layer.

BIBLIOGRAPHY

[1] E. Schrödinger, *Was ist das Leben? Der physikalische Aspekt der lebenden Zelle.* Dublin: Trinity College Press, 1944.

[2] J. D. Watson and F. H. Crick, "Molecular structure of nucleic acids: a structure for deoxyribose nucleic acid," *Nature*, vol. 171, no. 4356, pp. 737–738, 1953.

[3] A. L. Hodgkin and A. F. Huxley, "A quantitative description of membrane current and its application to conduction and excitation in nerve," *Bulletin of Mathematical Biology*, vol. 52, no. 1-2, pp. 25–71, 1990.

[4] B. Wunderlich, C. Leirer, A. Idzko, U. F. Keyser, A. Wixforth, V. M. Myles, and T. Heimburg, "Phase-State Dependent Current Fluctuations in Pure Lipid Membranes," *Biophysical Journal*, vol. 96, no. 11, pp. 4592–4597, 2009.

[5] S. Shrivastava and M. F. Schneider, "Evidence for 2D Solitary Sound Waves in a Lipid Controlled Interface and its Biological Implications for Biological Signaling," *Journal of The Royal Society Interface*, vol. 11, pp. 1–8, 2014.

[6] T. Heimburg and A. D. Jackson, "On soliton propagation in biomembranes and nerves.," *Proceedings of the National Academy of Sciences of the United States of America*, vol. 102, no. 28, pp. 9790–9795, 2005.

[7] T. Heimburg and A. D. Jackson, "On the action potential as a propagating density pulse and the role of anesthetics," *Biophysical Reviews and Letters*, vol. 02, no. 01, pp. 57–78, 2007.

[8] T. Heimburg, "Nerves and Anesthesia: A physics perspective on medicine," *arXiv preprint*, p. 8, 2014.

[9] H. Träuble and H. Eibl, "Electrostatic effects on lipid phase transitions: membrane structure and ionic environment," *Proceedings of the National Academy of Sciences of the United States of America*, vol. 71, no. 1, pp. 214–219, 1974.

[10] L. Thilo, P. Overath, and H. Träuble, "Mechanistic Interpretation of the Influence of Lipid Phase Transitions on Transport Functions," *Biochemistry*, vol. 16, no. 7, pp. 1283–1290, 1977.

[11] T. Mužić, F. Tounsi, S. B. Madsen, D. Pollakowski, M. Konrad, and T. Heimburg, "Melting transitions in biomembranes," *Biochimica et Biophysica Acta - Biomembranes*, vol. 1861, no. 11, p. 183026, 2019.

[12] J. R. Hazel, S. J. McKinley, and E. E. Williams, "Thermal adaptation in biological membranes: interacting effects of temperature and pH," *Journal of Comparative Physiology B*, vol. 162, no. 7, pp. 593–601, 1992.

[13] E. F. Delong and A. A. Yayanos, "Adaptation of the membrane lipids of a deep-sea bacterium to changes in hydrostatic pressure," *Science*, vol. 228, no. 4703, pp. 1101–1103, 1985.

[14] J. H. Crowe, F. A. Hoekstra, L. M. Crowe, T. J. Anchordoguy, and E. Drobnis, "Lipid phase transitions measured in intact cells with fourier transform infrared spectroscopy," *Cryobiology*, vol. 26, no. 1, pp. 76–84, 1989.

[15] D. L. Melchior and J. M. Steim, "Thermotropic transitions in biomembranes.," *Annual review of biophysics and bioengineering*, vol. 5, pp. 205–238, 1976.

[16] G. M. Cooper and R. Hausman, "A molecular approach," *The Cell. 2nd ed. Sunderland, MA: Sinauer Associates*, 2000.

[17] A. Johnson, J. Lewis, M. Raff, K. Roberts, and P. Walter, "Molecular biology of the cell," *Garland Science*, vol. 4, 2002.

[18] "DMPS data sheet." `https://avantilipids.com/product/840033/`. Accessed: 2021/11/18.

[19] S. J. Singer and G. L. Nicolson, "The fluid mosaic model of the structure of cell membranes," *Science*, vol. 175, no. 4023, pp. 720–731, 1972.

[20] G. Cevc, *Phospholipids handbook*. CRC press, 2018.

[21] D. Fitzner, J. M. Bader, H. Penkert, C. G. Bergner, M. Su, M.-T. Weil, M. A. Surma, M. Mann, C. Klose, and M. Simons, "Cell-type-and brain-region-resolved mouse brain lipidome," *Cell Reports*, vol. 32, no. 11, p. 108132, 2020.

[22] H. Träuble, "Membrane Electrostatics," in *Structure of Biological Membranes*, pp. 509–550, Boston, MA: Springer US, 1977.

[23] H. B. Callen, *Thermodynamics and an Introduction to Thermostatistics*. John Wiley & Sons, 1985.

[24] T. Heimburg, *Thermal Biophysics of Membranes*. 2007.

[25] B. Fichtl, "Integration der Biochemie in die Physik der Grenzfläche," *Dissertationsschrift Universität Augsburg*, 2015.

[26] H. Ebel, P. Grabitz, and T. Heimburg, "Enthalpy and Volume Changes in Lipid Membranes . I . The Proportionality of Heat and Volume Changes in the Lipid Melting Transition and Its Implication for the Elastic," *The Journal of Physical Chemistry B*, vol. 105, no. 30, pp. 7353–7360, 2001.

[27] R. Winter and C. Jeworrek, "Effect of pressure on membranes," *Soft Matter*, vol. 5, no. 17, pp. 3157–3173, 2009.

[28] A. Einstein, "Theorie der Opaleszenz von homogenen Flüssigkeiten und Flüssigkeitsgemischen in der Nähe des kritischen Zustandes," *Annalen der Physik*, vol. 338, no. 16, pp. 1275–1298, 1910.

[29] M. J. Klein, A. J. Kox, J. Renn, R. Schulmann, and C. W. Kilmister, "The Collected Papers of Albert Einstein, vol. 3, The Swiss Years: Writings, 1909-11," 1995.

[30] L. D. Landau and E. Lifshitz, "Course of Theoretical Physics, vol5," ch. Statistica, p. 544, Oxford: Pergamon Press, 1980.

[31] D. Steppich, J. Griesbauer, T. Frommelt, W. Appelt, A. Wixforth, and M. F. Schneider, "Thermomechanic-electrical coupling in phospholipid monolayers near the critical point.," *Physical review. E, Statistical, nonlinear, and soft matter physics*, vol. 81, no. 6 Pt 1, p. 061123, 2010.

[32] H. Träuble, M. Teubner, P. Woolley, and H. Eibl, "Electrostatic interactions at charged lipid membranes. I. Effects of ph and univalent cations on membrane structure," *Biophysical Chemistry*, vol. 4, no. 4, pp. 319–342, 1976.

[33] C. Fillafer and M. F. Schneider, "On the excitation of action potentials by protons and its potential implications for cholinergic transmission," *Protoplasma*, vol. 253, no. 2, pp. 357–365, 2016.

[34] C. Leirer, B. Wunderlich, V. M. Myles, and M. F. Schneider, "Phase transition induced fission in lipid vesicles," *Biophysical Chemistry*, vol. 143, no. 1-2, pp. 106–109, 2009.

[35] S. Nuschele, *The Role of Interfaces in Enzyme Activity and Cell Adaptation*. PhD thesis, 2010.

[36] M. F. Schneider, "Living Systems Approached from Physical Principles," *Prog Biophys Mol Biol*, 2020.

[37] T. Heimburg, “Mechanical aspects of membrane thermodynamics. Estimation of the mechanical properties of lipid membranes close to the chain melting transition from calorimetry,” *Biochimica et Biophysica Acta - Biomembranes*, vol. 1415, no. 1, pp. 147–162, 1998.

[38] E. A. Evans, “Bending Resistance and Chemically Induced Moments in Membrane Bilayers,” *Biophysical Journal*, vol. 14, no. 12, pp. 923–931, 1974.

[39] T. Heimburg, “Lipid ion channels,” *Biophysical Chemistry*, vol. 150, no. 1-3, pp. 2–22, 2010.

[40] B. Fichtl, I. Silman, and M. F. Schneider, “On the Physical Basis of Biological Signaling by Interface Pulses,” *Langmuir*, pp. 3–8, 2018.

[41] J. Griesbauer, A. Wixforth, and M. F. Schneider, “Wave propagation in lipid monolayers,” *Biophysical Journal*, vol. 97, no. 10, pp. 2710–2716, 2009.

[42] J. Griesbauer, S. Bössinger, A. Wixforth, and M. F. Schneider, “Propagation of 2D pressure pulses in lipid monolayers and its possible implications for biology,” *Physical Review Letters*, vol. 108, no. 19, pp. 1–5, 2012.

[43] P. Overath, L. Thilo, and H. Träuble, “Lipid phase transitions and membrane function,” *Trends in Biochemical Sciences*, no. August, pp. 186–189, 1976.

[44] I. Tasaki, A. Watanabe, R. Sandlin, and L. Carnay, “Changes in fluorescence, turbidity, and birefringence associated with nerve excitation,” *Proceedings of the National Academy of Sciences of the United States of America*, vol. 61, pp. 883–888, 1968.

[45] K. Iwasa and I. Tasaki, “Mechanical Changes in squid giant axons associated with production of action potentials,” *Biochemical and Biophysical Research Communications*, vol. 95, pp. 1328–1331, 1980.

[46] J. M. Tobias, “A chemically specified molecular mechanism underlying excitation in nerve: A hypothesis,” *Nature*, vol. 203, no. 4940, pp. 13–17, 1964.

[47] B. C. Abbott, A. V. Hill, and J. V. Howarth, “The Positive and Negative Heat Production Associated with a Nerve Impulse,” *Proceedings of the Royal Society of London. Series B - Biological Sciences*, vol. 148, pp. 149 LP – 187, feb 1958.

[48] T. Heimburg, “The capacitance and electromechanical coupling of lipid membranes close to transitions: The effect of electrostriction,” *Biophysical Journal*, vol. 103, no. 5, pp. 918–929, 2012.

[49] M. Mussel and M. F. Schneider, "Sound pulses in lipid membranes and their potential function in biology," *Progress in Biophysics and Molecular Biology*, vol. 162, pp. 101–110, 2021.

[50] T. Parasassi, G. De Stasio, G. Ravagnan, R. M. Rusch, and E. Gratton, "Quantitation of lipid phases in phospholipid vesicles by the generalized polarization of Laurdan fluorescence," *Biophysical Journal*, vol. 60, no. 1, pp. 179–189, 1991.

[51] J. R. Lakowicz, *Principles of fluorescence spectroscopy,*. New York: Springer, 3rd ed., 2006.

[52] S. Nigam and S. Rutan, "Principles and Principles and," *Applied Spectroscopy*, vol. 55, no. 11, p. 362A, 2001.

[53] ATTO-TEC Gmbh, "Fluorescent Labels and Dyes: Catalogue," tech. rep., 2018.

[54] Carl Roth, *Voluntary safety information following the Safety Data Sheet format according to Regulation (EC) No. 1907/2006 (REACH); Dimethyl sulfoxide (DMSO)*, 5 2021. Rev. 4.

[55] J.-P. Dufour, N. Ray, L. Buhle, and T. Y. Tsong, "Comparative Study of an Adenosine Triphosphatase Trigger-Fused Lipid Vesicle and Other Vesicle Forms of Dimyristoyl phosphatidyl choline," *Biochemistry*, vol. 20, no. 19, pp. 5576–5586, 1981.

[56] J. Dinic, H. Biverståhl, L. Mäler, and I. Parmryd, "Laurdan and di-4-ANEPPDHQ do not respond to membrane-inserted peptides and are good probes for lipid packing," *Biochimica et Biophysica Acta - Biomembranes*, vol. 1808, no. 1, pp. 298–306, 2011.

[57] S. Fabiunke, C. Fillafer, A. Paeger, and M. F. Schneider, "Optical studies of membrane state during action potential propagation," *Progress in Biophysics and Molecular Biology*, 2020.

[58] Excelitas Technologies, "SPCM-AQRH Single Photon Counting Module," *Datasheet*, 2015.

[59] PicoQuant GmbH, "MicroTime 200," *Brochure*, 2009.

[60] R. N. Lewis and R. N. McElhaney, "Calorimetric and spectroscopic studies of the thermotropic phase behavior of lipid bilayer model membranes composed of a homologous series of linear saturated phosphatidylserines," *Biophysical Journal*, vol. 79, no. 4, pp. 2043–2055, 2000.

[61] J. Li, X. Wang, T. Zhang, C. Wang, Z. Huang, X. Luo, and Y. Deng, "A review on phospholipids and their main applications in drug delivery systems," *Asian Journal of Pharmaceutical Sciences*, vol. 10, no. 2, pp. 81–98, 2015.

[62] S. Shrivastava and M. F. Schneider, "Opto-Mechanical Coupling in Interfaces under Static and Propagative Conditions and Its Biological Implications," *PLoS One*, vol. 8, no. 7, 2013.

[63] P. Grabitz, V. P. Ivanova, and T. Heimburg, "Relaxation kinetics of lipid membranes and its relation to the heat capacity," *Biophysical Journal*, vol. 82, no. 1, pp. 299–309, 2002.

[64] L. Onsager, "Reciprocal relations in irreversible processes. i.," *Phys. Rev.*, vol. 37, pp. 405–426, Feb 1931.

[65] M. Gudmand, M. Fidorra, T. Bjørnholm, and T. Heimburg, "Diffusion and Partitioning of Fluorescent Lipid Probes in Phospholipid Monolayers," *Biophysical Journal*, vol. 96, no. June, pp. 4598–4609, 2009.

[66] R. Macháň and M. Hof, "Recent developments in fluorescence correlation spectroscopy for diffusion measurements in planar lipid membranes," *International Journal of Molecular Sciences*, vol. 11, no. 2, pp. 427–457, 2010.

[67] R. Rigler and J. Widengren, "Fluorescence - based monitoring of electronic state and ion exchange kinetics with FCS and related techniques : from T - jump measurements to fluorescence fluctuations," *European Biophysics Journal*, no. 0123456789, 2017.

[68] J. Widengren, Ü. Mets, and R. Rigler, "Fluorescence correlation spectroscopy of triplet states in solution: A theoretical and experimental study," *Journal of Physical Chemistry*, vol. 99, no. 36, pp. 13368–13379, 1995.

[69] P. Schwille and E. Haustein, "Fluorescence correlation spectroscopy," *An introduction to its concepts and applications*, vol. 94, pp. 1–33, 2001.

[70] C. Eggeling, C. Ringemann, R. Medda, G. Schwarzmann, K. Sandhoff, S. Polyakova, V. N. Belov, B. Hein, C. Von Middendorff, A. Schönle, and S. W. Hell, "Direct observation of the nanoscale dynamics of membrane lipids in a living cell," *Nature*, vol. 457, no. 7233, pp. 1159–1162, 2009.

[71] P. Kapusta, "Absolute Diffusion Coefficients: Compilation of Reference Data for FCS Calibration," *Application Note*, 2010.

[72] J. R. Silvius *et al.*, "Thermotropic phase transitions of pure lipids in model membranes and their modifications by membrane proteins," *Lipid-protein interactions*, vol. 2, pp. 239–281, 1982.

[73] J. Korlach, P. Schwille, W. W. Webb, and G. W. Feigenson, "Characterization of lipid bilayer phases by confocal microscopy and fluorescence correlation spectroscopy," *Proceedings of the National Academy of Sciences of the United States of America*, vol. 96, no. 15, pp. 8461–8466, 1999.

[74] R. N. Lewis, N. M. Nanette Mak, and R. N. McElhaney, "A Differential Scanning Calorimetric Study of the Thermotropic Phase Behavior of Model Membranes Composed of Phosphatidylcholines Containing Linear Saturated Fatty Acyl Chains," *Biochemistry*, vol. 26, no. 19, pp. 6118–6126, 1987.

[75] P. Parkkila, M. Štefl, A. Olzyńska, M. Hof, and P. K. Kinnunen, "Phospholipid lateral diffusion in phosphatidylcholine-sphingomyelin-cholesterol monolayers; Effects of oxidatively truncated phosphatidylcholines," *Biochimica et Biophysica Acta - Biomembranes*, vol. 1848, no. 1, pp. 167–173, 2015.

[76] B. S. Lee, S. A. Mabry, A. Jonas, and J. Jonas, "High-pressure proton NMR study of lateral self-diffusion of phosphatidylcholines in sonicated unilamellar vesicles," *Chemistry and Physics of Lipids*, vol. 78, no. 2, pp. 103–117, 1995.

[77] R. Machán and M. Hof, "Lipid diffusion in planar membranes investigated by fluorescence correlation spectroscopy," *Biochimica et Biophysica Acta*, vol. 1798, pp. 1377–1391, 2010.

[78] H. A. Faizi, R. Dimova, and P. M. Vlahovska, "A vesicle microrheometer for high-throughput viscosity measurements of lipid and polymer membranes," *Biophysical Journal*, vol. 121, no. 6, pp. 910–918, 2022.

[79] J. Kragel, J. Li, R. Miller, M. Bree, G. Kretzschmar, and H. Mohwald, "Surface viscoelasticity of phospholipid monolayers at the air/water interface," *Colloid and Polymer Science*, vol. 274, pp. 1183–1187, 1996.

[80] J. Heberle, J. Riesle, G. Thiedemann, D. Oesterhelt, and N. A. Dencher, "Proton migration along the membrane surface and retarded surface to bulk transfer," *Nature*, vol. 370, no. 6488, pp. 379–382, 1994.

[81] M. Gutman and E. Nachliel, "The dynamics of proton exchange between bulk and surface groups," *BBA - Bioenergetics*, vol. 1231, no. 2, pp. 123–138, 1995.

[82] P. Brzezinski and J. Widengren, "Localized proton microcircuits at the biological membrane – water interface," *Proceedings of the National Academy of Sciences*, vol. 103, 2006.

[83] T. Sandén, L. Salomonsson, P. Brzezinski, and J. Widengren, “Surface-coupled proton exchange of a membrane-bound proton acceptor,” *Proceedings of the National Academy of Sciences*, vol. 107, no. 9, 2010.

[84] T. F. Scientific, “The molecular probes® handbook, a guide to fluorescent probes and labeling technologies, Thermo Fisher Scientific,” 2020.

[85] J. Bergstrand, P. Brzezinski, and J. Widengren, “Protonation Dynamics on Lipid Nanodiscs : Influence of the Membrane Surface Area and External Buffers,” *Biophysical Journal*, pp. 1993–2003, 2016.

[86] A. Lichius and S. Zeilinger, “Application of membrane and cell wall selective fluorescent dyes for live-cell imaging of filamentous fungi,” *Journal of Visualized Experiments*, vol. 2019, no. 153, pp. 1–16, 2019.

[87] R. Pagano and C. Chen, “Use of BODIPY-labeld sphingolipids to study membrane traffic along the endocytic pathway,” *Annals Reports*, vol. 845, no. 1, pp. 152–160, 1998.

[88] S. Kumari, S. Mg, and S. Mayor, “Endocytosis unplugged: Multiple ways to enter the cell,” *Cell Research*, vol. 20, no. 3, pp. 256–275, 2010.

[89] C. S. Fedosejevs and M. F. Schneider, “Sharp, localized phase transitions in single neuronal cells,” *Proceedings of the National Academy of Sciences*, vol. 119, no. 8, p. e2117521119, 2022.

[90] M. Wagner, P. Weber, T. Bruns, W. S. Strauss, R. Wittig, and H. Schneckenburger, “Light dose is a limiting factor to maintain cell viability in fluorescence microscopy and single molecule detection,” *International Journal of Molecular Sciences*, vol. 11, no. 3, pp. 956–966, 2010.

[91] H. Schneckenburger, P. Weber, M. Wagner, S. Schickinger, V. Richter, T. Bruns, W. S. Strauss, and R. Wittig, “Light exposure and cell viability in fluorescence microscopy,” *Journal of Microscopy*, vol. 245, no. 3, pp. 311–318, 2012.

[92] K. Bacia and P. Schwille, “A dynamic view of cellular processes by in vivo fluorescence auto- and cross-correlation spectroscopy,” *Methods*, vol. 29, no. 1, pp. 74–85, 2003.

[93] F. Tablin, A. E. Oliver, N. J. Walker, L. M. Crowe, and J. H. Crowe, “Membrane phase transition of intact human platelets: Correlation with cold-induced activation,” *Journal of Cellular Physiology*, vol. 168, no. 2, pp. 305–313, 1996.

[94] E. Sezgin and P. Schwille, “Fluorescence Techniques to Study Lipid Dynamics,” *Cold Spring Harbor perspectives in biology*, pp. 1–32, 2011.

[95] C. K. Biebricher and M. Eigen, "What is a quasispecies?," *Current Topics in Microbiology and Immunology*, vol. 299, pp. 1–31, 2006.

[96] E. J. Walter and M. Carraretto, "The neurological and cognitive consequences of hyperthermia," *Critical Care*, vol. 20, no. 1, pp. 1–8, 2016.

[97] E. J. Walter, S. Hanna-Jumma, M. Carraretto, and L. Forni, "The pathophysiological basis and consequences of fever," *Critical Care*, vol. 20, no. 1, pp. 1–10, 2016.

[98] P. L. Privalov, "Cold denaturation of protein," *Critical Reviews in Biochemistry and Molecular Biology*, vol. 25, no. 4, pp. 281–306, 1990.

[99] C. Eggeling, C. Ringemann, R. Medda, G. Schwarzmann, K. Sandhoff, S. Polyakova, V. N. Belov, B. Hein, C. Von Middendorff, A. Schönle, and S. W. Hell, "Direct observation of the nanoscale dynamics of membrane lipids in a living cell," *Nature*, vol. 457, no. 7233, pp. 1159–1162, 2009.

[100] I. H. Lee, S. Saha, A. Polley, H. Huang, S. Mayor, M. Rao, and J. T. Groves, "Live cell plasma membranes do not exhibit a miscibility phase transition over a wide range of temperatures," *Journal of Physical Chemistry B*, vol. 119, no. 12, pp. 4450–4459, 2015.

[101] L. D. Frye and M. Edidin, "The rapid intermixing of cell surface antigens after formation of mouse-human heterokaryons.," *Journal of Cell Science*, vol. 7, no. 2, pp. 319–335, 1970.

[102] C. Fillafer, A. Paeger, and M. F. Schneider, "The living state: How cellular excitability is controlled by the thermodynamic state of the membrane," *Progress in Biophysics and Molecular Biology*, pp. 1–27, 2020.

[103] L. Windgaße, "Optical characterization of the thermodynamic state of cell layers, Masterthesis," 2016.

[104] "Fcs2 chamber system." `https://bioptechs.com/fcs-chamber-system/`. Accessed: 2022/08/08.

Acknowledgment

The completion of this thesis would have not been possible without the support of several people I want to thank at this point.

First of all, I thank my supervisor Prof. Dr. Matthias F. Schneider for giving me the opportunity to conduct my PhD in his lab and for making two research stays possible at the KTH in Stockholm during that time. Thank you, for introducing me into a new way of approaching living systems and sharing your inspiring enthusiasm for this field. I had a lot of freedom to explore the possibilities in the lab which I really appreciate. I want to thank Dr. Matan Mussel as well for taking the time to be the second advisor of this thesis and for fruitful discussions during his time in our group.

I thank Prof. Dr. Widengren for giving me the opportunity to visit his lab at the KTH Stockholm for several weeks during my PhD. I could draw so much helpful from this time and the stays were crucial for my progress in the experimental work on the fluorescence correlation spectrometer.

Further, I want to mention Dr. Konrad Kaufmann. Thank you for inspiring talks and your constant efforts to bring us students closer to your theories.

I want to thank **all** my colleagues for providing a fruitful atmosphere at work: In particular, Dr. Christian Fillafer, who is always supportive and takes time for discussing problems. Lisa, for being the good soul of the group and supporting all of us constantly. Daniel, for being helpful whenever problems occur and for working well together on our shared teaching duties.

I want to address a very special *thank you* to my office colleagues: Anne, Gregor and Simon. We had great years together sharing an office (unfortunately interrupted by Covid). You made that time always fun even on the tough days. I will miss the discussions, the mutual support, the jokes and of course our table tennis matches. I feel privileged to spend the last years working with you.

Completing this thesis made it often impossible to let work be work. I want to thank my flat mates for being supportive and understanding in all this time. Also, I would like to thank my very good friend Theresa: Thanks for listening to my problems even though you have had sleepless nights caused by little Romy. :)

I am extremely thankful for the unconditional support of my parents, without which I would definitely not have come this far.

At last, I want to thank my boyfriend, Simon. Without his moral support I would have been lost several times. His care for me is amazing and I am incredibly happy to experience his unreserved support and love during all times.